UNIVERSITÀ DEGLI STUDI DI PALERMO

Dottorato in Energia – Indirizzo Energetica
D.E.I.M. - Dipartimento di Energia, Ingegneria dell'Informazione e Modelli Matematici
Settore Scientifico Disciplinare ING-IND/11

BUILDING INTEGRATED SOLAR THERMAL DESIGN: CHARACTERISATION AND ASSESSMENT OF PERFORMANCES OF A LOW COST SOLAR WALL.

IL DOTTORE
Arch. GIULIANA LEONE

IL COORDINATORE
prof. ing. ALDO ORIOLI

IL TUTOR
Prof. ing. MARCO BECCALI

CICLO XXV
ANNO CONSEGUIMENTO TITOLO 2015

TABLE OF CONTENTS

INTRODUCTION

Present work deals with the topic of renewable energy focusing of solar thermal collector and building integration issues especially focusing on the topic of a low cost building energy refurbishment strategy.

Nowadays, the prospects of worldwide climatic changes have promoted increasing attention on energy-saving measures and many efforts have been done to enable such an issues, both at research and legislative level. Indeed, energy use in buildings represents a relevant percentage of the total primary energy demand in the EU and therefore developing effective energy alternatives is imperative: from one hand, the existing building stock is generally inappropriate at energy performance level and from the other hand, new construction are getting more and more unusual. From all these considerations come the needs to investigate retrofit strategy and to make them attractive from an economical point of view.

Since forward, the prospects of a traditional energy system crash have prompted investigations to exploit alternative energy sources exploitation at building level as well as to reduce the required energy by buildings themselves. Recently these two issues have converged in a unique line of research aimed to determine the best compromise between energy demand and supply. Building integration is then an important goal since it could improve the spread of such a renewable technologies by making themselves more accepted by people and since integration optimises the exploitation of available space making easier resolving related property issues.

The main question is: ***what does an integrated component mean?*** The most reasonable response is today: ***a plant component that apart of its primary function as a heating/power generator, plays a specific role as a building component***. It could be a shelter or a finishes of the building envelope itself.

Actually, researches seem to be focused on finding a way for obtaining this double function at a technological level but if the easier way to do that is considered, what does it happen at thermal behaviour level and at energy production level for the solar component whenever itself is integrated in a wall? And what happen at energy building overall performance and at energy exchange through the wall if the solar thermal collector is itself integrated in the wall? Moreover, it is possible to reach satisfactory resuts with esy and low-cost installations?

THIS ARE ESSENTIALLY THE MAIN QUESTION ADDRESSED BY PRESENT WORK WHOSE FLOW CHART IS PRESENTED BELOW.

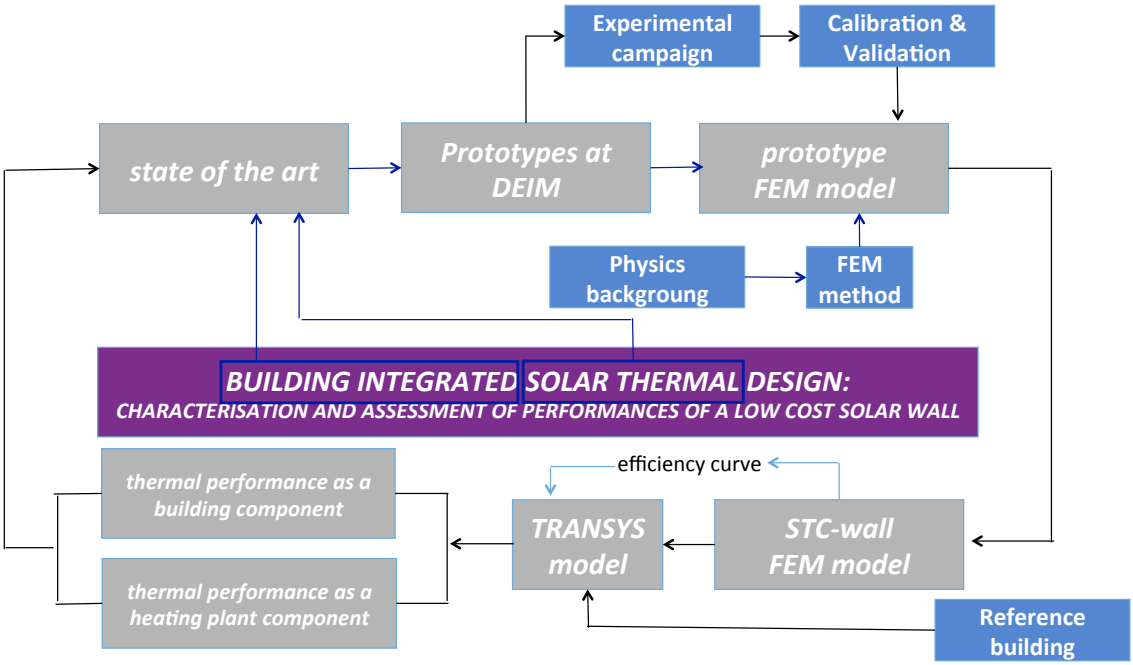

Fig. 1 Thesis flowchart

Start-up of research was an overview of the present state of the art in the field of integrated solar thermal technologies from one hand and of the new NZEB theories from the other hand, whose results are reported in **CHAPTER 1**. For answering previous question, two low cost prototypes tested at the Università degli Studi di Palermo – DEIM are available and will be presented in **CHAPTER 2**.

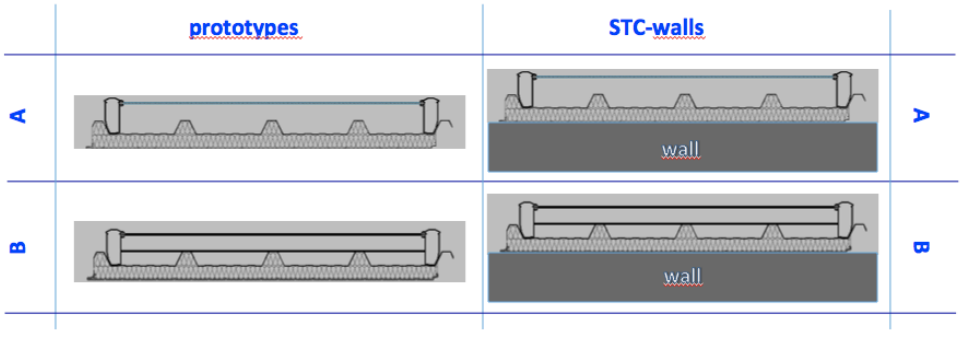

Fig. 2 Investigated models and their nomenclature. On the left the prototype configurations, on the right the correpsonding integrated configurations (addressed as STC-wall).

They are really feasible for the present purpose since they could be easily integrated in the building envelope and since their cost is really low using component that are common in the

market at a really slow price. Technological assumptions at constructional level and a first overview on the integrated component thermodynamic system are presented in the same chapter. Meanwhile the basic knowledge needful for building up the FEM model as well as for understanding the meaning of the results are summarised in **CHAPTER 3**.

Data from the experimental campaign on prototypes were then used for validating and calibrating a FEM models whose main characteristics at physics and calculation levels and whose reliability are presented in **CHAPTER 4** and constitute the basis for implementing two wall-integrated solar collectors, **CHAPTER 5**. These models were indeed used for sorting the efficiency curves that were suitable for evaluating solar collector energy production in working condition over a typical year in a specified site.

Finally, in **CHAPTER 6** a reference building is then choose and 8 solar collector arrays are supposed to be integrated in the south façade according to its main architectonical features. Collectors and building are then simulated in Trnsys evaluating from one hand the useful energy from the active component and the gain through the focused wall considering heat exchange happens between the indoors conditions boundary and the surface temperature at wall/collector interface. Main results from the thesis are then outlined in **CHAPTER 7.**

1. INVESTIGATED TOPICS

The present chapter deals with a critical analysis of the most important researches that have been carried out during the past decades. Two main lines will be followed according to the topic of the present work being aware that an overall approach is needed: from one hand the recently NZEB theories have been analysed; from the other hand the solar collector integration studies are addressed.

1.1 Outlines from IEA SHC/ECBCS- task 40: toward Net Zero Energy Solar Building

Theory and definition

A Net Zero Energy Building is commonly defined as "*a building with greatly reduced energy needs through efficiency gain such that the balance of energy needs can be supplied by renewable technologies*" [39]. So it is clear that researches in the topic move toward an integrated approach to the problem being conscious that it's not enough providing only "green" energy to the building and it's not enough reducing only its energy demand: the two instances have to meet in some point. The main idea is then exploiting as much as possible low-cost, locally available, non-polluting renewable sources for producing on site enough energy (or more) than the one needed by the building.

Despite of this shared definition and intents a clear meaning of the "Net Zero" concept is still missing: which are the energy carriers to be considered, and consequently which is the metric of the problem? Moreover, which is the boundary of the system and consequently which energy carriers go in it and which ones come out? Answering these questions is a focus point for having a clear definition and definitively will influence design strategy and local energy policy regulations. As outlined by Torcellini *et al*. [39] different specific definitions could be introduced with respect to the values of the different actors involved in the project (building designer, national energy agency, etc.) are interested in:

1. NET ZERO **SITE** ENERGY: a site ZEB produces at least as much energy as it uses in a year, when accounted for at the site.

2. NET ZERO **SOURCE** ENERGY: A source ZEB produces at least as much energy as it uses in a year, when accounted for at the source. Source energy refers to primary energy used to generate and deliver the energy to the site by multiplying to an appropriate site-to-source conversion factor.

3. NET ZERO ENERGY **COST**: In a cost ZEB, the amount of money the utility pays the building owner for the exported energy from the building to the grid is at least equal to the amount of money the owner pays the utility for the energy services and the energy used over the year

4. NET ZERO ENERGY **EMISSION**: A net-zero emission building produces at least as much emission-free renewable energy as it uses from emission-producing energy sources

Marzsal et al. [36] focused then on the facts that some questions have to be clearly answered and a methodology for calculation well defined before goes on with a proper definition. Actually, if some points are not clearly defined, different concepts and definitions could come and different design strategies are encouraged. We talk about: metric, period and type of the balance as well as the type of energy use, the way connections with the infrastructure are and the way the renewable energy supply option fulfil.

For the purpose of the present study, whatever concerning the energy production/use/exportation is of particular interested. For example, if the **site ZEB** definition is applied then aggressive energy efficiency design is needed since the one-unit energy value from different sources when accounted for them at the site is not differentiated. Consequently, on-site generated electricity has to offset gas use (as merely example) on a 1 to 1 basis. From the other hand, if the **source ZEB** definition is introduced appropriate site-to-source energy factor will be needed probably influencing the national energy plans. Moreover, if **cost ZEB** definition is considered every kind of decision on renewable energy supply will be affected by external influence related to the market of energy at global and local level. Finally, if the **zero-emission** definition is chosen once again the energy supply strategy will be affected by externalities related to the way energy is produced at the source. If emissions-free renewable energy is nearby available (for example nuclear, hydro electricity, ect…), no interest in providing emission-free energy generation on-site will arise.

From that point of view, Marzsal and Heiselberg [35] citing Lausten (2008), similarly as Mertz, et al. (2007), mention two approaches:

· **Zero Net Energy Buildings** *are buildings that over a year are neutral, meaning that they deliver as much energy to the supply grids as they use from the grids. Seen in these terms they do not need any fossil fuel for heating, cooling, lighting or other energy uses although they sometimes draw energy from the grid.*

· **Zero Carbon Buildings** *are buildings that over a year do not use energy that entails carbon dioxide emission. Over the year, these buildings are carbon neutral or positive in the term that they produce enough CO_2 free energy to supply themselves with energy. Zero Carbon Buildings differ from Zero Energy Building in the way that they can use for instance electricity produced by CO_2 free sources, such as large windmills, nuclear power and PV solar systems which are not integrated in the buildings or at the construction site.*

According to the utilised definition, the understanding of the most suitable combination of applicable efficiency measures at building level and renewable energy supply options at plant level is then imperative for achieving the net-zero target. At the same time, it is also necessary to identify the boundaries of the system on which depend the definition of in-coming/out-coming energy fluxes. From that point of view, scientific community agrees in introducing a differentiation in energy supply options that are of interest for the topic of present work, see tab. 1 [39].

tab. 1 ZEB renawable energy supply option

hierarchy	reduce energy demand by means of:	example	
0.	-using low-energy building technology	daylighting, high-efficiency HVAC equipment, natural ventilation, evaporative cooling…	
1.	- using renewable sources installed in the building's footprint	Integrated PV-system, integrated ST-system, small-scale wind power generation, …	on-site
2.	- using renewable sources available on site but not in the building's foot print	PV- installation, ST-installation, low-impact hydro, located on-site	
3.	- using renewable sources available off-site for generating energy on-site	biomass, biodiesel, wood pellets imported for generating heat/electricity on-site	off-site
4.	- purchase off-site renewable energy sources	utility-based wind, PV, emission credits and other green purchasing options	

From tab. 1 it is evident how first option is to reduce the energy demand as much as possible by passive solution and then exploiting the renewable sources to fulfil the residual demand by installation as closed as possible to the building itself; purchasing energy from off-site is the last option. Consequently the building integration of plant component, as solar collectors are, plays a key role in NZEB theory.

Summarising, *Fig. 3* from [40] graphically describes the typical balance in which line at 45° represents the NZEB target, meanwhile points lying above this line refers to Plus Energy Building that produces more energy than it consumes and points lying nearby the 45° line but under it represents the Nearly Zero Energy Building target. Nonetheless it is evident how different results follow if energy load/generation criteria are applied instead of delivered/export criteria. At the same time, results will be affected by the chosen weighting factors whose values have to be properly defined. Actually these factors belong to technical features moreover they could be also influenced by political decisions influencing in turn the energy policy at national level.

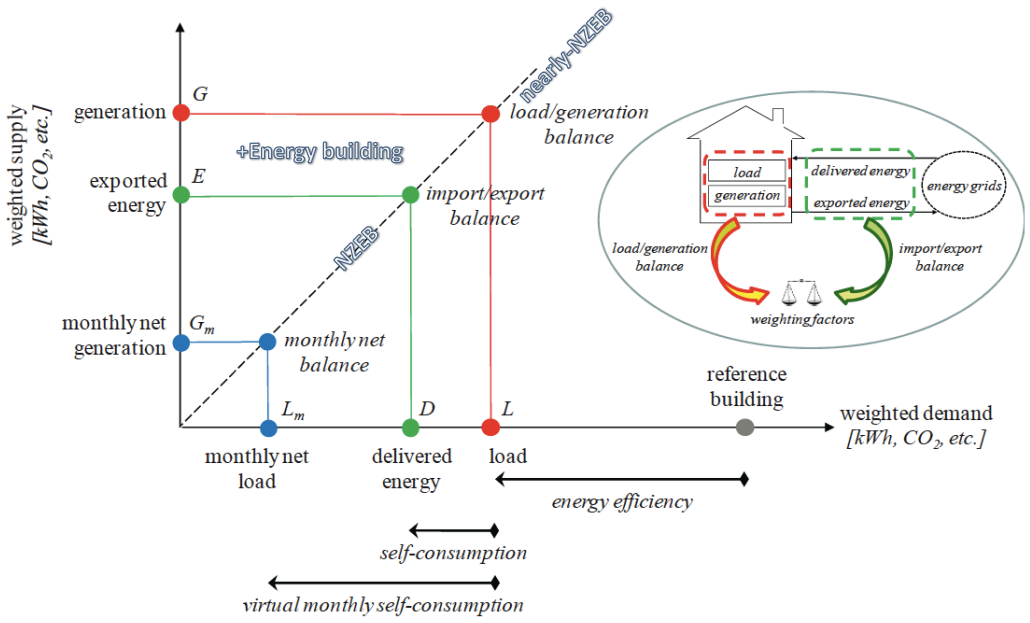

Fig. 3 Graphical representation of the three types of balance: import/export balance between weighted exported and delivered energy, load/ generation balance between weighted generation and load, and monthly net balance between weighted monthly net values of generation and load, source.

All things considered, all researches in NZEB will hopefully deal with national regulations as outlined by Marzsal et al. [34] who presented an overview of Net ZEBs energy calculation methodologies proposed by organisations representing eight different countries. At European level the EPBD recast has already introduced the NZEB model and new public building have to achieve the nearly zero target. Anyway, NZEB concept is not yet included in the most of the national building codes even if some common points are shared among the different regulations. For example in many countries the most favoured practise is to account on the yearly building balance between energy use and renewable energy generation. Nonetheless, Marzsal et al. [34] have substantially outlined how some discrepancies exist among the different energy code approaches to Net ZEBs.

Finally, a focal point according to NZEB theory and to the purpose of present study is the grid-interaction; from that point of view the latter is not only allowed but also strictly necessary, to fulfil the gap between load/demand matching that generally occurs when renewable source are used. Studies have been carried out by many authors regarding this topic, for example Voss et. al [41] analysing some monitored building proposed some indexes for evaluating the load matching and the grid interaction for renewable source exploitation. Also Salom et al. [37] addressed such a topic distinguishing residential building and offices in different climatic conditions in order to sort appropriate load match (LM) and grid interaction (GI) indicators.

NZEB constructions

Despite of all national building code discrepancies and theoretical open-questions, the zero target have been anyway applied in new constructions as well as in building refurbishment and some database are already available; particularly Garde and Donne [32] gave an overview of 30 Net ZEBs case studies. The German Federal Ministry of Economics and Technology sponsored a research (EnOB: Research for energy-optimised construction) involving all new buildings or refurbished ones within the German territory that have gain minimal primary energy requirements and high occupant comfort, with moderate investment costs and significantly reduced operating costs. Moreover the EnOB gives a generic worldwide overview on Net zero-energy buildings [http://www.enob.info/en/net-zero-energy-buildings/map/], see *Fig. 4*.

Fig. 4 Worldwide EnBO database

According to the purpose of present study, it is of interested outlining all building where the solar thermal technology has been applied. Specifically, the two databases consist respectively of 30 and 57 case studies moreover while the Garde and Donne database addresses building all around Europe in different climatic conditions, the German database focus only on construction built within its national territory distinguishing 33 new building and 27 refurbishing cases. The first group includes all constructions built from 1990 until today with a range of new concepts, materials and technologies suitable for getting energy-optimised constructions. They are scientifically evaluated over an extended occupation period, and optimised during completely normal operation. The second group includes building built during the 50-70th and recently refurbished employing innovative technologies in order to achieve energy efficiency high level. Actually, the German database does not directly deals with the NZEB concept anyway it is of interest for the present study.

For making populations from the different database comparable each other, only constructions in heating dominated climate from Garde and Donne have been considered sorting 26 case studies. Specifically, Solar thermal and PV use has been compared, actually these two technologies could be regarded each other as design options, according to the available roof/façade/ground available surfaces.

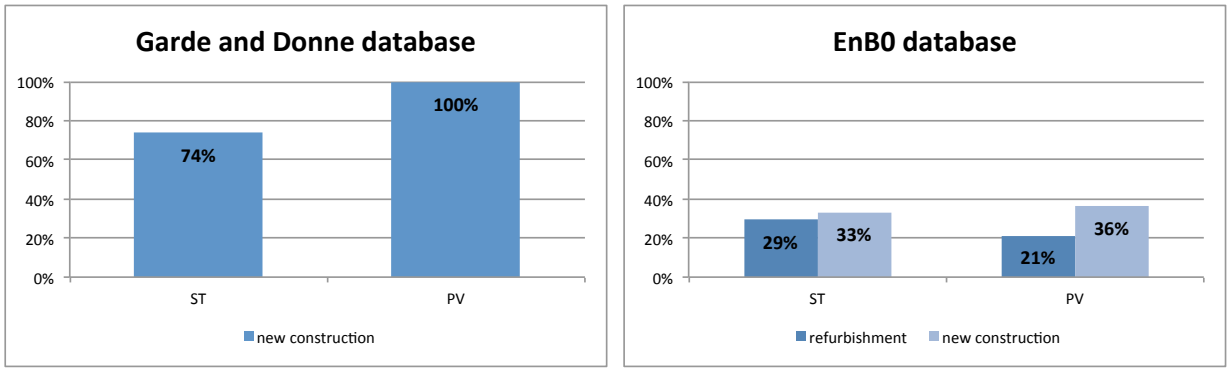

Fig. 5 Use of solar thermal technology in new construction and reburbishement

Fig. 5 shows how the solar renewable option is more exploited when NZEB target is directly addressed with slightly higher interested in PV-systems. Actually all buildings from Garde and Donne include a PV-plant meanwhile heating source is sometimes biomass or in the case of Pixel building in Australia and Plus Energy Houses Weiz in Germany heat pump driven respectively by combined wind turbine/PV plant and roof integrated PV-plant.It is worth to notice that flat plate collectors are commonly used in new construction and building integration in façade preferred wherever possible, see *Fig. 6*.

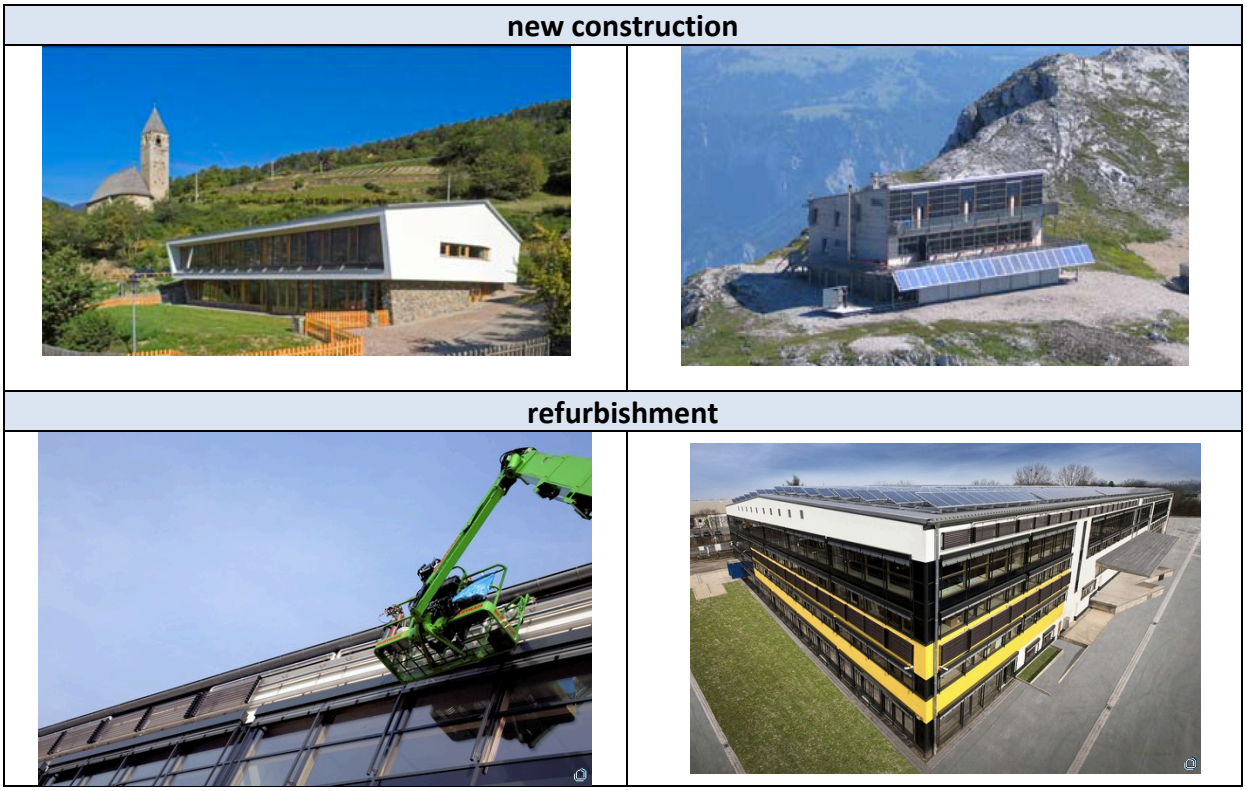

Fig. 6 On the top Primary School of Laion (left) and Alpine Refuge – Schiestlhaus (right) from Garde database, on the bottom Derelict factory building transformed into energy-plus building from EnBO database.

1.2 Outlines from IEA SHC – TASK 41: Solar energy and architecture – Innovative components toward building integration

Building integration design

From previous analysis it follows that solar thermal technology is of particular interest especially for new NZEB construction. Nonetheless, energy retrofit in refurbishment is an important goal since the existing building stock significantly affects world energy consumption and solar technologies could actually contribute to reduce building energy demand. In this sense, building integration issues is of current importance since generally the available space for ST (or PV) plant has to be searched in the building envelope itself. Moreover, different from its PV counterpart, solar thermal plant needs to be close to the place where the produced energy is consumed.

Solar collector should be hence conceived as multifunctional envelope systems in which functional aspects, constructive issues and formal (aesthetic) targets have to meet in a unique component **[51**]. It means architectural and engineering instances have been regarded as a unique topic.

Munari-Probst and Roecker **[53**] outlined this problem giving an overview of ST building-integration appreciation among a large pool of European architects, engineers and façade manufacturers, equally representing the different European climatic area. A survey was them proposed via the web and results shown by ***Fig. 7***. As supposed, judgments by the two different professional categories are not always comparable. Integration guidelines follow from the survey and could be summarized in five interdependent points affecting building integration quality:

1. Size and position of collector field.
2. Shape and size of the modules.
3. Type of jointing.
4. Collector material and surface texture.
5. Absorber colour.

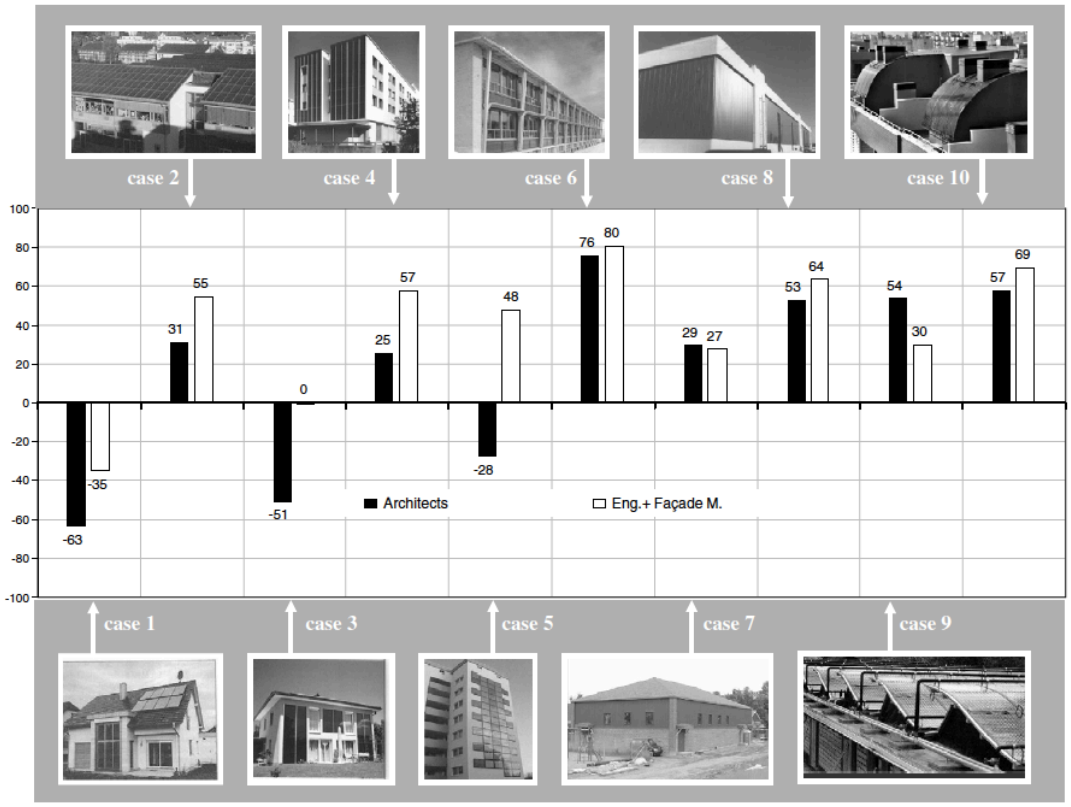

Fig. 7 Survey results from Munari-Probst and Roecker survey. Architects and engineers appreciation results (results reported on a -100 to +100 scale)

Actually, if the building envelope is schematically considered it is possible to distinguish opaque and transparent (or translucent) parts from one hand and overhang elements from the other hand, ***Fig. 8***. Opaque and transparent elements have both a protection functions from weathering and from intrusions but also accomplishing the task of modulate heat transfer between indoor and outdoor by means of multi-layer structure. Moreover transparent elements modulate additionally solar gain while ensuring day lighting and visual contact with the outdoor. At the same time solar collector technical requirements have to be considered and ensured meanwhile aesthetical targets have to be fulfil for improving the acceptance of the technology by architects/owners/manufacturers.

opaque envelope			transparent element	shading device	balconies and similars
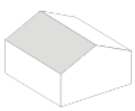	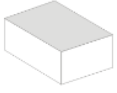	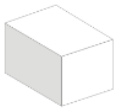	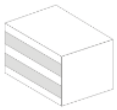	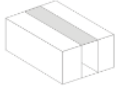	

Fig. 8 Building integration function

At this regards, Munary-Probst and Roecker **[51**] identified three different level of integration:

1. **Basic level:** solar system are easily customisable in size and shape offering appropriate selection of jointing and reasonable colours in order to ensure formal flexibility and adaptively to specific contexts and buildings.

2. **Medium level:** standardised non-active elements similar to solar model are provided for architectural envelope coherence**.**

3. **Advanced level:** complete roof/façade system with active and non-active elements, interface elements (jointing, finishing, angular component) is designed from an overall point of view. For developing such integral solar envelope system, two possible approaches could be considered: starting from the collector technology or starting from the envelope system.

The IEA SHC Task 41 database [http://task41.iea-shc.org/casestudies/] consisting of 17 case studies built up all around Europe could be taken as start point for analysing what has been done since today. From an overview of all building in the database, the most common integrated solar thermal technology is the flat plate collector that is generally integrated in façade and usually used for both heating and DHW production purposes.

Three approaches to integration design have been noticed: using standard collector component, using size-customised collector component and adapting building component for obtaining an air-heating element. Among the first group of buildings Kraftwerk B and Sunny woods are taken as example while Home+ and FESTI belong respectively to the second and third group.

Specifically, the first is a multi-family house (***Fig. 9***) whose aim was to reduce as much as possible energy demand while realising an environmentally sustainable building. Actually, this building produces more energy than it needs thanks to the roof integrated PV system and façade integrated solar thermal plant. Standard components have been used and as a

result a typical window partition is introduced alternating glazed surface and flat plate solar collectors.

From the other hand, Sunny woods is a south-oriented four storey apartment building that was built in a residential area of Zurich in 2000/2001. It integrates both photovoltaic system that covers all roof surface and solar thermal modules. Specifically standard vacuum collectors are used as balcony railing at the south façade.

NEW BUILDING - **KRAFTWERK B** - Switzerland

Fig. 9

NEW BUILDING - **SUNNY WOODS** - Switzerland

Fig. 10

Using standardised components as in the previous case studies generally allow reducing cost while affecting the façade aesthetics since panel size will influence the partition and the dimension of building features. Higher level of integration at aesthetical level (but also higher cost) could be achieved if customised products are used adapting their size to the architectonical characters. It is the HOME+ designed and built for the Solar Decathlon European competition in 2011, the proposed plus energy building is completely wrapped in PV, ST and PVT collectors, ***Fig.* 11**. The double function of the ST vacuum tubes influences the spatial experience creating shadows inside the building that move during the course of the day. The PV system, which is integrated into the facade, was specially developed for this building. In this case PV, ST and PVT modules are actually the real architectonical component also at aesthetical level.

NEW BUILDING - **HOMEplus** – GERMANY team for Solar decathlon

Fig. 11

Another option is to use available standard component in the market such as corrugated panels for implement a solar component. It is the case of the head-office for Fire and Emergency Services Training Institute (FESTI) in Canada (***Fig.* 12**). Focal point of the project is the SolarWall that serves at the same time as a cladding and as a heating system. The façade consists then of two different metal panelling systems: the perforated black siding of the SolarWall is creating contrast with white non-perforated metal panels on the remaining exterior façade.

Specifically the corrugated black sheet captures solar energy and transfer heat to the air trapped between this outer layer and the massive wall on the back. Moreover the high mass wall stores heat during the day decreasing the energy demand for heating even after the sun has passed the solar thermal facade. Convective forces feed the air into a plenum only when heating is required in the building.

NEW BUILDING – **FESTI** - CANADA

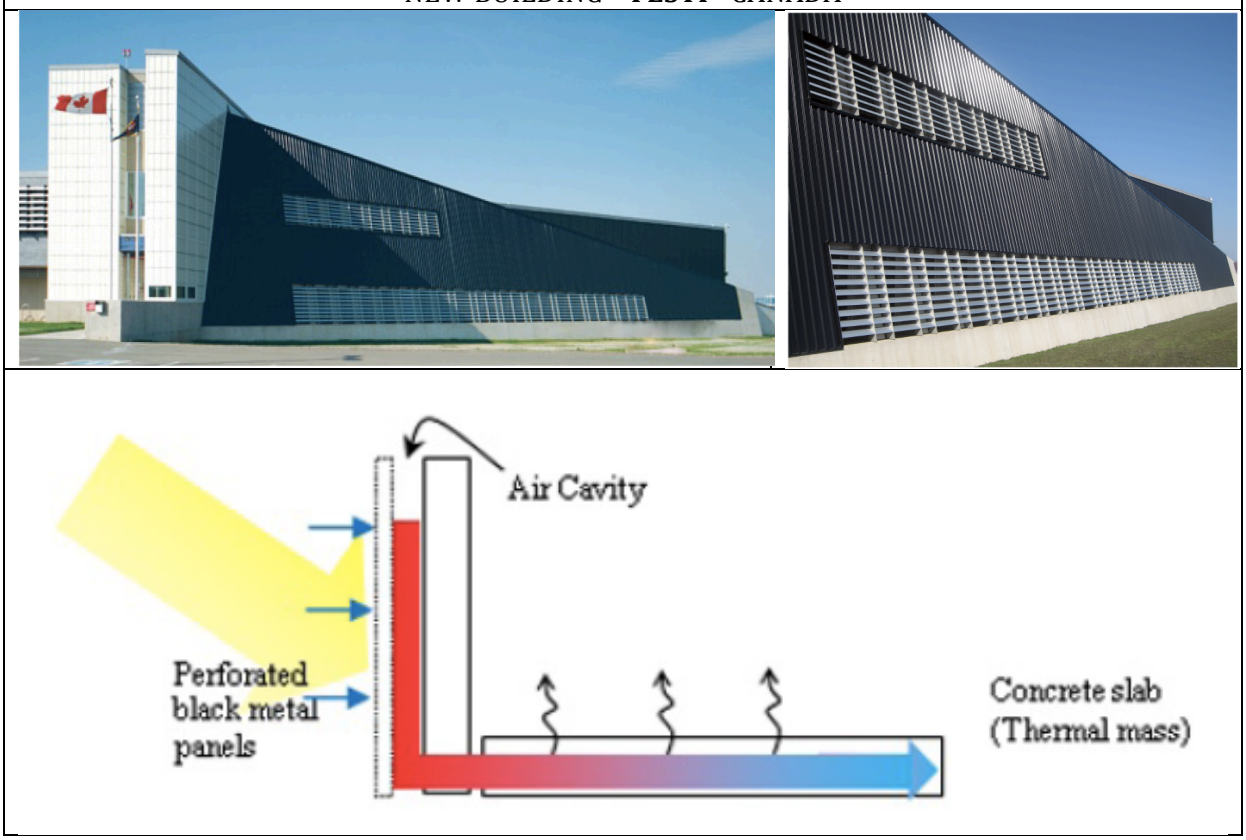

Fig. 12

Higher level of complexity is represent by the **XELIOX ENERGY LAB** in Italy, ***Fig.* 13**. It is a refurbishment design of an existing building in which for compensating the not optimal exposure a double façade is properly designed in order to integrate standard panels. The modules are alternated between solar thermal, photovoltaic and transparent glass panels allowing natural light passing into the public entrance space. The Italian typical precast concrete structure and the typical aluminum frame are then used in an innovative design for including solar panels in a continue skin. Moreover a number of parabolic collectors are installed on the roof and will be used for solar cooling in summer and solar heating in winter.

Actually the main idea of the design is to exploit as much as possible solar energy for heating, cooling and electrical production obtaining at the same time a proper illumination level and overpassing one of the typical problem in solar energy retrofit strategy concerning the actual building orientation.

REFURBISHMENT - **XELIOX ENERGY LAB** - ITALY

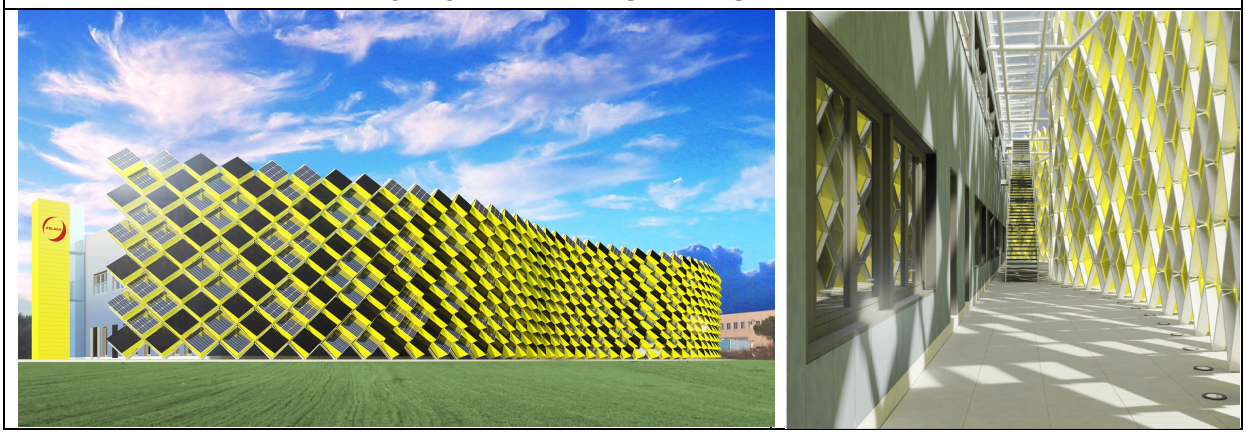

Fig. 13

Available collector and integration issues

Other interesting studies concern the best available technologies. At this regards, a first review of the available products in the market and of their suitability to be integrated in the building is proposed. From this point of view, Munari Probst and Roecker **[52**] gives a complete overview of the problem while distinguish the most common technology (glazed flat plate collector, unglazed collector and evacuated tubes). Four general criteria are followed in order to outline pros and cons for each analysed collector technology:

1. **multi-functionality**: the suitability of the solar collector to accomplish to specific functions as a technological component of the building (façade/roof coating, balcony railings,…);
2. **joint**: the feasibility of the solar component to be constructively integrated in the building considering water tightness and aesthetic issues;
3. **dimension**: the achievability of obtaining customisable component with regards to their length, width and thickness;

4. **colour**: the availability of different colour finishes for achieving aesthetic integration;
5. **visible surface texture and finishes**: the possibility and availability of different finishes characterising the aesthetic of the component.

Actually, from these points of view, it is possible to organise dissertation distinguishing the glazed and unglazed collectors from the evacuated tube technology.

Indeed, both glazed and unglazed collector have common features and could be easily integrated as building component (roof/façade cladding) with an additional possibility for the unglazed collector to obtained curved shape meanwhile the glazed collector are sometimes used also as shading devise or balcony railings. Generally, this kinds of collectors are integrated in the opaque envelope, nonetheless new semi-transparent glazed collector has recently paved the way to integration into the transparent component even if they could serve mainly as glare control systems, ***Fig. 14***. At the same time it is interesting to notice how, due to their structure, the flat plate collector layers could be easily merged into the envelope layers when integrated in façade and roof. Anyway in glazed and unglazed collector cases, vapour transfer through the envelope component has to be carefully assessed meanwhile resistance to shock and weathering is of particular interest for unglazed collector. From that point of view, one safe way to ensure the building function is to inspire the unglazed system from existing envelope systems like metal roofing or claddings.

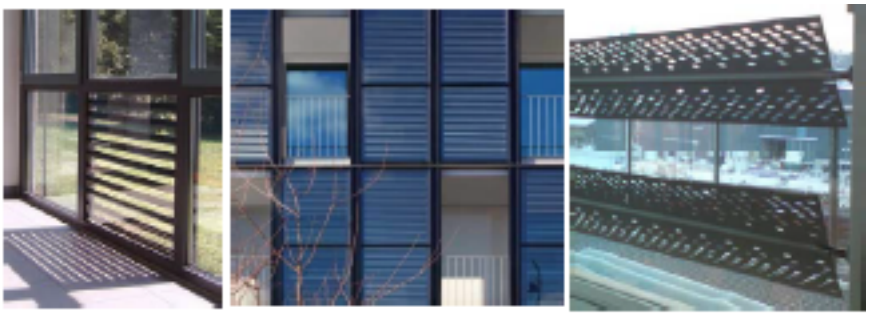

Fig. 14Trasparency in glased flat plate collector

Concerning joints, the trickiest problem at technical level for both technologies is related to roof integration and water tightness. At the same time jointing imply also an aesthetic evaluation overall for glazed collector in which two different types of joint could be distinguished and are more evident: the jointing between the cover glass and the casing of

the absorber, and the jointing between two collectors or between the collector and an adjacent envelope element. On-site assembly could be a possible solution limiting and designing that joint according to the architectonic features. From that point of view, the new available thin collector based on triple glass technology allows to use same frame typical of windows reducing the visual impact of jointing.

Regarding dimension customisable opportunity are available and main limits could be related to the glass cutting process for flat plate collectors. Actually, some difference concerns the fluid energy carrier, generally for water driven component dimensions flexibility is mainly affected by the hydraulic system of the absorber. Interesting researches dealt to this topic and roll bond technology, nowadays available at low cost, is one of the most interesting option. It consists in rolling two aluminium sheets together under high pressure while letting the hydraulic channels free to be "blown up". Different patterns are consequently available optimising heat transfer to fluid while obtaining variable absorber plate shape and finishes, ***Fig. 15***.

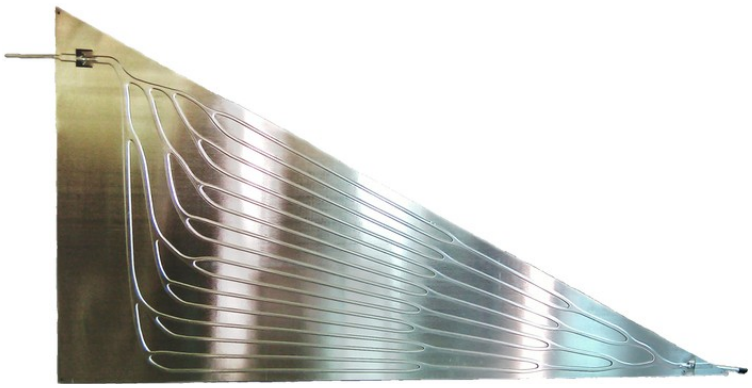

Fig. 15 Absorber plate based on roll bond technology by Fraunhofer Institut

This last consideration leads to the next two criteria for integration evaluation: colour and finishes. Actually, thin film and selective varnishes open way to coloured collector minimising efficiency loss. Even that some differences in colour opportunities exists between glazed and unglazed collector due to the fact that the absorber in unglazed collector is directly exposed to weathering and durability of finishes has to be provided. Only thickness insensitive spectrally selective (TISS) paints are then available for unglazed collector reducing the colour options, ***Fig. 16***.

Contrariwise, for glazed collector two possibilities exist: colouring the absorber or colouring the glass completely hiding the plate. This visually non-transparent element could be used as covering for the active element and as merely cladding for the non-optimally exposed areas of the building envelope, optimising aesthetical results.

Finally, silk printing technology could be easily used for obtaining a good appearance even if efficiency could reduce drastically.

Fig. 16 On the left, TISS palette developed by the National Institute of Chemistry of Ljubljana. On the right Various shades of acid etched coloured glasses

Regarding colour it is worth to notice that different colour and consequently different reflectance spectra affects the collector performance. In this regards, Anderson et al **[42]** carried out experiments on glazed collector with different colour-coated mild steel absorber, specifically black, grey, green, red and white finishes were detected. Theoretical results, once (ta), FR and UL are calculated, are shown in ***Fig. 17***.

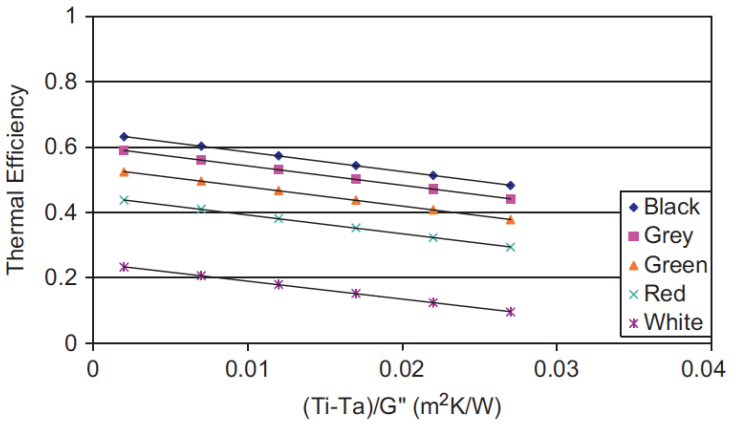

Fig. 17 Efficiency variation while change absorber colour from Anderson et al.

Finally, regarding evacuated tube technology, they are made adding autonomous energy collection elements and this make them different from glazed and unglazed collector.

Generally, they have been used as extra or complementary elements to the envelope by generate a double skin over the opaque envelope with an own structure or by replace shading devise or balcony eaves. Even that the possibility to orientate the absorber in the tube independently of collector orientation allows the horizontal mounting without affecting efficiency. Meanwhile dimensions could be customised with regards to the length of tube and to the distance between them; finally jointing issue mainly relates to the manifold element. Colour options are not of particular interest as well as finishes.

Researches activities and building integration goal

Since now, traditional collector design has been analysed and influences on architectural features outlined. Other line of research regards the new design of collector specifically aimed to obtaining products that are at the same time a building component and a solar thermal collector. What is different in this paragraph is the design approach: specific building component are analysed and solar collector function introduced as additional function; meanwhile previous section deals with standard collector adapted to a specific building component function.

Lobaccaro and Wall **[47**] outlined the main research carried out by institutes and universities involved in IEA SHC Task 41 in collaboration with companies. It is worth to notice that many efforts have been done regarding the development of new PV products/system among the organisations taking part in Task 41 but only two solar thermal component suitable for roof integration have been studied by the Australian National University but actually they don't strictly deal with the integration topic from a architectonical/technological point of view. Specifically, these studies regard a solar air heater with PCM thermal storage able to produce also solar hot water and PV electricity in one array. The other research deals finally with thermally driven compressor operating in a heat pump refrigerator cycle.

Nonetheless, some interesting results come from the database by Task 41 – Solar energy and architecture: "Innovative solar products for building integration" [http://leso2.epfl.ch/solar/index.php?page=solarthermal].According to my personal opinion, the most interesting studies for their innovative approach to the problem belonging to that database and to research worldwide have been summarised in tab. 2, tab. 3, tab. 4.

Some of them are really new such as the roof solution for glazed and unglazed tiles or for gutter in tab. 2 some other like the new shape from Visa et al. **[57]** shows how simple change in the geometry of the existing technologies could give more possibility in architectonical integration.

tab. 2 Roof Integration

SolTech Sigma – ST GLAZED FLAT PLATE COLLECOTOR [http://leso2.epfl.ch/solar/index.php?page=solarthermal].

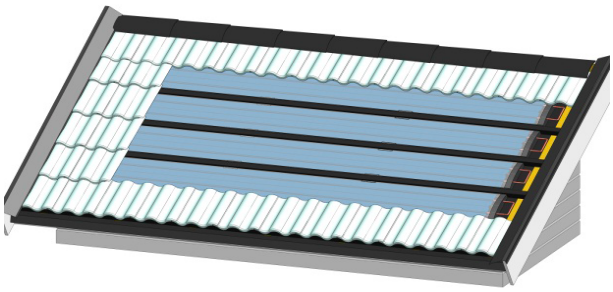

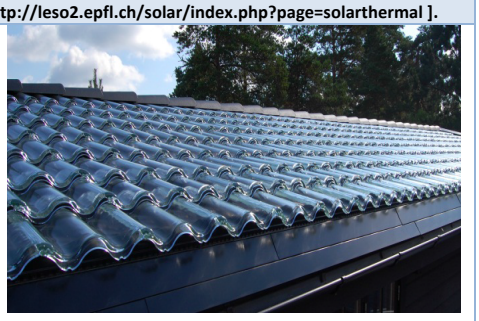

Biberschwanz/Classic – ST UNGLAZED [http://leso2.epfl.ch/solar/index.php?page=solarthermal].

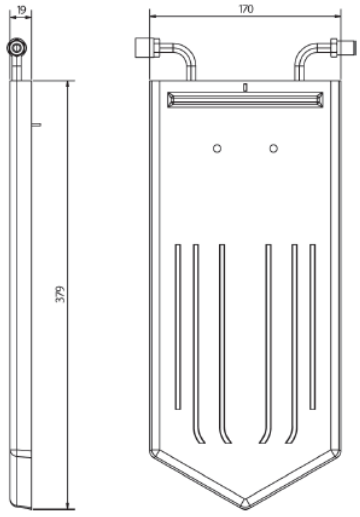

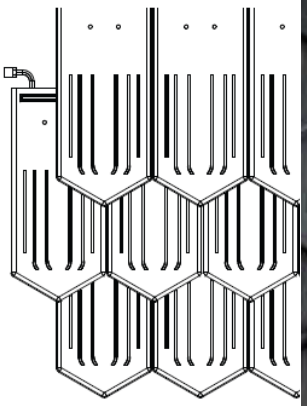

Solar rainwater gutter by Motte et al. [49]

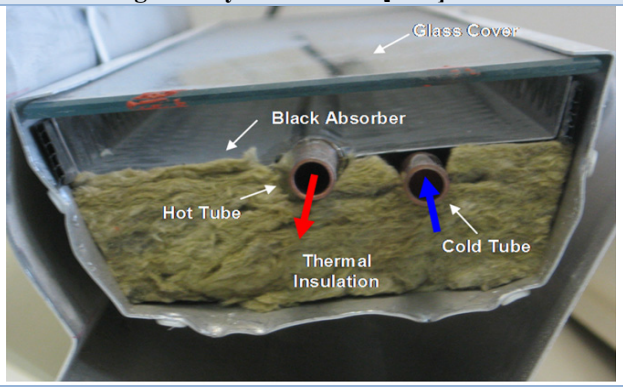

tab. 3 Building envelope integration

Asfalt Roofs [http://leso2.epfl.ch/solar/index.php?page=solarthermal].

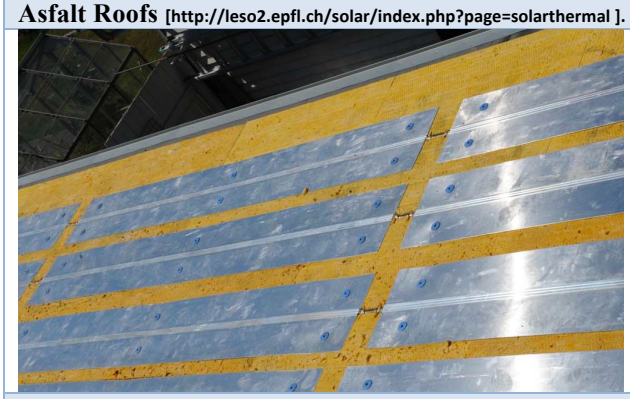

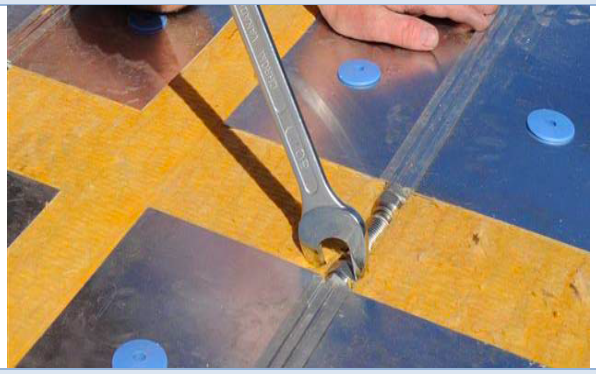

TECU® Solar System [http://leso2.epfl.ch/solar/index.php?page=solarthermal].

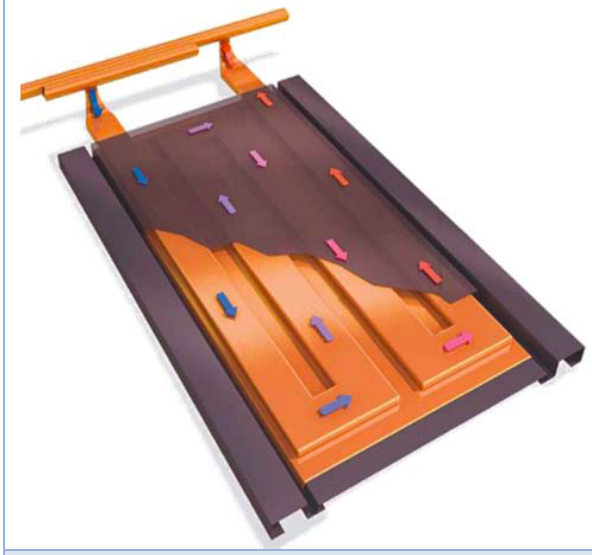

New geometry by Visa et al. [57]

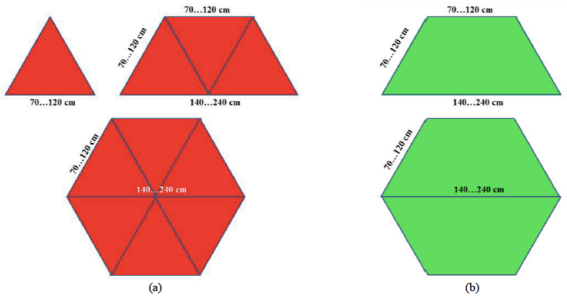

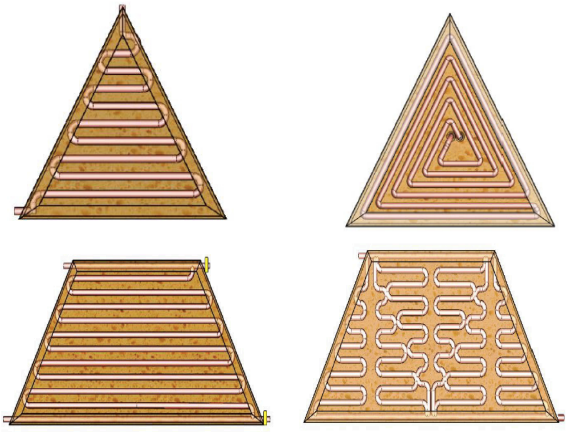

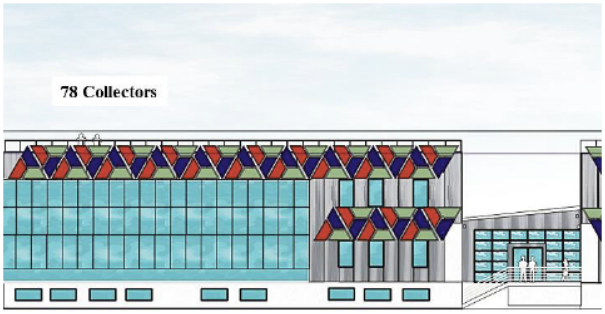

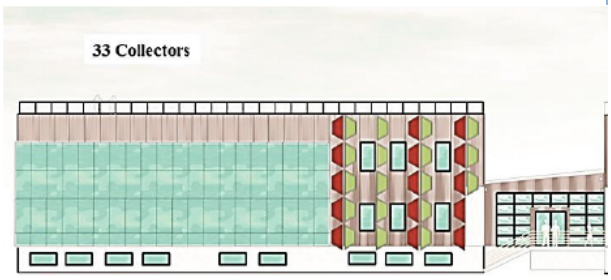

tab. 4 Shading/balcony integration

SWISSPIPE Balkone – ST GLAZED FLAT PLATE [http://leso2.epfl.ch/solar/index.php?page=solarthermal].

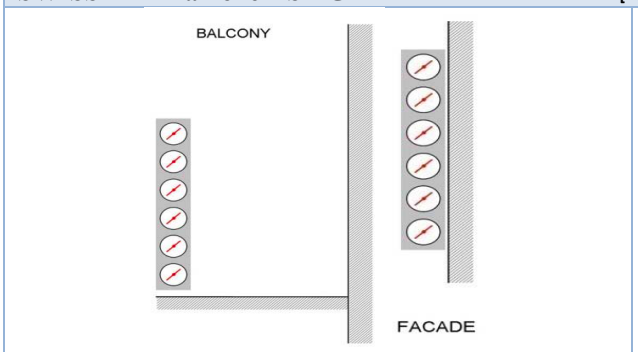

RobinSun Solar Thermal Glass [http://leso2.epfl.ch/solar/index.php?page=solarthermal].

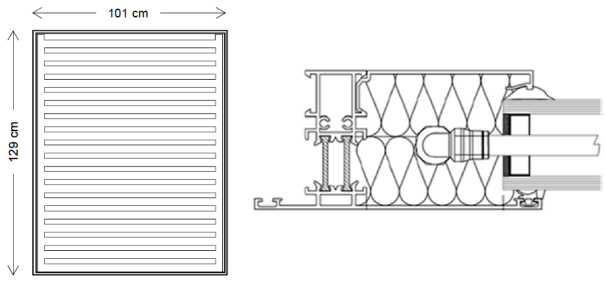

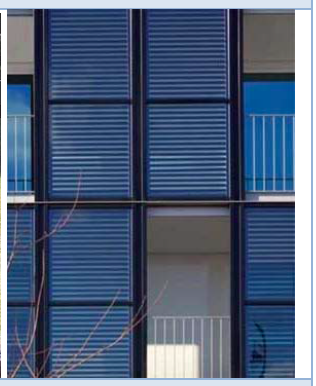

Solar louvre collector by Palmero-Marrero and Oliveira [54]

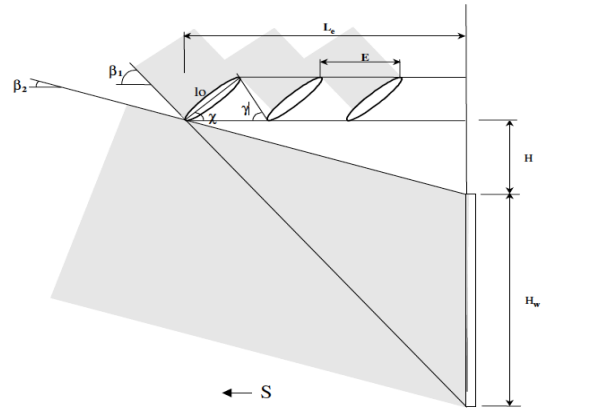

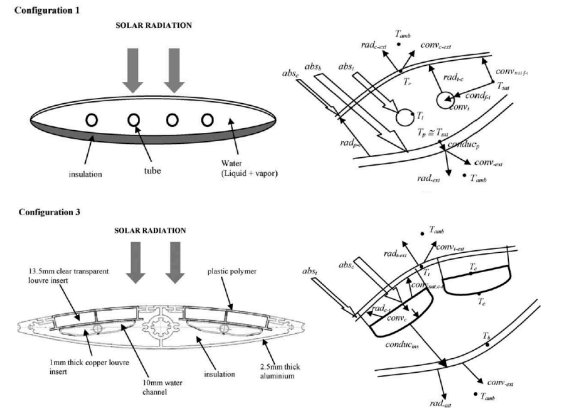

PV/T hybrid solar window by Davidsson et al [45]

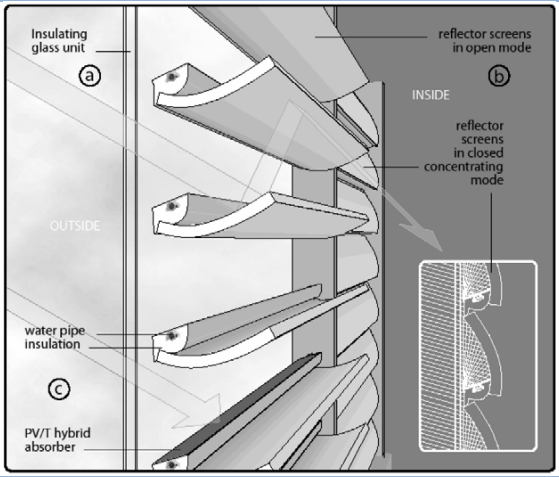

Worldwide

Finally, one interesting notice comes from a worldwide point of view. Particularly, the China Government has recently promoted a 5-years research project with the purpose of developing key technologies involved in the integration of solar thermal systems with buildings **[58**]. And many researches have been carried out in this field and in the generic topic of solar thermal technologies. The green buildings of Shanghai Research Institute of Building Science (***Fig. 18***) have been used as test case for a 2-years experimental campaign **[62**] **[59**]. The main idea was to provide a solar-powered integrated energy system involving heating, air-conditioning, natural ventilation and hot water supplying, which realizes high integration of solar thermal technologies, and therefore increases utilization ratio of solar system. Wang et al., **[59**] demonstrated how under the climate condition of Shanghai, 150 m2 vacuum tube solar collector arrays can be used to satisfy heating and air-conditioning for covered area of 460 m2. Other researches include the design of prototype such as the all ceramic absorber (***Fig. 18***) from Sun et al. **[60**] and Yang et al. **[61**] whose aim was to give a low-cost solution for the absorber. Anyway, no real attention has been done in the topic of building integration as outlined in previous sections but it is interesting to notice how attention on solar thermal technology is spreading also in the new world economy as the choice of the 2014 venue for the "International Solar Heating and Cooling for buildings and industries" has demonstrated.

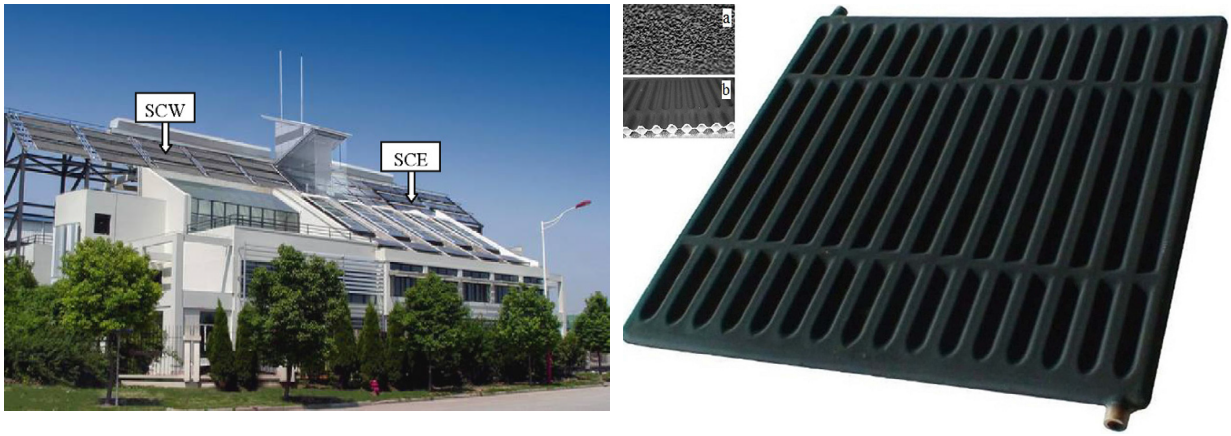

Fig. 18 Researches in China.
On the left green buildings of Shanghai Research Institute of Building Science.
On the right the all-ceramic prototype.

1.3 Conclusion

Different approaches to the problem have been investigated all along this chapter and some interesting notices could be summarised. First of all two attitudes are distinguished in the new concept design:

1. Analysing the existing building component and try to understand how they could be adapted to the solar thermal function.
2. Analysing the existing collector technology and try to understand how they could act as a building component from a technological point of view.

Actually building integration is not a merely technical problem regarding from one hand collector efficiency and from the other hand building envelope functions but it also deals with other instances such as aesthetic quality and collector fitting on available building surface, overall when energy refurbishment goals are addressed. Aesthetical quality is actually an important goal also for the acceptance of solar thermal technology by architects and owners and will for sure give a contribution to the spread of the technology itself. Many efforts have been done starting from these approaches and, according to my opinion, tab. 5 summarised straightness and weakness of available solar component in terms of integration outlining what needs some further deepening ("-" in the table). Nonetheless what seems to be almost a lack and what will be the topic addressed by the present work is the thermal evaluation of the integrated system taken as a whole element with the building component.

tab. 5 Available collector technology and integration

	Glazed Flat plate	*Unglazed*	*Evacuated tube*
multi-functionality	+	+	-
joint	-	-	0
dimension	+	+	+
colour	+	-	0
Visible surface textures and finish	+	-	0

according to author opinion: positive judgment + ; negative judgment -; indifferent 0

2. THESIS OUTLINE AND GOALS

As outlined in INTRODUCTION, present work employs the results of two prototypes (addressed as Prototype A and Prototype B) that have been tested at the Università degli Studi di Palermo - DEIM for validating two FEM models. Once these models are ready, calculations are run integrating the prototypes in a typical wall structure (STC-wall A and STC-wall B) in order to sort the corresponding efficiency curves answering essentially at the following questions:

1. **How collector efficiency changes if the collector is a building integrated component?**
2. **How a solar-thermal integrated collector affects energy exchange through the building envelope?**
3. **How much active/passive STC-wall affects the overall building energy balance?**

As obviously cooling and heating seasons needs separately analysis as well as it is necessary to consider the influence of climate in the STC-walls performance. It is consequently necessary introducing a reference building located in a specific site. Definitely present work refers to a research carried at the Politecnico di Milano in 2009-2011 concerning the characterisation of building stock in Milan for energy refurbishment strategy **[16**] and to the advisement document presented in 2003 by CTI (*Comitato Termotecnico Italiano*, Italian Thermo-technical Commitment) in which most common building envelope structure in Italy with reference to the region and to the age of the building are presented **[17**].

2.1 Reference collectors

The main idea of the analysed two prototypes is to use component easily available in the market at small price in order to obtain low cost solution for air pre-heating. The research carried out during summer 2011 and summer 2012 led to two different configurations being the prototype B the spontaneous development of the basic low cost idea driving at first prototype A realisation.

Prototypes description

Main idea of both configurations is the use of common sandwich corrugated panel, easily available in the market at really small price. It is a prefabricated panel composed by an insulation core (high density PUR, k=0,024 W(mK)$^{-1}$) that is enclosed by two metallic layers made up in aluminium or steel. This panel is characterised by standard width (generally 1m) and standard corrugation aspect, while other dimensions such insulation thickness and panel length are customisable as well as colour coating. Typical offered insulation thicknesses are from 30mm up to 100mm and blue, green and red tones finishes could be generally chosen (***Fig.* 19**), it is worth to notice that recently modules assessed for PV-panel integration are also available. Accessories for fixing the panels at roof and façade structures are specifically designed while if the frontal profile is observed in ***Fig.* 19** it is visible how different modules could be coupled together; all these aspects make this kind of panel attractive in the market for building finishes.

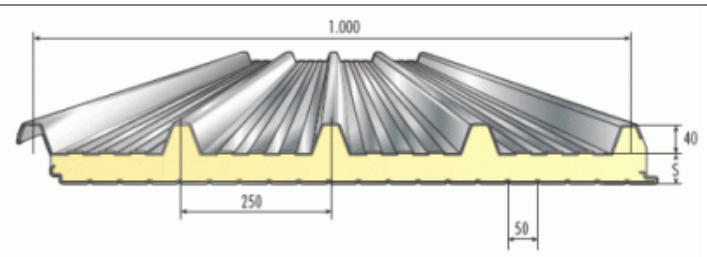

RAL 7016	Grigio antracite	RAL 9002	Bianco grigio
RAL 6005	Verde muschio	RAL 3009	Rosso Siena
RAL 9006	Silver	RAL 8017	Testa di moro

Fig. 19 *Sandwich corrugated panel. On the left the main common dimensions (from Alubel catalogue), measures are expresses in mm; on the right the panel used for building up the prototypes.*

Specifically, both prototypes are equipped with 2,5m length module characterised by 40mm insulation depth and brown paint. Metal insulated profiles are fixed at the panel perimeter by screws and are suitable for enclosure the module and fixing the glass cover.
According to the low-cost idea simple glass cover is provided and no selective thin-layer used in order to verify the maximum efficiency level achievable with the minimum cost.

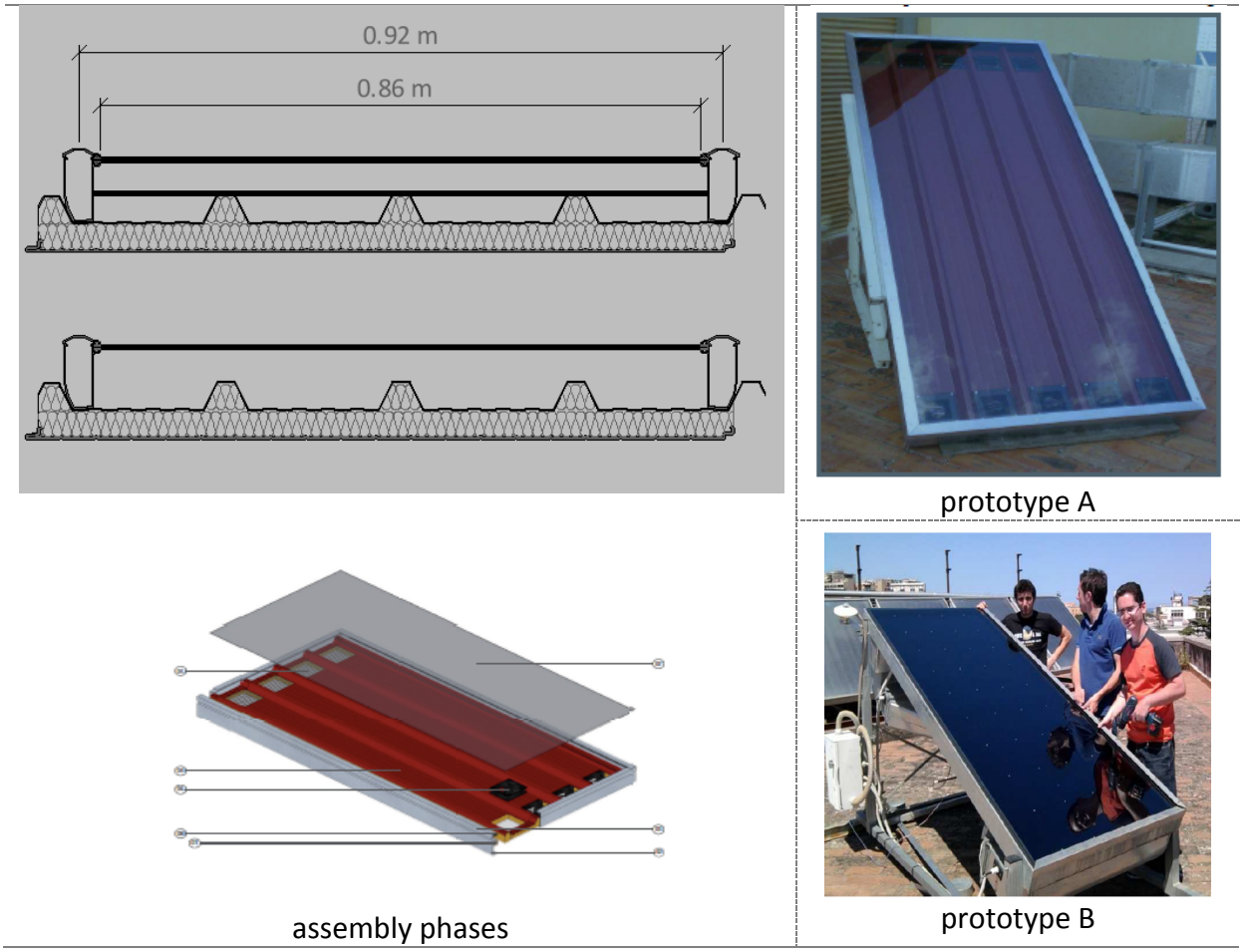

Fig. 20 Prototype A and Prototype B comparison. On the left, sketch of design detail and assembly phases. On the right, pictures of the two solar collector prototypes.

In order to improve efficiency in the second phase of this background research a change in configuration of prototype A occurred and led to configuration B. A selective layer was then fixed on the panel corrugation displacing the absorber function from the prefabricated panel to the new layer; at the same time at fluid level, the single channel between glass cover and plate in the previous configuration gives way to 4 air channels and to an almost steady-state air gap governed by natural convection that improves top resistance reducing energy losses through the cover. Actually, fluid flow is optimised introducing a fin effect while maintaining

at least the same surface of contact between the hot boundary of the channel and air. Moreover the flow channel section area is reduced from 661cm^2 in prototype A to 304 cm^2 in prototype B.

Furthermore, a TiNOX layer was chosen as absorption plate and fixed on the panel corrugation without affecting significantly the cost. TiNOX is a selective coating whose thicknesses is about 1.250 mm composed by different nano-layers, each one with a specific radiative or protective function, that are bonded at an aluminium or copper substrate. The main thermal characteristics is its higher absorption (0,95) at wavelengths between 380 and 2500 nm corresponding to almost the totality of solar radiation and its lower emittance (0,05) in the IR band corresponding to the emittance band for a black absorber at 100°C. This coating then allows to catch the almost totality of the solar radiation and to embody it, diminishing the radiative losses through emission phenomena.

New configuration allowed to obtain better thermal performances and is still topic of research at DEIM: the TiNOX layer was partially substituted by a PV panel leading to a configuration C that is not anyway part of present work.

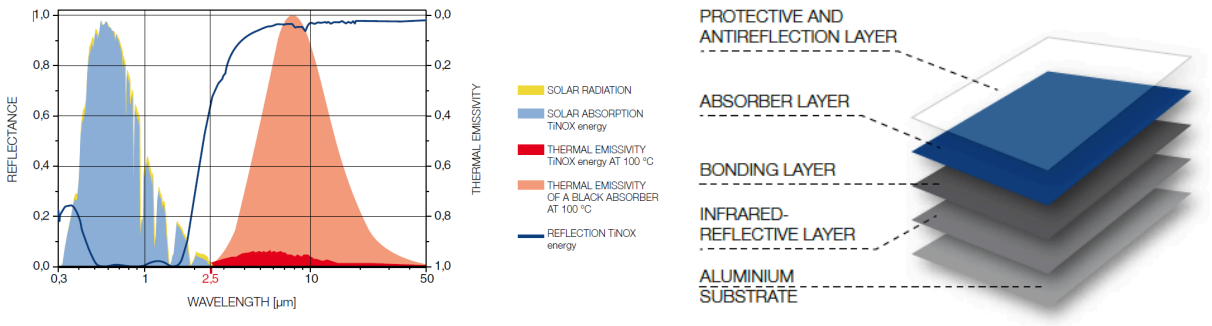

Fig. 21 TiNOX-energy coating, from Almeco catalogue. On the left, typical spectra for the coating compared to solar radiation and black absorber emission at 100°C.
On the right, TiNOX energy layers structure.

Experimental campaign

After prototypes were built up, experimental campaign took place and measures for sorting collector efficiency were detected according to the key regulations **[18]** **[19]**, **[21]** which will be presented chapter 3. The tested collector were mounted at the roof of the department, south oriented (±2%) with a slope equal to 45° ±5°. The place was chosen in

order to let wind freely pass all around the collector itself and only data at wind speed less then 5 ms^{-1} are considered. Sensors were mounted on the structure for measuring external solar irradiation on the collector plane while other PT100 sensors are put in the module for detecting temperature at the significant point (inlet, outlet, middle channel). Hot-wire anemometer were useful for assessing the working flow rate (***Fig. 22***). Moreover, fans provide the desired inlet flow rate while an electrical resistance is put at inlet section in order to manage the inlet temperature as prescribed by regulation.

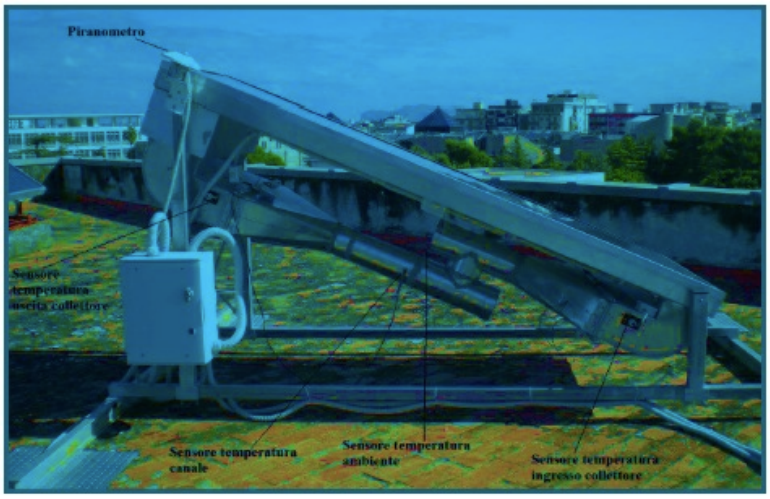

Solar radiation:
LP-PYRA-02-V by DeltaOhm
field of measure: 0-2000 Wm^{-2}

Air Temperature:
PT100
accuracy ±0.3°C

Flow rate:
Hot-Wire Anemometer
(HD29V37C32 by Delta Ohm)
field of measure: 0.1-0.2 ms^{-1}
accuracy of interest: ±0.4ms^{-1}
+3%

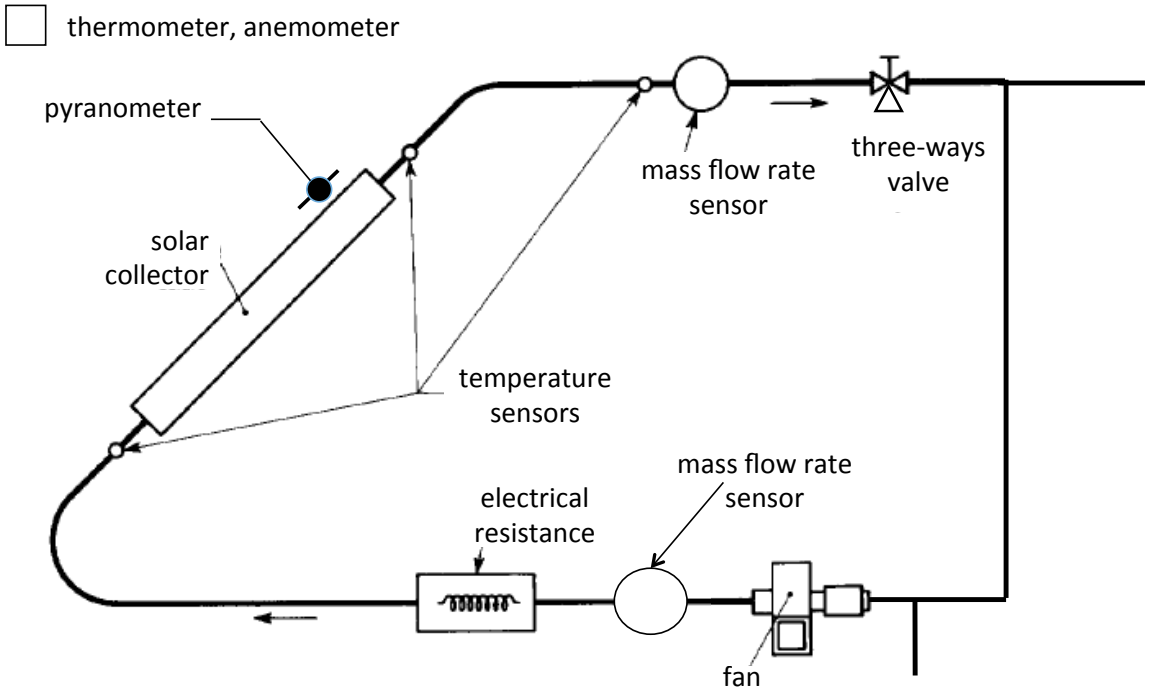

Fig. 22 Monitoring system sensors set up.

A dimmer (Mod. K8064 by Velleman) allowed to vary the outlet tension of electrical charge from 0Vac to 230 Vac governed by the acquiring module ADAM 6024. Two Advantech modules (ADAM 6015 for PT100 measures and ADAM 6024 for solar radiation and flow rate) acquired all data. Two PID controllers are used for obtaining the desired inlet temperature acting on the power of the electrical resistance and having the desired inlet flow rate acting on the fans rotation speed. Data were acquired with a time step equal to 30s and measures took place during morning at increasing solar radiation condition and during afternoon at three different flow rate (240 m^3h^{-1}, 155 m^3h^{-1} and 90 m^3h^{-1}) in order to sort efficiency curve at different speeds. Data in the time interval higher then 15 minutes characterised by almost stady-state test conditions are considered for obtaining reliable results. Even that instantaneous fluctuations for flow rate are logged and mean value for fluid rate is considered in the calculation. For each test condition four different inlet temperature are provide at 28°C, 35°C, 40°C e 45°C; two different measure are recorded for each inlet temperature and test conditions, so that 16 point in the efficiency diagram are available for defining the efficiency curve.

Results

Actually, no direct comparison between prototypes is available since they efficiency curves belong to different inflow rate. Even that the inlet flow rate is quite different for test regarding prototype A and test regarding prototype B inducing not to associate directly the sorted efficiency curves although the order of magnitude is comparable and some reasoning are possible. First of all, as aspect and as reported in ***Fig. 23*** prototype B has better performance with respect to previous configuration. Generally, the intercept term for prototype B varies from 65% at the maximum provided flow rate (m= 270 kg/hr) to 41% corresponding to 100 Kg/hr.

Prototype A was working at a maximum flow rate equal to 180 kg/h comparable with the medium flow rate for prototype B (η_{max}=52% at 165 kg/hr) and a reduction about 5% between the two conditions is recorded while maximum efficiency for prototype A varies from 48% to 30% at the minimum flow rate equal almost to 30 kg/hr. Moreover the x-axis interception lies between 0.03-0.04 for all cases showing good performance during summer condition.

Present work will address these prototypes and the corresponding experimental data were used for validate a FEM model aimed to obtain efficiency curve at standard and normalised inflow rate and to obtain further efficiency curve corresponding to a building integrated component.

prototype A – maximum flow rate

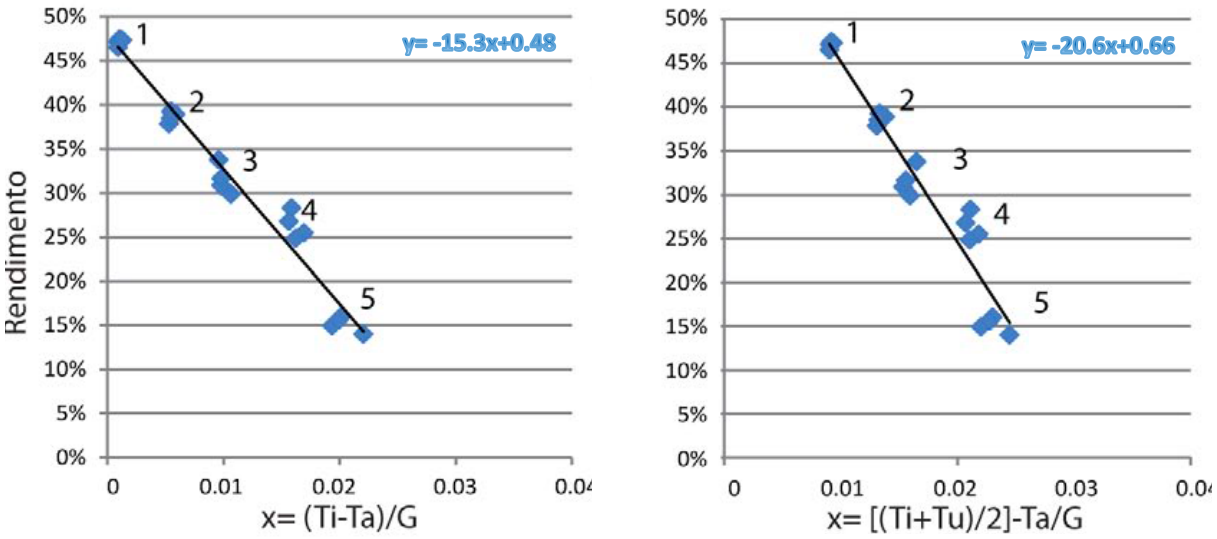

prototype B – maximum flow rate

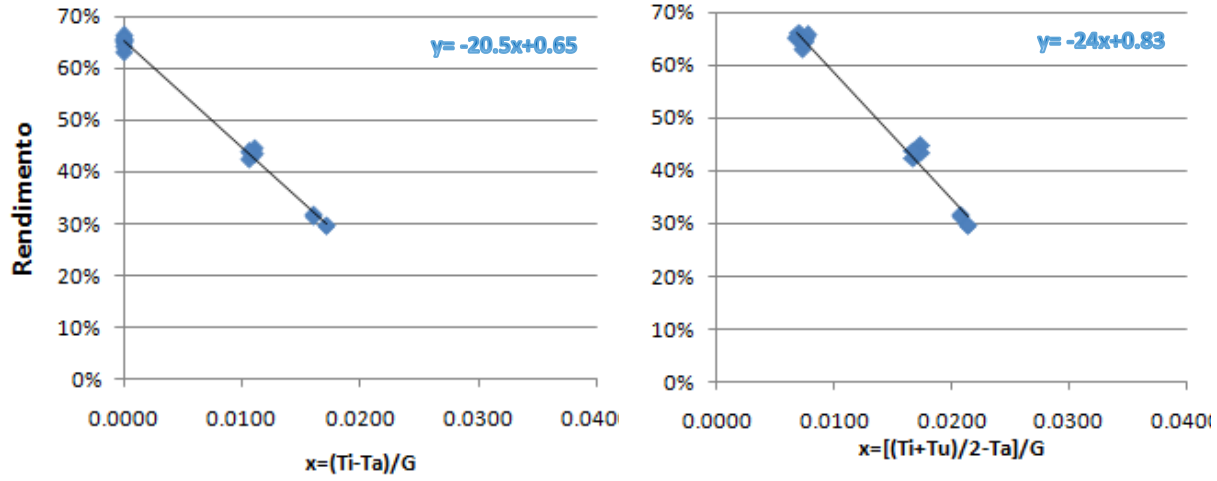

Fig. 23 Efficiency curve belonging to the experimental campaign at maximum inlet flow rate.

2.2 Building Integration: technical feasibility and assumptions.

It is worth noting that according to building integration purpose in energy refurbishment approach, the proposed prototypes are particularly suitable and match the aim of present work. If the typical Italian building is considered this kind of system could be easily fixed on façade creating a collector string between windows series while providing a external insulation layer for the whole wall, as shown in ***Fig. 24***. Two possible fitting technologies are assumed at first: the sandwich-corrugated panel is directly fixed in wall structure by screws creating a conductive thermal junction; some spacers create an air gap between the panel and the wall. In the latest case, the thermal joint between the two components is a convective/radiative dominated system, so that additional resistances have to be introduced influencing results while adding other variables. Present work deal to the first assumption for stressing attention on STC-wall effects at building envelope heat transfer level. For the same reasons, it is supposed that the windowed façade is south oriented and enclose only one thermal zone, so that heat transfer through the modified wall directly affects the overall building balance.

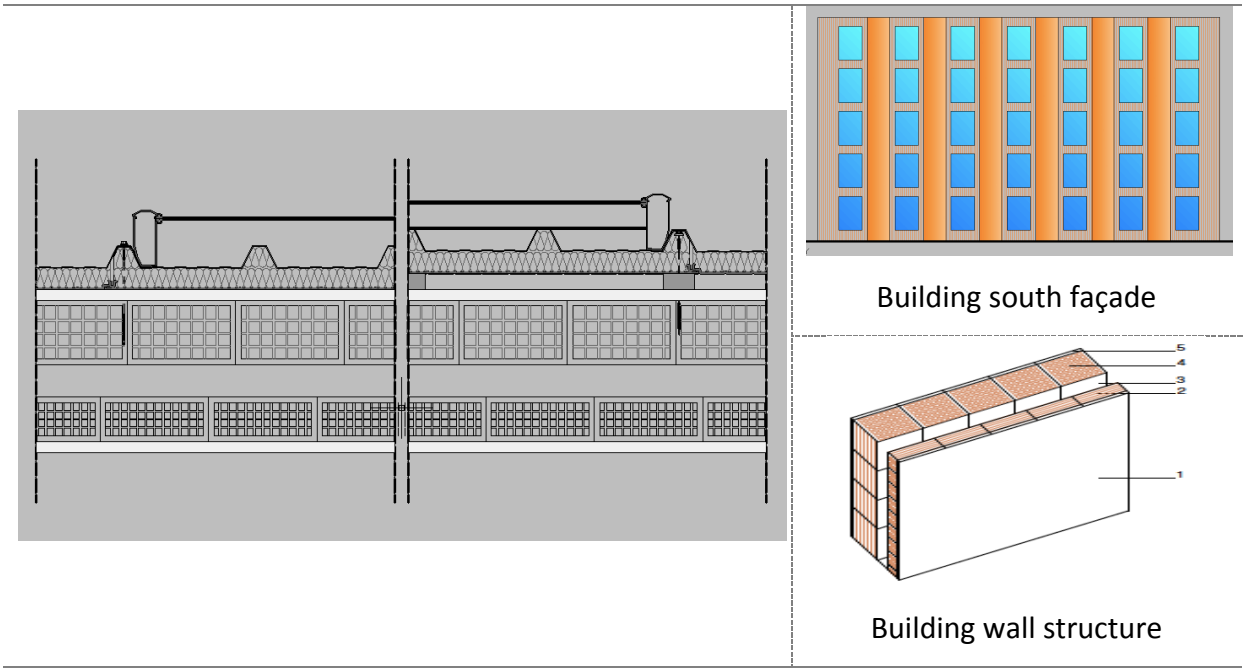

Fig. 24 On the left, proposal for building integration at structural detail level. On the right, scheme of the reference building façade characteristics at architectural and detail level, a proposal for building solar thermal system integration at façade level is draft in façade.

At thermal plant level, it is reasonable to suppose STC-component provide pre-heated air for conventional air change per hour during winter. It means that a distribution network for air is already available in the building or it is feasible to build it up. Two different scenario are possible: each apartment has an independent heating plant and it will be directly connected to a single thermal solar component; a centralised heating plant characterise the building and the air heated by a string of components assembled in series converges in the ATU. Present work deals to a centralised plant in order to evaluate the overall benefit of such a refurbishment strategy.
Summarising following assumption are introduced:

1. **the reference building [16] is located in three climatic-different cities in Italy;**
2. **the STC-walls are directly fixed at the façade structure;**
3. **the heating building plant is a centralised one and collector string are used for pre-heated air during winter season for provide the minimum air change per hour;**
4. **during cooling season, heated air is thrown away and only passive effects on building balance evaluated.**

2.3 First approach to the simulation model: case-study qualitative overview

Basic hypothesis is that the sandwich panel is directly fixed at the wall structure, a first comparison at thermal level among the stand-alone collectors, the wall with only a fixed corrugated panel and the integrated STC-wall A and B is proposed by an electrical analogy, see ***Fig.* 25** were following system are proposed:

- a merely insulated wall,
- the not-integrated collector in configuration B
- the integrated solar collector in configuration A.

Let's say the three system are enclosed by BND_up and BND_down, for solving the system convective/radiative heat fluxes defines BND_down have to be defined as well as T_{plate_1} is chosen for describing outdoor conditions at BND_up.

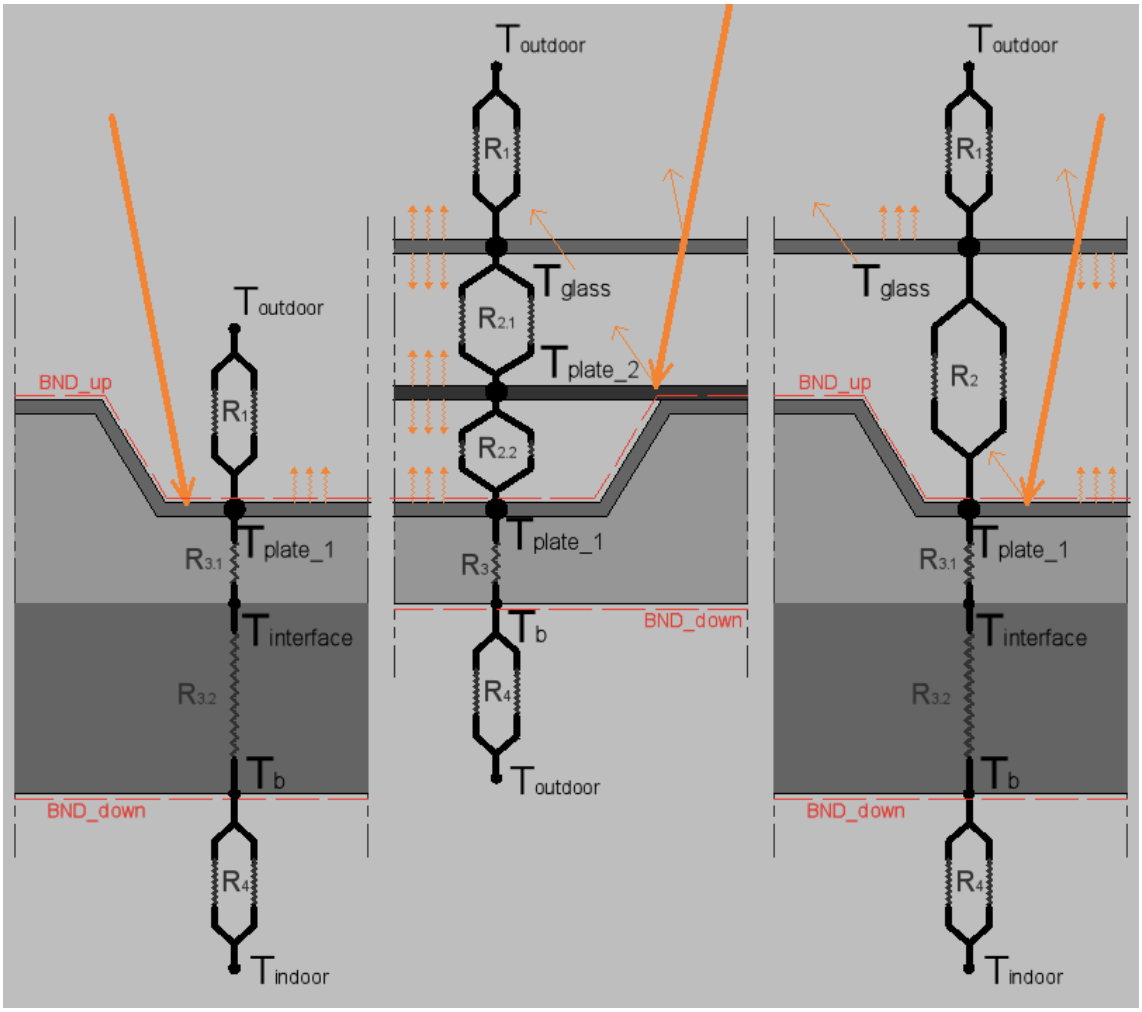

Fig. 25 *Electrical analogy in term of conductive, convective and radiative resistance. A comparison among prototype A and B in different boundary condition is also proposed.*

Differences between the detached prototype and the integrated one as well as between the merely wall and the STC-wall are manifest and obviously. Down boundary radiative/convective fluxes could be easily express as function of out-boundary temperature by means of heat transfer coefficients provided by UNI EN ISO 6946/1999 **[24**], supposing temperature surface could be approximated at the ambient air temperature. Main difference stays in collector performance evaluation between integrated and detached one: the first borders on an ambient at fixed condition while the second bounds with outdoor ambient extremely variable both in temperature and in wind speed-direction that affects the convective resistance value. More evident is the up boundary difference among the analysed systems. Main difference is notice between merely wall and STC-wall; first of all an incoming heat flux (irradiation) passes the boundary and enters the system in both cases.

Nevertheless, the same solar source is on one hand filtered by glass and at the same time improved by reciprocal radiative exchange between surfaces in the IR band. Moreover the characteristic temperature at the close out-boundary is different from the merely wall and the STC-wall: once again it is reasonable to consider outdoor temperature for both convective transfer and radiative exchange in first system; meanwhile fluid temperatures and upward surface temperature in the second system are needed and are different from $T_{outdoor}$, for sure. One notice regards finally the configuration A and B of prototype, in the latter, as matter of fact, all these described phenomena are mediated by a second intermediate layer (TiNOX absorber plate) hence no fraction of solar radiation enter the system directly but according to achievable T_{plate_2} temperature radiative exchange increases as well as the fluid temperature. Finally another note regarding the system itself while comparing the merely wall and the STC-wall, an additional resistance is introducing in the second system ($R_{3.2} = \sum s/\lambda$) increasing the value about 36% from the solar collector to the STC-wall configurations.

Having analysed the systems and in order to compare them according to present work goals, following steps are taken into account:

1. FEM models of STC-wall A and B are built-up for solving the system investigating all the T_{node} temperatures in specified ambient conditions and for characterising at the same time the two collector performances by means of their efficiency curve;

2. The interface temperature is chosen as key-point for solving the whole system and determining performances at building level by means of a TRNSYS model built on the reference building in different configurations.

It is worth to notice again that only south façade is matter of present work, as a deliberate intention for stressing attention on STC-wall effects on building energy balance.

3. PHYSICS OUTLINE: heat transfer phenomena in the STC-wall

Present chapter deals with main physics knowledge suitable for characterising the FEM model and that were matter of the three years study program.

3.1 Radiative Heat transfer topic

Thermal radiation

Thermal radiation could be regards as electromagnetic phenomena where waves coming from a source propagate in a medium (solid or liquid, without any respect) or even in vacuum. Generally body's surfaces continuously emit electromagnetic radiation according to its local temperature and properties; for that reason they could be considered as a receiver as well as a source, ***Fig. 26***. From a radiative point of view, the way they behave and the resulting achieved temperature depend on the surface characteristics; hence radiative properties depend exclusively on layer finishes and are generally affected by the wavelength and the direction, so that they are not strictly material properties but merely properties of surfaces with a own spectral distribution. Moreover, since no real isotropic surfaces could be found these properties varies also with the surface location. At the same time it is possible to distinguish between properties for real and ideal surfaces, the ending _*ance* instead of _*ivity* is generally use for indicating the first group.

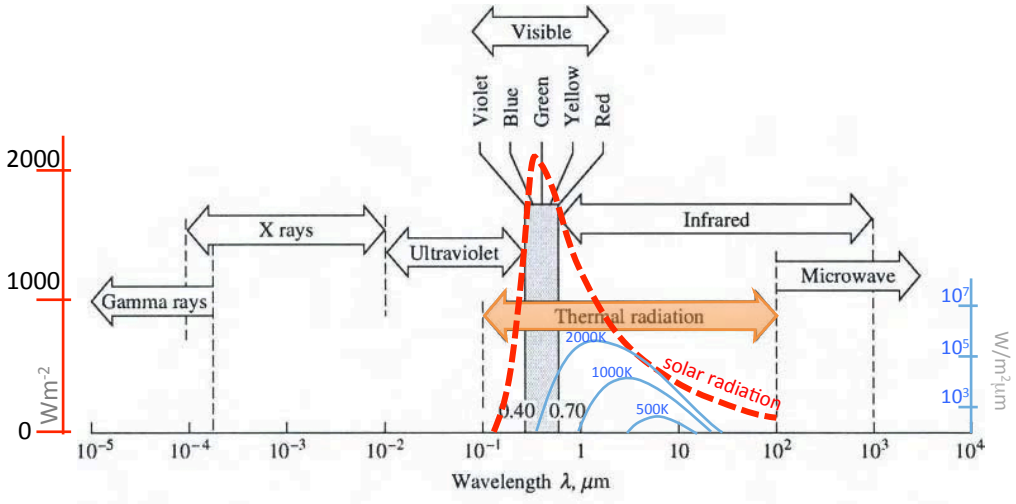

Fig. 26 Electromagnetic wave spectrum (for radiation traveling through vacuum), standard spectral irradiance curve at mean earth-sun distance and black body emissive curves at different temperature.

When an electromagnetic wave traveling through a medium (or in vacuum) strikes a surface, it is partially reflected while the non-reflected fraction penetrates toward the other medium. Moreover, the wave is continuously attenuated depending on different phenomena, if this attenuation is complete then the medium is called *opaque*; otherwise it is called *semi-transparent* while if no attenuation occurs it is defined as *transparent* medium. Finally this phenomenon depends on the characteristic of the medium as well as on its thickness: so that metals, such as gold, are generally recognised as opaque media but it has been proved they are semi-transparent if an extremely *thin layer* is taken into account. Considering the overall phenomena, according to radiation balance and coefficient definitions the absorbed, the transmitted and reflected fraction has to be equal to the incoming one:

$$\alpha + \tau + \rho = 1$$

where α stays for coefficient of absorption, τ transmission and ρ reflection; they are defined as the ratio between respectively the absorbed, the transmitted and the reflected energy with respect to the incoming one, for more specifications see tab. 6.

When semi-trasparent media (such as glass and glazing system) are finally considered the attenuation phenomena depend on absorption but also on scattering contributions; so that others two coefficient has to be introduced:

1. the **absorption coefficient,** *k* (m^{-1}) referred to the media accounts for the amount of radiative energy that is converted into internal energy increasing the temperature of the media itself;

2. the **scattered coefficient**, σ_c (m^{-1}) that characterises the media and accounts for the amount of energy that is simply redirected and appears as an augmentation along another direction; depending on the angle of propagation. Some of this energy is finally trapped into the media (σ_c^+) while the other part finally passes toward the outside (σ_c^-)

For understanding scattering phenomena, it is necessary focusing on radiation interactions with particles. As shown in ***Fig. 27***, a photon reaching a particle could change its traveling direction by diffraction or could be reflected or penetrate into the particle changing is path by refraction. These three phenomena at particle scale are known as scattering; three different regime of scattering could be distinguished considering the ratio between the particle radius (a) and the wavelength ($x=2\pi a/\lambda$):

- $x \ll 1$: Rayleigh scattering, as for atmospheric air and sunlight.
- $x \cong 1$: Mye scattering
- $x \gg 1$: In this case the surface of the particle may be treated as a normal surface, and properties may be found through geometric optics.

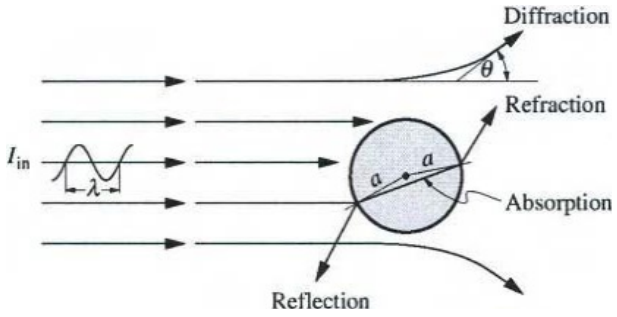

Fig. 27 Scattering phenomena sketch [8]

The absorption and scattering phenomena could be summarised introducing an **extinction coefficient**: $\beta = k + \sigma_c^+$. Specifically, the scattered phenomena is influenced by the dimensionless **refractive index** *n* that characterises the interaction between the two media and influences the way radiation passes from the one to the other, defining how a pencil of ray change its direction while passes through the layer between them. Moreover, the absorption coefficient k and the absorptance are related by the Beer´s law (or Bourgeur-Lambert-Beer´s low for absorption, see **tab. 8**) that relates the attenuation of transmitted energy due to the absorption phenomena to the properties k of the medium through which the radiative pencils are travelling.

tab. 6 Physics: radiative coefficients

Emittance could be defined as the ratio between the emitted energy from a surface at temperature T compared to the emitted energy from a black body at the same temperature.

$$e_\lambda = \frac{I_\lambda(T,\lambda,s)}{I_{b\lambda}(T,\lambda)}$$

where s stays for the direction, l for the wavelength and T for temperature. Some assumptions and simplifications could be done, taking the properties constant with respect to some variables. Indeed, generally the emittance is not so affected by the direction and is almost constant with respect to the angle with higher level for non-metal surfaces while rapidly drops to zero at $\theta=\pi/2$. So *hemispherical emittance* could be introduced as well as *Lambert´s diffuse surfaces* with good degree of accuracy. In the same manner, emittance could be considered spectrally constant introducing the *total emittance* value related to *gray surfaces* concept but this assumption is not always so suitable. Finally, *total hemispherical emittance* varying only with respect of surface temperature is often taken into consideration when semi-trasparent media are considered.

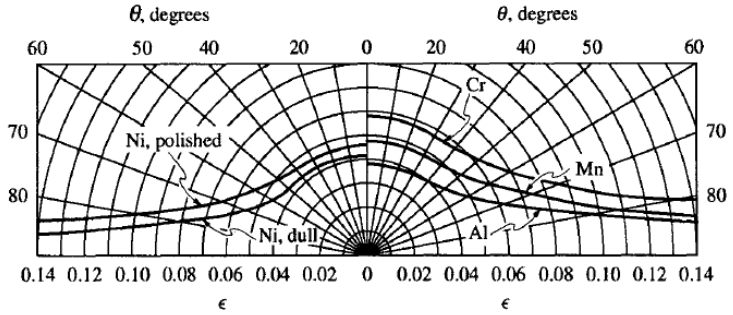

fig. 8 Directional variation of surface emittances for metal [8]

Spectral emittance

directional:
$\varepsilon'_\lambda = f(T,\lambda,s)$

hemispherical:
$\varepsilon_\lambda = f(T,\lambda)$

Total emittance

directional:
$\varepsilon' = f(T,s)$

hemispherical:
$\varepsilon = f(T)$

Considering the spectral directional irradiation, it follows:

$$H_\lambda(r,\lambda,s) = I_\lambda(r,\lambda,s)\cos\theta_i$$

depending on wavelength, directions θ and incoming flux (I), as an heat flux always pointing into the surface, **absorptance** is defined as the ratio between the absorbed radiative flux and the incoming irradiation:

$$\alpha_\lambda = \frac{H_{\lambda,abs}(\lambda,s)}{H_\lambda}$$

Moreover, if the thermal equilibrium is achieved in the surface and, if and only if, the incoming radiation is diffuse or collimated (such as for sun) a coefficient is constant and could be considered independent from the external radiation field. At the same time, the absorbed flux has to meet the emitted one, hence:

Spectral Directional Absorptance = Spectral Directional Emittance[(1)]

[(1)] The same follows for the hemispherical and/or total coefficients.

Spectral absorptance

directional:
$\alpha'_\lambda = f(T,\lambda,s)$

hemispherical:
$\alpha_\lambda = f(I_{\lambda,in}T,\lambda)$

Total absorptance

directional:
$\alpha' = f(I_{\lambda,in}T,s)$

hemispherical:
$\alpha = f(I_{\lambda,in}T)$

Similarly to the other properties **reflectance** is dependent on wavelength but instead of them it depends also on two directions: the one of the incoming radiation (s_i) and the one of the reflected fraction (s_r). For this reason, considering the incoming radiation at a certain angle, the reflected fraction in all possible direction has to be evaluated; that reasoning has to be made for all the possible incident angles of incoming radiation and in each wavelength. Anyway, for the most of the practical purposes, it is possible to introduce a ***spectral hemispherical-directional reflectance*** defined as the ratio between the diffuse reflected fraction of the incoming radiation in such a direction and the incoming radiation at certain angle.

$$\rho_\lambda = \frac{H_{\lambda,refl}(T, \lambda, s_i, s_r)}{H_\lambda}$$

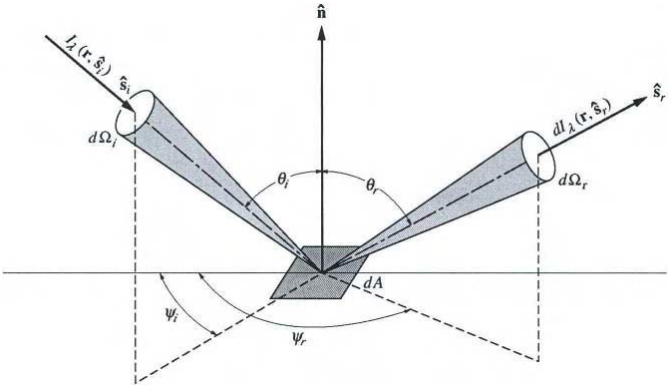

fig. 9 Bidirectional reflection sketch [8]

Spectral reflectance:

directional

$\rho''_\lambda = f(T, \lambda, s_i, s_r)$

directional/hemispherical

$\rho'_{\lambda,i} = f(I_{\lambda,in}, T, \lambda, s_i)$

hemispherical/directional

$\rho'_{\lambda,r} = f(I_{\lambda,in}, T, \lambda, s_r)$

hemispherical

$\rho'_\lambda = f(I_{\lambda,in}, T, \lambda)$

Total reflectance:

directional

$\rho'' = f(T, s_i, s_r)$

directional/hemispherical

$\rho'_i = f(I_{\lambda,in}, T, s_i)$

hemispherical/directional

$\rho'_r = f(I_{\lambda,in}, T, s_r)$

hemispherical

$\rho' = f(I_{\lambda,in}, T)$

The glazing system: Radiation through semi-transparent media, main coefficient

Glazing system has two main roles in the physics of the collector: allowing sun rays to reach and warm up the absorber plate and reducing energy losses by convection and radiation on the front of it. For these conflicted reasons, different kinds of covers could be taken into account and are generally used affecting the collector efficiency and costs.

From a phenomenological point of view, glass cover has to be considered as a medium through with solar radiation is partially reflected, partially absorbed (transformed into internal energy or trapped into the media) and partially transmitted beyond it.

Considering the typical dimension of glass panel is larger enough comparing to the wavelength of incident light radiative geometric optics and ray tracing methods could determine properties of glass system, tab. 7.

tab. 7 glass optical properties for theoretical calculation	solar trasmittance	IR emissivity
low iron glass	0.90	0.84
low iron antireflective glass	0.96	0.84
AZO(*)/low iron glass	0.85	0.30
AZO(*)/low iron antireflective glass	0.87	0.30
ITO(*)/low iron glass	0.84	0.20
ITO(*)/low iron antireflective glass	0.86	0.20

(*)*AZO= aluminium doped zinc oxide; ITO=indium tin oxide*

Consequently considering a generically glazing system, there are two interfaces per cover causing reflection losses and leads to a partial polarisation of the radiant flux. Taking into account for first the beam radiation, the transmitted energy is then proportional to a T-value (comprehensive value for all the slabs) that has to taken into account all the phenomena occurring through the glass media.

For calculating this value a simple model has been introduced taking apart the absorption phenomenon in the glass from the reflection phenomena among the surfaces separating the different media (air/glass; glass/glass and glass/air). Hence the overall T-value is proportional to the transmission related to reflections losses (τ_r) and to transmission related to absorption losses (τ_a), calculated as separated value:

$$T_{tot} = \tau_\alpha \tau_\rho$$

Neglecting at the moment the absorption phenomena inside the media. A single glass panel, facing air at both boundary layers (1, upper layer; 2, bottom layer) with identical reflectance (ρ) and transmittance (τ) values is considered, ***Fig. 28***. Then the incident solar radiation on layer 1 ($I_i(\theta_1)$) is partially reflected towards the outdoor spaces (r_{12}) and partially transmitted into the slab ($(1-\rho_{12})\tau$). This radiation travels through the glass media and reaches the second boundary layer according to the refractive angle (θ_2) for being partially transmitted through it while some other internal reflections according to Snell´s law (see **tab. 8**) occur toward the first boundary following the refraction direction.

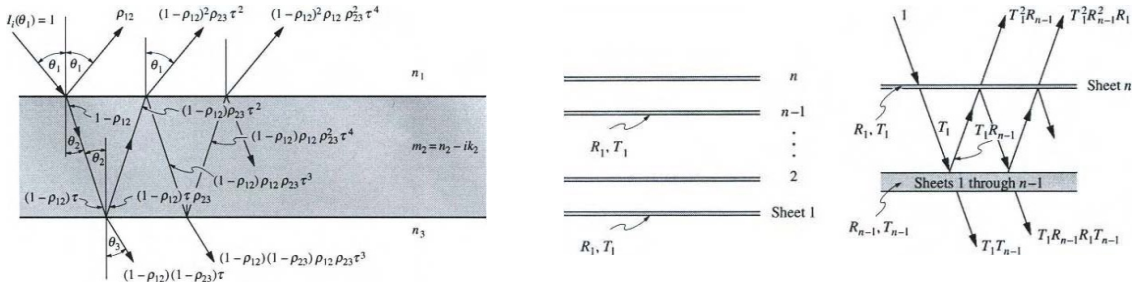

Fig. 28 Reflection interaction in single glass slab (left) and multiple glass slabs (right) [8] Modest M.F., *Radiative heat transfer*, 2nd ed., Academic press – Elsevier Science, 2003

These phenomena take place several times until all incoming energy is finally totally reflected back towards the medium 1, absorbed into medium 2 and transmitted to medium 3, but some simplifications could be introduced: interchanging n1 and n2 as well as θ_1 and θ_2 in the general equation could be easily demonstrated that the reflectivity at the 1-2 interface is the same, regardless of whether radiation is incident from Medium 1 or Medium 2 so that $\rho_{nm} = \rho_{mn}$. Moreover since media 1 and 3 are identical $\rho_{12} = \rho_{23}$. The total Reflection R-slab and Transmission T-slab coefficient are found out summing in a series the reflected and transmitted contributions, respectively. That two series belong and could be simplified considering that last terms are much lower than 1, this introduces finally:

- $R_{slab} = \rho \left[\frac{(1-\rho)^2\tau^2}{1-\tau^2\rho^2}\right]$
- $T_{slab} = \frac{(1-\rho)^2\tau}{1-\tau^2\rho^2}$
- $A_{slab} = \frac{(1-\rho)(1-\tau)}{1-\tau\rho}$

Finally, the absorption phenomena in the media 2 has to be counted considering Beer´s law, so the absorbed intensity is: $dI_a = -I\,k\,dx$ from which, integrating along the path dx = s cos(q_2), $I_a = e^{-kL/\cos\vartheta_2}$ and consequently $\tau_a = I_a/I_i$.

Dependence on wavelength. It is worth noting according to our purpose that these coefficients are wavelength dependant, ***Fig. 29***. Specifically, glass transmissivity tends to be very high between 400 nm and 2500 nm while it rapidly decreases beyond these two limits, so that glass could be considered almost opaque to IR and UV radiation. This means that a

very important fraction of the solar radiation could reach the absorber plate while IR emission in the collector cavity is trapped and a greenhouse effect occurs. Moreover, considering glass thickness, these coefficient are also influenced by absorption phenomena; but as the absorption coefficient is small for λ<2700 nm this effect is rather minor.

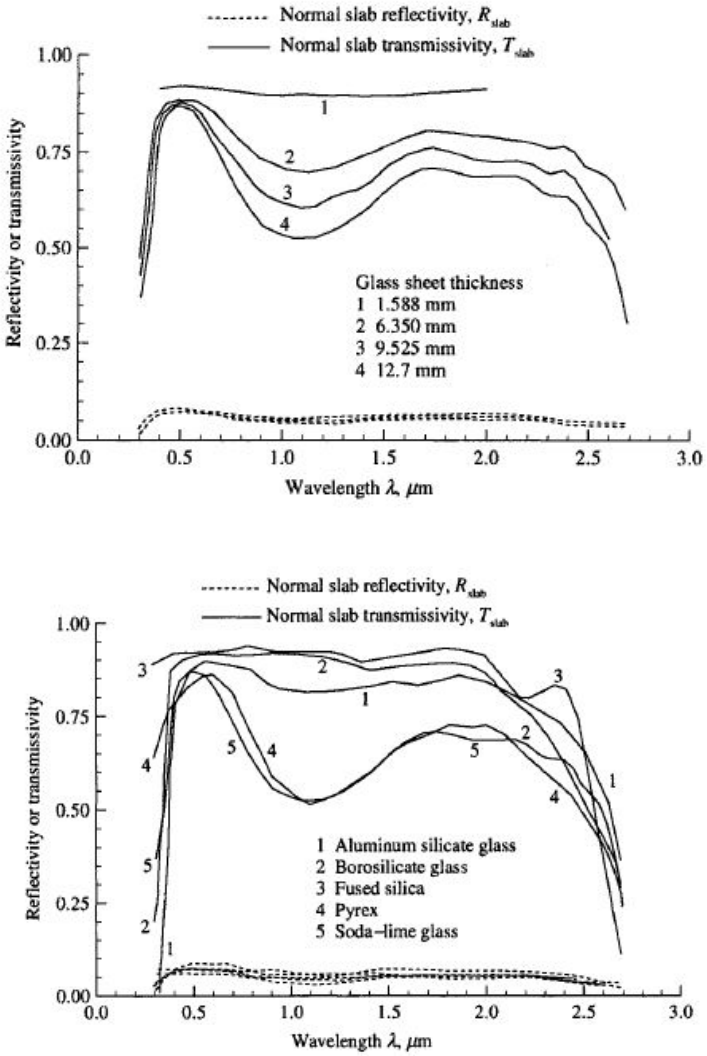

Fig. 29 Wavelenght dependence of reflectivity and trasmissivity coefficients for most common glasses at room temperature [8]

Dependence on angle of incidence. Other considerations have been done for a comprehensive analysis; particularly, the dependence on incident angle has to be taken into account. Indeed, the refraction angle is influenced by the characteristics of the two media (refractive index n) and by the angle of incidence. Hence according to Snell´s law and

Fresnel´s relations, the transmitted energy, due only to the reflection phenomena, is finally found out by means of:

- $\tau_r = \frac{1}{2}\left(\tau_{per} + \tau_{par}\right) = \frac{1}{2}\left[\frac{1-r_{par}}{1+r_{par}} + \frac{1-r_{per}}{1+r_{per}}\right]$, for single slab

- $\tau_r = \frac{1}{2}\left(\tau_{per} + \tau_{par}\right) = \frac{1}{2}\left[\frac{1-r_{par}}{1+(2N-1)\,r_{par}} + \frac{1-r_{per}}{1+(2N-1)\,r_{per}}\right]$, for N slabs.

where r_{par} and r_{per} are respectively the parallel and the perpendicular component of the unpolirised radiation depending by Fresnel Law on the incident and refractive angle (q1,q2, related each other by Snell's Law), see **tab. 8**.

tab. 8 Physics: general laws

Kirchoff´s law

If two enclosures are considered with perfect black wall, containing one a perfect black-body and the other a gray object, after such a period both the enclosures and the objects within them will be at same uniform temperature in accordance with the Secondo Law of Thermodynamics.

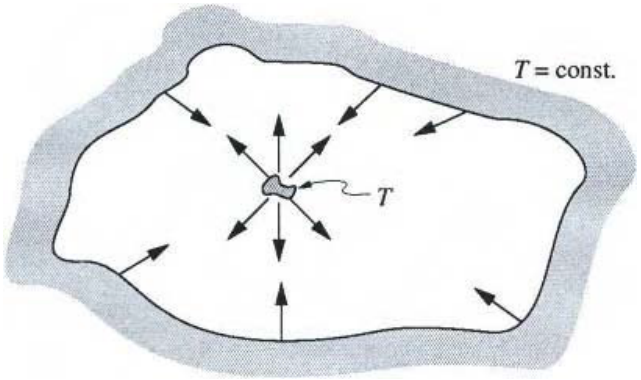

This means that when thermal equilibrium is achieved the wall as well the object will emit as much energy as they absorb. It follows:

directional spectral	$\alpha'_\lambda(T,\lambda,s) = \varepsilon'_\lambda(T,\lambda,s)$	
directional total	$\alpha'(T,s) = \varepsilon'(T,s)$	if the incident radiation has a distribution proportional of that of black body;
hemispherical spectral	$\alpha(\lambda,T) = \varepsilon(\lambda,T)$,	if radiation do not depend on angles;
hemispherical total	$\alpha(T) = \varepsilon(T)$,	if incident radiation do not depend on angle and have a spectral distribution proportional to that of black body

Snell´s law

Considering a boundary between two non-absorbing media, in this case planes with constant amplitude and phase coincide and it is referred to as wave front. When the latter crosses the boundary between the two media, its speed decreases due to the different refraction indexes, so that the initial speed recorded in the first medium $c_1 = c_0/n_1$ becomes $c_2 = c_0/n_2$ in the second media (where c_0 is the speed of light and $n_1 > n_2$).

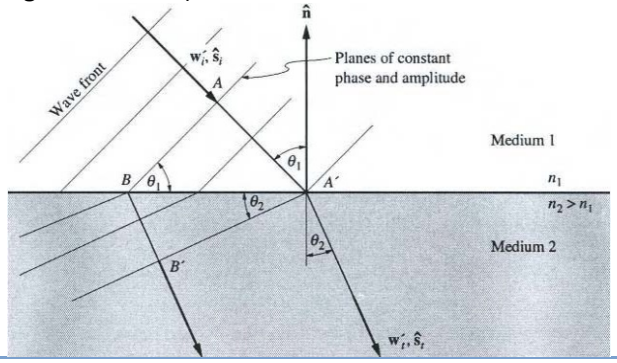

This lead to a legging so that in a Δt time the plane wave front in A reaches A´ while in the same lapse the B plane has encounter a shorter path; this is expressed in geometrical form: Δt = AA`/ $c_1$= BB`/ c_2 moreover considering geometrical relations and the phase velocity:

$$\Delta T = \frac{BA' \sin\theta_i}{c_0/n_1} = \frac{BA' \sin\theta_2}{c_0/n_2} = \frac{BA' \sin\theta_r}{c_0/n_1}$$

where i stays for incident and r for reflected. It means:

1. **the angle of incidence is equal of that of reflection**
2. **while the angle of refraction is proportional to n_1 and n_2**

$$\frac{\sin\theta_2}{\sin\theta_1} = \frac{n_1}{n_2}$$

Beer´s law *(or Beer-Bouger-Lambert´s law for absorption)*
It states that absorption in a media is proportional to of the incident energy at a certain wavelength and direction as well as to the distance the beam travels through the medium, then integrating over a past from 0 (incident surface) to a point a at certain distance:

$$dI_{abs,\lambda} = -k_\lambda I_\lambda ds$$

$$\ln(I_{(s)}) - \ln(I_{(0)}) = -k\,s$$

$$\alpha = \frac{I_{(0)} - I_{(s)}}{I_{(0)}} = 1 - \frac{I_{(s)}}{I_{(0)}} = 1 - \tau_\alpha = 1 - e^{-kL\cos\vartheta_2}$$

where $\mathbf{I}_{abs}$ is the absorbed quantity, $\mathbf{I}(0)$ is the in-coming radiation, $\mathbf{I}(s)$ is the out-coming radiation after absorption takes place, $\tau\alpha$ is the transmitted energy in function of absorption phenomenon, L $\cos(\theta_2)$=s is the distance the radiant flux undergoes in the media with respect to incident angle and *k* is the absorption coefficient.
ps. Generalizing, when scattering has to be taken into account, the extinction coefficient β could be introduced instead of the absorption coefficient *k*.

Fresnel´s relation
Fresnel equations describe light behavior when radiation passes from a medium (with a refractive index n_1) to another (with refractive index n_2) in function of the incident angle (θ_1) and the refractive angle (θ_2). In this case the total reflectivity could be defined as the average value between the parallel (r_{par}) and the perpendicular components (r_{per}).

$$\rho_{per} = \frac{sin^2(\theta_2 - \theta_1)}{sin^2(\theta_2 + \theta_1)}$$

$$\rho_{par} = \frac{sin^2(\theta_2 - \theta_1)}{sin^2(\theta_2 + \theta_1)}$$

Thermal Radiation balance for grey surface

The radiation heat transfer, instead of the convection/conduction mechanisms, does not require any medium to occur. So that looking at the characteristically dimensions of the three phenomena an important difference has to be noticed. Conduction, as well convection, are short-range phenomena, the free mean path for collision between the

molecules in the medium sets at $1O^{-10}$ m, so it is possible to sort infinite volume element whose dimensions are enough large in comparison with the collision path but enough small in comparison with the overall dimension of the analysed system. Instead, in the radiative heat exchanges, a photon or a wave could travel $1O^{-10}$ m without interacting with the surrounding as well as $1O^{+10}$ m. Calculation has to count on the entire volume under consideration and this leads to an integral equation in up to seven independent variables (the frequency of radiation, three space coordinates, two coordinates describing the direction of travel of photons, and time). Moreover, conduction and convection heat transfer rates are linearly proportional to temperature differences while the radiative heat transfer rates are proportional to differences in temperature to the fourth power. Thermal radiation may be defined to be those electromagnetic waves which are emitted by a medium due solely to its temperature, this definition limits the range of wavelengths of importance for heat transfer considerations to between 100 nm (ultraviolet) and 2500 nm (midi-infrared).

Hence some differences could be outlined between the radiative energy balance and the convective/conductive one. Even if in both cases the First Law of thermodynamics is applied, radiative exchange involves properties that are not only depending on matter but also in direction as well as on wavelength, moreover the basic variable appearing in the law of conservation of radiative energy, commonly referred to as the equation of radiative transport, is not temperature but radiative intensity, which is a function not only of location in space (as temperature is), but also of direction, ***Fig. 30***. Hence only after the intensity field is known the local temperature (as well as radiative heat flux vector) could be calculated.

For thermal radiation calculation enclosure bounded by opaque wall (some of which may be artificial to account for radiation penetrating through openings) has to be introduced distinguishing enclosure filled by non-absorbing and non-scattering medium where only *surface radiation transport* occurs and enclosure filled by absorbing gases or semi-transparent media or scattering/absorbing particles where *radiative transport in participating media* follows, accompanied by surface radiative transport. Anyway, in solar thermal system, the three mechanisms of heat transfer strictly interact each other; therefore changing radiative heat flux disturbs the overall energy balance at the surface, causing a change in temperature, as well as conductive-convective fluxes do, and vice versa.

Regarding radiative balance it is necessary to introduce the physical quantities and definitions involved in the phenomena. They are Irradiation (H), Emissive power (E), radiative Intensity (I) and Radiosity (J), **tab. 9**.

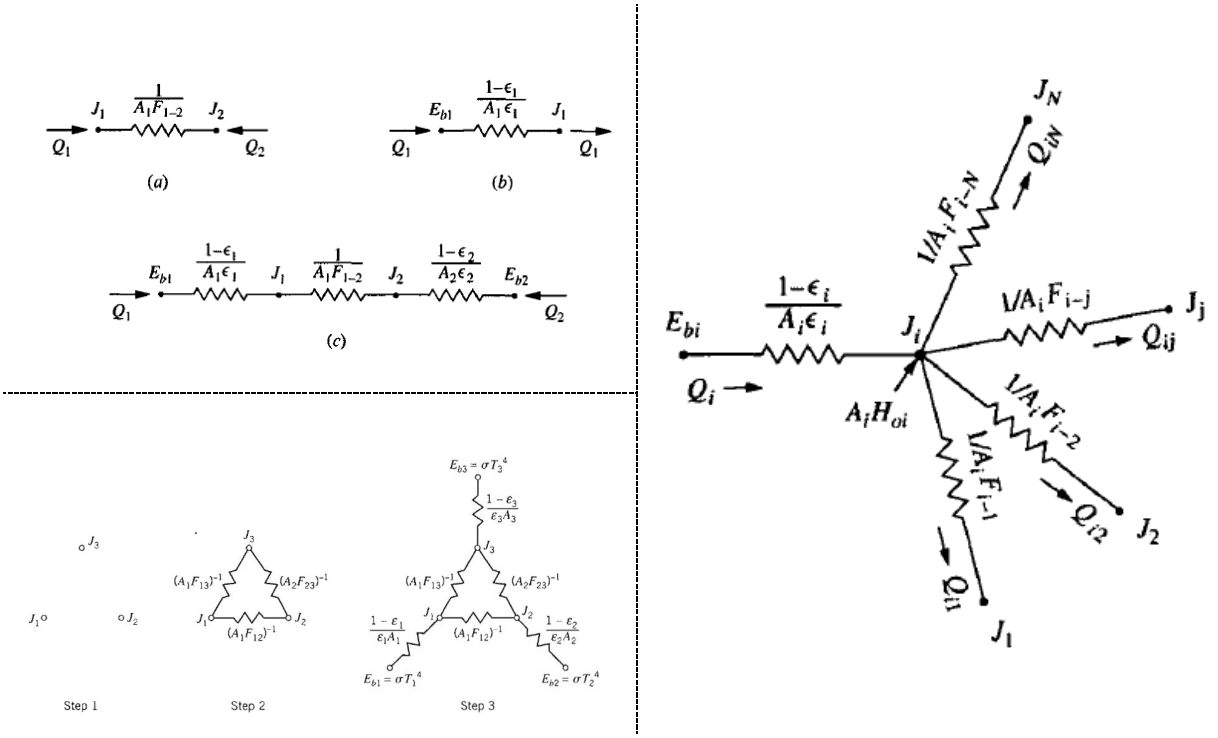

Fig. 30 Electrical analogy for radiative balance in the analysed collector [8].
On the up left, infinity parallel plate are compared in term of space resistance (a), surface resistance(b) and total resistance(c). On the bottom left, electrical analogy for radiative balance in an enclosure in terms of total resistances. On right the network representation for radiative heat flux happening between surface A_i and all other surfaces.

From those definitions and assuming grey surface for which $\rho = 1-\alpha = 1-\varepsilon$, the unitary net flux from a surface at a certain location is the difference between the radiosity (outcoming energy: reflected plus emitted) and the irradiation (oncoming one), where expressing H_i from definitions and grey surface assumption as a function of J and ε [$H_i=(J-\varepsilon E_b)/(1-\varepsilon)$]:

$$q_i/_A = -J_i + H_i = -J_i + \left[\frac{J_i-\varepsilon E_b}{(1-\varepsilon)}\right] \quad \rightarrow \quad q_i = \frac{E_{bi}-J_i}{\left((1-\varepsilon_i)/_{\varepsilon_i A_i}\right)}$$

Moreover if an enclosure is considered, the net flux from a surface has to equal the sum of flux coming from other surfaces (radiosity):

$$\frac{E_{bi} - J_i}{(1-\varepsilon_i)/\varepsilon_i A_i} = \sum_{j=1}^{n} \frac{J_i - J_j}{(A_i F_{ij})^{-1}}$$

In both cases, the ratio $(1-\varepsilon_i)/\varepsilon_i A_i$ could be regard as a resistance between an ideal blackbody emitter and a real one one ($E_{bi}=\sigma T_i^4$) with respect to surface extension A_i; while the product $(A_j F_{ij})^{-1}$ depending only on geometrical aspects is the radiative resistance between surfaces facing each other, see ***Fig. 30***.

tab. 9 Physics: definitions

Irradiation, amount of radiative power reaching a surface per unitary area	**Hλ**	W/m^2
Emissive power, amount of radiative power leaving a surface depending on its local temperature and properties. Henceforward the emitted energy depends on the considered time, surface area and wavelength; total (E) and spectral (Eλ) quantities could be distinguished.	$\boldsymbol{E_\lambda = \int_0^\infty E_\lambda d\lambda => \varepsilon_\lambda \sigma T^4}$	
Radiative intensity, amount of radiative power per unit solid angle and unit area normal to the rays. It is introduced in order to taken into account the directional dependence of the radiation field. Moreover total (I) and spectral (Iλ) quantities could be distinguished.	$\boldsymbol{I_\lambda = \int_0^\infty I_\lambda(r,s) d\lambda}$ Where $\boldsymbol{r}$ is di position vector fixing the location of a point in space, and $\boldsymbol{s}$ is a unit direction vector 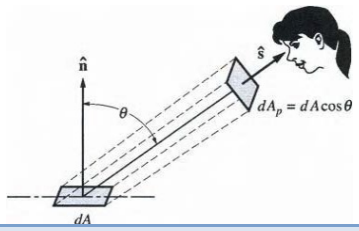	W/m^2
Radiosity, amount of radiative power/energy that is reflected and emitted by a surface	$\boldsymbol{J = \rho H + E}$	W/m^2

Geometry.

Total solid angle above the surface: 2π. It is equal to the surface of a unitary emisphere trough which emitted energy from the surface dA_s penetrates from all directions.

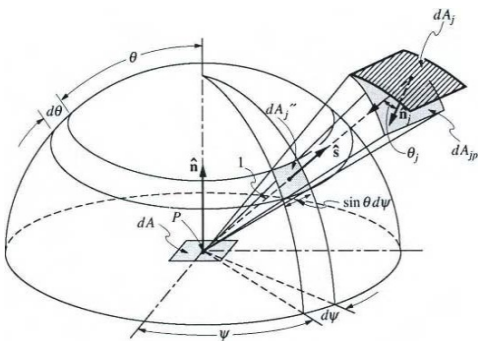

Solid angle:

$$d\Omega = \cos\vartheta_j / S^2 = (1\ x\ \sin\vartheta\ d\psi)\ (1\ d\vartheta)\ .$$

It is the angle with which an infinitesimal surface dAj is seen from a point P, if the angle is projected onto the unit hemisphere above the point, the solid angle is equal to the projected area itself or simply it is an infinitesimal area on a unit sphere

View factor is the ratio between the energy leaving a surface and directly intercept by another surface (without undergoing any reflection) and the total energy leaving the surface itself. It mainly depend on reciprocal position of the two analyzed surfaces:

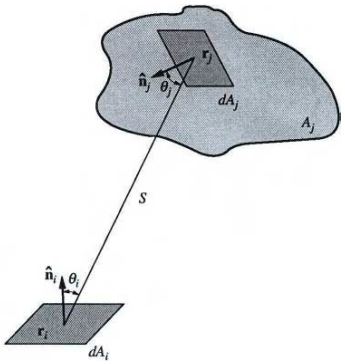

$$dF_{dA_i - dA_j} = \frac{\cos\theta_i \cos\theta_j}{\pi S^2}\, dA_j$$

$$dA_i dF_{dA_i - dA_j} = dF_{dA_j - dA_i}\, dA_j$$

3.2 Thermal Radiation balance for the analysed system

At that point, the radiative balances for the analysed prototype are presented and assumed as start-point for the FEM simulation models, see ***Fig. 31***. A first hypothesis induces to split the system into two sub-system sorting two main bands in order to consider the analysed surface as grey diffuse ones with respect to wavelength. Split point occurs at λ=2500nm corresponding from one hand to the main band wherein solar radiation is distributed and from the other hand to the break point at which glass properties changes.

Starting from this assumption band B1 and band B2 are chosen, it is interesting to notice how glass is almost transparent in the first band while it is opaque in the second chosen one, see ***Fig. 31***. Then in band 1, absorber plate interacts mainly with the solar source and the surrounding surfaces that are approximate as a parallel plane reflecting the solar rays themselves ($H_{sun,diff}$). As this plane is assumed at an infinite distance, as well as solar source is, resistance between node J_{B1} and $J_{surroundings,B1}$ is actually zero; moreover focusing on band 1 and on wavelength energy distribution curves it follows: $J_{B1}=\rho H_{sun,beam}+\rho H_{sun,diff}$ while the

emission from surface are out of interest in the analysed range. Indeed, for the sake of accuracy, only the transmitted energy by glass is supposed to reach the absorber plate.

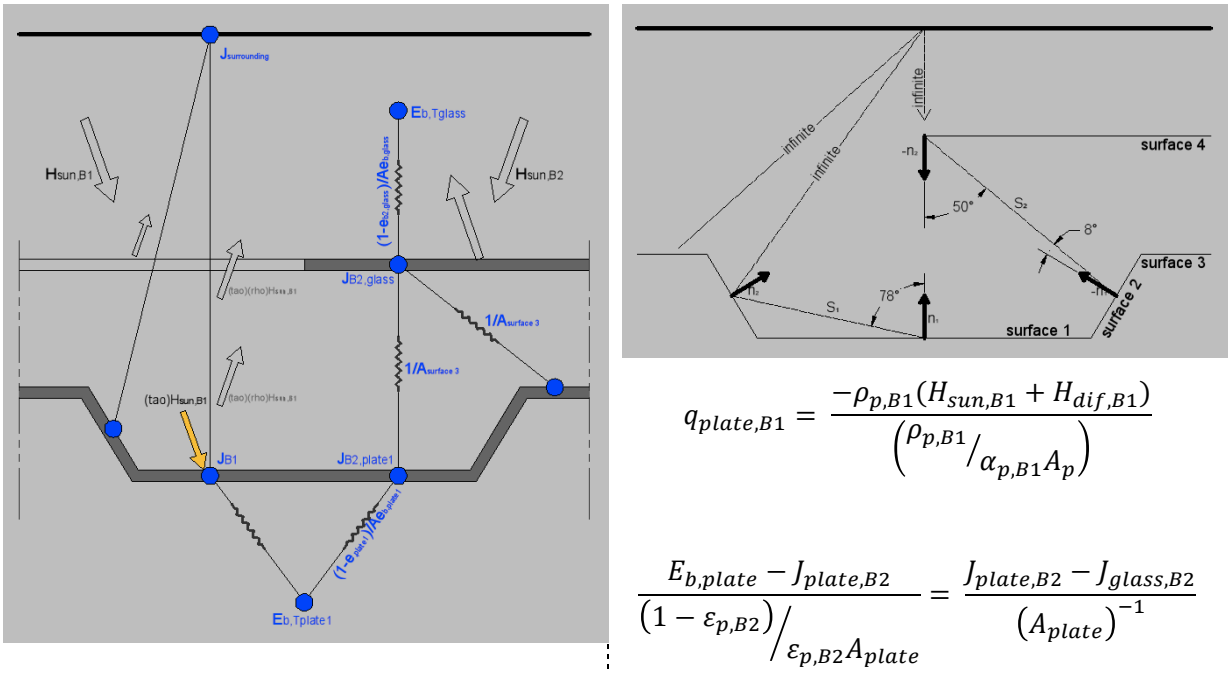

$$q_{plate,B1} = \frac{-\rho_{p,B1}(H_{sun,B1} + H_{dif,B1})}{\left(\rho_{p,B1}/\alpha_{p,B1}A_p\right)}$$

$$\frac{E_{b,plate} - J_{plate,B2}}{(1-\varepsilon_{p,B2})/\varepsilon_{p,B2}A_{plate}} = \frac{J_{plate,B2} - J_{glass,B2}}{(A_{plate})^{-1}}$$

Fig. 31 Electrical analogy for radiative exchange between surfaces in Prototype A, on the left the comprehensive scheme is shown while on the right the simplified one is presented.

Moreover, considering the characteristic dimensions of corrugations and the reciprocal distance between surfaces some other notices regarding resistances in the B2 follows. Specifically view factor between surface 2 and 4 and between surface 2 and 1 tends to zero in both cases inducing at an infinite resistance. For that reason system is finally simplified as shown in ***Fig. 32*** for both prototype A and B, and only resistance due to surface area considered between surfaces while resistance due to radiative properties are included between the corresponding black body nodes and the J-nodes. These mechanisms will be coupled to conductive/convective phenomena in FEM simulation models.

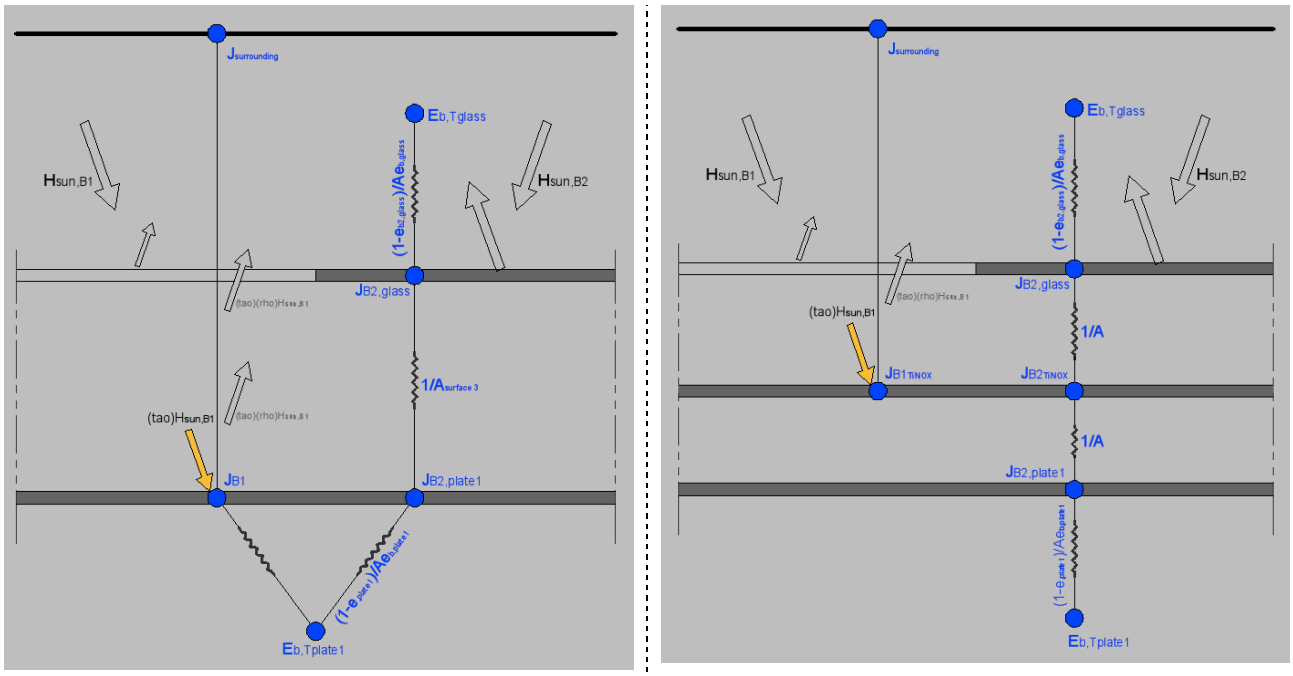

Fig. 32 Electrical analogy for radiative exchange between surfaces in Prototype A (left) and B (right) in the simplified system.

3.3 Collector balance and parameters

In steady state conditions, the overall energy balance for a plate collector leads to define the useful energy from the collector as the difference between the absorbed solar radiation and the thermal losses:

$$Q_u = Ac\ [I_{sun,ab} - U_L(T_p - T_{amb})\ ]$$

where $I_{sun,ab}$ is the absorbed solar radiation by the absorber plate considering the optical losses through cover while U_L is the overall heat loss coefficient, see tab. 10. Specifically the generic incoming radiation group beam, diffuse and ground reflected component $I_{sun}= I_{sun,b}+ I_{sun,d} + I_{sun,gr}$.

tab. 10 Collector characteristic parameter: formula and definition

OVERALL HEAT LOSS COEFFICIENT

It refers to bottom, top and edge heat losses. Specifically, top losses (U_t) depends on radiative and convective phenomena happening between plate/cover and cover/out-boundary; while bottom losses (U_b) regards conductions through the insulation layer and convection/radiation between bottom surface and external ambient. Finally, edge losses (U_e) concerns losses estimated by assuming one-dimensional heat flow refereed to collector area (A_C). Electrical analogy for a double glazed system from **[3]** is proposed on the left, following:

$$U_L = U_b + U_t + U_e = \frac{1}{R_4 + R_5} + \frac{1}{R_1 + R_2 + R_3} + \frac{(UA)_e}{A_c}$$

$R_{1,5} = \left(h_{c,wind} + h_{r,amb}\right)^{-1}$ accounting on up (R_1) and down (R_2) boundary convective/radiative exchange at the appropriate ambient temperature;

$R_{3,2} = \left(h_{c,s1/s2} + h_{r,s1/s2}\right)^{-1}$ accounting on convective exchange between parallel plates in the collectors (cover/cover), (cover/plate)

$R_4 = \sum(s/k)^{-1}$ accounting on conductive resistance by the back insulation layers

ps. For Radiative/Convective heat transfer coefficients assessment see tab. 11.

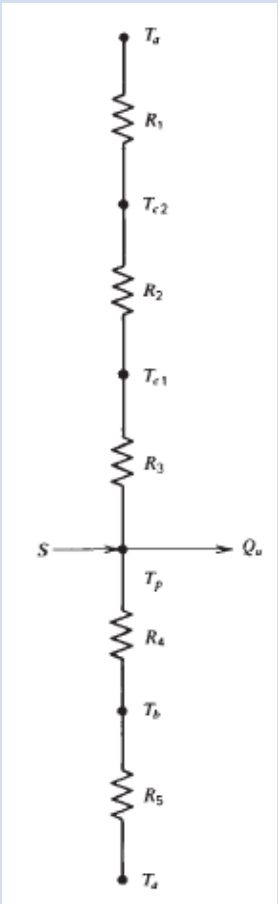

EFFICIENCY FACTOR

It is defined as the ratio between the resistance from the fluid to the ambient temperature and resistance occurring between the absorber plate and the ambient temperature: $F' = U_0/U_L$.

$$F' = \frac{1/U_L}{W\left[\frac{1}{U_L(D+(W-D)F)} + \frac{1}{C_b} + \frac{1}{\pi D h_{fl}}\right]}$$

where D and W are geometrical features whose meaning is shown in the figure below, F is the fin factor, C_b the bond conductance and h_{fl} the fluid heat transfer coefficient.

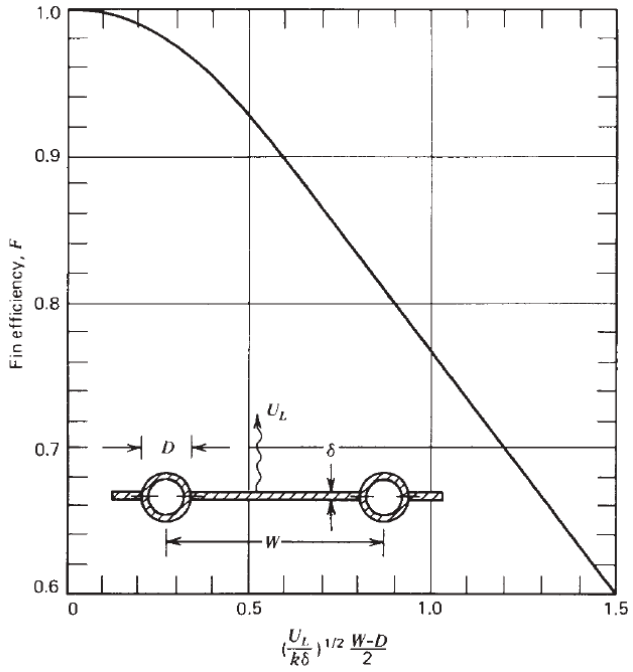

fin efficiency for tube-and-sheet solar collector

HEAT REMOVAL FACTOR

This parameters depending on mass flow rate, relates the actual useful energy gain evaluated in terms of inlet/outlet temperature to the maximum useful energy gain obtainable if collector surfaces were at the inlet fluid temperature (T_p=T_{in}) that means energy losses are minimum:

$$F_R = \frac{\dot{m}\, c_p\,(T_{out} - T_{in})}{Ac\,[I_{sun,ab} - U_L(T_{in} - T_{amb})\,]} = \frac{\dot{m}\, c_p}{AcU_L}\left(1 - \frac{I_{sun,ab}/U_L - (T_{out} - T_{amb})}{I_{sun,ab}/U_L - (T_{in} - T_{amb})}\right)$$

$$F_R = \frac{\dot{m}\, c_p}{AcU_L}\left(1 - e^{-\frac{AcU_L F'}{\dot{m}\, c_p}}\right)$$

FLOW FACTOR

$$F'' = \frac{F_R}{F'} = \frac{\dot{m}\, c_p}{AcU_L F'}\left(1 - e^{-\frac{AcU_L F'}{\dot{m}\, c_p}}\right)$$

($\tau\alpha$) PRODUCT

It is a coefficient proportional to the glass transmittance coefficient and the plate absorptance coefficient, introduced for accounting on multiple reflection occurring between cover surface and absorber plate.

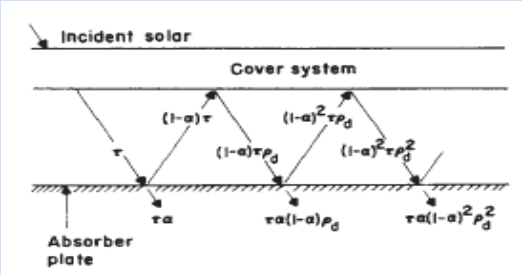

$$(\tau\alpha) = \frac{\tau\,\alpha}{1-(1-\alpha)\rho_d}$$

$$\rho_d = \tau_a(1-\tau_r) = \tau_a - \tau$$

As obviously, trasmissivity coefficient refers to cover as well as ρ_d while absorptivity refers to the plate and depend on the transmitted energy according to absorption phenomena (t_a) and the overall transmitted energy (t).

TIME CONSTANT

It is the time required by a specific solar collector for changing about a quantity equal to (1 - 1/e) from the initial to the ultimate steady value after a step change in incident radiation or inlet fluid temperature is done:

$$\frac{T_{out,t} - T_{initial}}{T_{out,t0} - T_{initial}} = \frac{1}{e}$$

where t stays for time and t_0 for the time when the step change occurs.

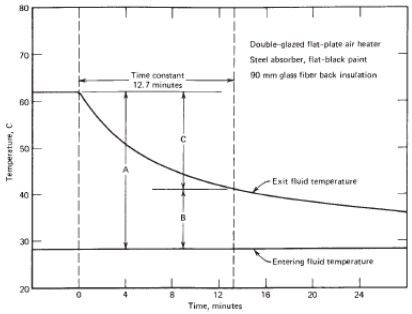

Moreover, introducing the heat removal factor F_R as defined in tab. 10, the useful energy gain could be expressed proportionally to the maximum possible production evaluated when the heat losses are reduced at minimum value (T_p=T_{in}). Then, considering optical losses and expressing Qu in terms of ambient and inlet temperature by means of F_R, the critical radiation level could be identify as such a radiation quantity beneath which energy absorbed is less than losses so heat production is actually nullified:

$$Q_u = Ac\,F_R[(\tau\alpha)I_{sun} - U_L(T_i - T_{amb})] \rightarrow \quad I_{sun,cr} = \frac{F_R U_L(T_i - T_{amb})}{F_R(\tau\alpha)}$$

Consequently, collector instantaneous efficiency being the ratio between the useful energy and the incident solar radiation is:

$$\eta = \frac{Q_u}{A_c I_{sun}} = \frac{mc_p(T_{out} - T_{in})}{I_{sun}A} = F_R(\tau\alpha) - \frac{F_R U_L(T_{in} - T_{amb})}{I_{sun}}$$

It represents a straight line where the angular coefficient represent heat losses in function of ΔT while the known term represent the maximum efficiency achievable when losses are null (η_0, zero-loss collector efficiency). It is worth to notice that it possible to introduce a linear dependence of U_L with temperature, in this case efficiency curve is a quadratic one in the form: $y = \eta_0 + b_1 x + b_2 x^2$ where x is the temperature difference while b_1 is the heat loss coefficient and b_2 the efficiency coefficient. The steady-state efficiency curve is basically a start point for the present work analysis and belongs to standard test that will be described in next paragraph as well as other consideration directly dealing with present analysis.

Moreover, effects of incident angle on the useful irradiation entering the system could be introduced by means of the **Incident Angle Modifier** (IAM) on ($\tau\alpha$) product. It varies from a collector to another and allows to use the ($\tau\alpha$) value at normal incidence introducing in previous equation K($\tau\alpha$) estimated by experimental tests or by means of the following correlation by Souka and Safwat **[3**] suitable in case of flat cover:

$$K_{\tau\alpha} = 1 - b_0 \left(\frac{1}{\cos\theta} - 1 \right)$$

where θ is the incident angle and b_0 the IAM coefficient, b_0=0.136 could be use for typical single cover. Generally this value varies linearly for θ<60 and it is used also for evaluate the diffuse and ground-reflected fractions of the incoming solar energy evaluated on a general tilted surface at the appropriate angle of incidence:

$$I_{sun} = I_{sun,b} R_b K_{\tau\alpha,b} (\tau\alpha)_n + I_{sun,d} K_{\tau\alpha,d} (\tau\alpha)_n \left(\frac{1 + \cos\beta}{2} \right) + \rho_g I_{sun} K_{\tau\alpha,g} (\tau\alpha)_n \left(\frac{1 - \cos\beta}{2} \right)$$

where R_b represent the ratio between beam radiation on a tilted plane to that on horizontal surface and β is the tilted angle of the surface itself.

3.4 Collector transient behaviour

Actually the steady state assumption driving all previous reasoning actually does not fit with real operating conditions that are characterised by intermittent behaviour of the driving force, such as sun and wind. Response of the collector to such change in ambient conditions deals then with its **heat capacity (Cc).** A transient energy balances (at plate and cover, for example) are then necessary for solving correctly the system and most of solutions needs an iterative process. For determining the effective heat capacity of a collector $\mathbf{(Cc)_e}$, European standard UNI EN 12975-2:2006 **[19**] suggest for water circulating component to manage indoor tests in which fluid moves from the top to the bottom and inlet temperature is assumed constant until steady-state conditions are reached. After, inlet temperature is raised rapidly by about 10K and measurements made until steady-state conditions are reached again; then the effective heat capacity is:

$$Cc\frac{dT_m}{dt} = -mc_f(T_{out} - T_{in}) - AU(T_m - T_{amb})$$

where T_m is the reduced temperature evaluated as the sum of the inlet temperature and half of the inlet/outlet temperature difference where T_{in} and T_{out} are evaluated according to flow direction. Integrating the formula from time 1 corresponding to first steady state condition to time 2 corresponding to the achieved new thermal equilibrium condition, the heat capacity is then the quantity of energy in terms of heat transfer through the mass flowrate and heat losses need for change the fluid temperature from state 1 to state 2. Anyway, it is possible to calculate this value considering all *i*-elements composing of the collector as:

$$Cc_e = \sum_i^n p_i m_i c_i$$

where m stays for mass (kg), c for the specific heat (J/kg) and p is a weighting factor for accounting on the fact that not all elements in the collector participate in the same way to its thermal inertia.

For describing in deep thermal behaviour of solar collector under variable ambient condition, a quasi-dynamic model based on the steady-state one is introduced for taken into

consideration the dependence of results on direct and diffuse radiation, wind speed, sky temperature, incidence angle effects and effective thermal capacitance:

$$\frac{Q}{A} = \left[F'(\tau\alpha)_e K_{\theta,b}(\theta) I_{sun,b} + F'(\tau\alpha)_e K_{\theta,d}(\theta) I_{sun,d}\right] - c_1(T_m - T_{amb}) - c_2(T_m - T_{amb})^2 - c_3 v_{wind}(T_m - T_{amb})^2 + c_4\left(E_L - \sigma {T_{amb}}^4\right) + c_5\, dT_m/dt - c_6 v_{wind} I^*$$

where each coefficient c are introduced for considering ambient influence on solar collector performance at different level, v_{wind} is the ambeint air speed, E_L is the longwave irradiance and I* is the global hemispherical solar irradiance. Looking at formula first line is exactly the model for steady state conditions in which diffuse (d-subscript) and beam (b-subscript) irradiation are distinguished and related to the correspondant ($\tau\alpha$) value for detailing interaction with the sun source; and the heat loss coefficient is dependant on temperature. While second line express in deep all other influences from convective losses at boundary system due to wind action, radiative exchange with the out-boundary ambient and transient response in function of heat capacity. Specifically c-coefficients are :

c_1	heat loss coefficient at (Tm-Tamb)=0	$Wm^{-2}K^{-1}$
c_2	temperature dependance of the heat loss coefficient	$Wm^{-2}K^{-1}$
c_3	wind speed dependance of the heat loss coefficient	$Jm^{-3}K^{-2}$
c_4	sky temperature dependance of the heat loss coefficient	$Wm^{-2}K^{-1}$
c_5	effective thermal capacity	$Jm^{-2}K^{-2}$
c_6	wind dependance on the zero loss coefficient	sm^{-1}

tab. 11 convective and radiative heat transfer coefficient

Radiative coefficient

In order to enhance comparison between the heat transfer mechanisms, radiative coefficient is introduced considering the radiative flux between two surfaces at different temperature: $Q=\varepsilon\sigma(T_2^4-T_1^4)A$ and the radiative resistances $((1-\varepsilon_i)/\varepsilon_i A_i;\ A_j F_{ij})^{-1}$. The aim is expressing this flux as: $Q= hr\ \Delta T\ A$, so that the radiative heat flux could be evaluated as a product between a temperature difference and a coefficient as well as conductive/convective problems.

$$h_r = \frac{\sigma\left(T_1^{\,2}+T_2^{\,2}\right)(T_2-T_1)}{(1-\varepsilon_1)/\varepsilon_1+F_{12}+(1-\varepsilon_2)A_1/(\varepsilon_2 A_2)} \qquad (\text{W m}^{-2}\,\text{K}^{-1})$$

This coefficient takes a simplified form if surfaces with equal area and reciprocal almost-unitary view factor are considered, as in most common problem in solar collector design. Then, considering the plate and glass temperatures (respectively T_p and T_c) and introducing the equality $A_1=A_2$ while F_{12} is closed to unity; it follows:

$$h_{r,p-g} = \frac{\sigma\left(T_p^{\,2}+T_g^{\,2}\right)(T_p-T_g)}{\left(\varepsilon_p^{-1}\right)+\left(\varepsilon_g^{-1}\right)-1} \qquad (\text{W m}^{-2}\,\text{K}^{-1})$$

If the radiative exchange between the glass and the ambient is considered some other simplifications could be introduced and the coefficient becomes:

$$h_{r,g-sky} = \varepsilon_g\,\sigma\left(T_g^{\,3}+T_{sky}^{\,3}\right)\left(T_g+T_{sky}\right) \qquad (\text{W m}^{-2}\,\text{K}^{-1})$$

where the sky temperature is a function of the air temperature (T_a), the dew point temperature (T_{dp}) and time t:

$$T_{sky} = T_a*(0{,}711+ 0{,}0056\ T_{dp} + 0{,}000073\ T_{dp}^{\,2} + 0{,}013\ \cos(15t).$$

Convective coefficient

Convective coefficients could be assessed by means of validated correlations between Reyleigh, Nusselt, Prandtl, Reynolds and Grashof numbers. From Nusselt number definition the convective coefficient is then evaluated by means of:

$$h_c = \frac{Nu\ k}{L}\ (\text{Wm}^{-2}\text{K}^{-1})$$

Two main groups of correlation could be distinguished:

- Correlation for natural flow
- Correlation for forced flow

Nusselt num.: $Nu = \frac{hL}{k}$

Rayleigh num.: $Ra = \frac{g\beta' \Delta T\ L^3}{\nu\alpha}$

Prandtl num.: $Pr = \frac{\nu}{\alpha}$

Reinolds num.: $Re = \frac{\rho\ V\ L}{\mu} = \frac{V\ L}{\nu}$

Grashof num.: $Gr = \frac{g\beta' \Delta T\ L^3}{\nu^2}$

where: h= heat transfer coefficient [W/m2 K]; L= plate spacing [m]; k = thermal conductivity [W/m K]; g = gravitational constant [m/s2]; β´=volumetric coefficient of expansion (for an ideal gas, β´= 1/T) [1/K]; T = temperature difference between plates [K]; ν = kinematic viscosity [m2/s]; α = thermal diffusivity [m2/s]; V= fluid speed (m/s); rho= density… D_H = Perimeter/Area ; m = dynamic viscosity

3.5 Steady-state efficiency curve evaluation by standard regulations and FEM-simulation

The efficiency curve, the thermal capacity and the time constant are generally used for characterising solar collector being suitable in describing its thermal behaviour and time response. For that purpose, standard regulations that have been introduced at local level and more, prescribes test procedures and method for sorting and processing data in order to obtain these parameters. Present work refers to the European Standard EN 12975-2:2006 **[19**] for liquid heater collector and to the Italian standard UNI 8937/1987 **[21**] for flat air collector. Both rules describe the main ambient conditions that are suitable for sorting useful data in outside operating conditions (see tab. 12) and the way this data has to be used for assessing the collector characteristics.

tab. 12 standard regulation test requirements and simulation inputs

data/input		UNI 8937/1987	EN 12975-2:2006	Simulation
v_{wind}	[m s^{-1}]	< 5	3 ± 1	2.5
I_{sun}	[W m^{-2}]	> 600	> 700	>600
albedo	[-]	0,2	isotropically assumption	-
α	[°]	0°< α < 40°	<20°	0°
azimuth	[°]	0°	0°	unimportant(1)
slope	[°]	$45° \pm 5$	$IAM = IAM_n \pm 2\%$	unimportant(1)
m	[m^3 $s^{-1}m^{-2}$]	0.01 – 0.03	0.02	0.01, 0.03, 0.05(2)
T_{amb}	[°C]	5 < T_{amb} < 35	-	5 < T_{amb} < 35
$T_{amb,rad}$	[°C]	-	$T_{amb} \cong T_{amb,rad}$	$T_{amb} = T_{amb,rad}$
T_{in}	[°C]	variable(3)	$T_{in} = \pm 3 + T_{amb}$	variable
$(T_{out}.T_{in})_{min}$	[°C]	5	-	5

(1) Irradiation on the collector plane is mainly modelled giving the direction of solar rays that are considered perpendicular with respect to the collector plane.

(2) The 0.05 Kg s^{-1} value belongs to the available recorded data and validation/calibration procedure.

(3) Italian rule introduces a minimum inlet temperature value $\boldsymbol{T_{in,min} = T_{amb} \pm 5°C}$ this restriction allows to maximise the resolution for the intercepting term.

Specifically the European standard distinguishes between outdoor tests and tests in solar irradiance simulator making differences between steady-state performance test and quasi-dynamic test conditions; moreover this regulation deals with capacity and time constant evaluations. Anyway European code is specifically calibrate for liquid heater meanwhile, the Italian standard focuses on air heater efficiency curve assessment. Both regulations put attention on surroundings; specifically reflections and obstructions by other surfaces as to be avoided as well as thermal bridge between the collector itself and the mounting system. Moreover air should circulate freely around the front and the back of the collector and a minimum distance from the ground (0,5m) in Italian regulation is introduced. More specifications belong to the European standard that introduces the concept of integrated solar collector specifying a minimum distance from the roof-edge for the collector that should be mounted in a roof and discharging wind effect on back for such an integrated collector. Other prescriptions regard the accuracy of the sensors and the way they have to be mounted in order to reduce error and uncertainties due to the surroundings.

In this regards, both regulations tend to reduce variability in measurements due to the influence of external environment with the main purpose of obtaining consistent set of data. Finally, both regulations introduce the concept of test period in which stable environment has to be provided and thermal equilibrium of collector achieved. It concerns permitted deviation from mean value during measurement as reported and compared in tab. 13.

tab. 13 Permitted standard deviation in measurements

parameter	UNI 8937/1987	EN 12975-2:2006
global solar irradiance	$\pm 50\ Wm^{-2}$	$\pm 50\ Wm^{-2}$
indoor surrounding temperature	$\pm 1.0\ K$	$\pm 1.0\ K$
outdoor surrounding temperature	$\pm 1.5\ K$	$\pm 1.0\ K$
fluid temperature	$\pm 0.1\ K$	-
mass flow rate	$\pm 1\%$	-

These regulations are basically the keystone for the present work. It is worth to notice that some prescriptions, valid for test procedures, has to be reorganised for the successively FEM model assuming a proper meaning related to the calculation method; moreover other adaptations have been introduced for the evaluation of the integrated collector.

Indeed, FEM calculations overpasses problems related to accuracy in measuring data and to provide stable input (constant irradiation, ambient and inlet temperature, inlet mass flow,…). Only outlet temperature depends on the way data are sorted from simulation since the temperature field in the domain is provided mesh-node by mesh-node; in this case the accuracy prescribed for measurements is used for evaluate the reliability of T_{out} as it is evaluated from all the available simulation output. Even that, while most of the weather data and working input have to be measured in test procedures and are subjects of standard regulations in order to ensure consistency of tests, in FEM model they are merely inputs. For that reason they are totally stable: the steady state condition is then native in the model. Moreover, FEM modelling goes beyond difficulties related to uncertainties belonging to surroundings influences such as undesirable reflections and shadowing effects. The environmental interactions are actually mathematically defined and controlled by boundary system inputs simulating surroundings.

Results reliability depends then on calibration and validation of the model, in knowing the limit of the model itself, in sorting and processing data and in determining the most appropriate inputs to simulate external ambient and physical exchanges with it. All these points are treated in previous chapter regarding the FEM model.

Efficiency curve is determined by introducing as input the recorded data from the experimental campaign meeting at the same time the standard rule prescriptions as replicated and compared in tab. 12. Efficiency of collector is then evaluated at different standard conditions varying one at time the inlet temperature and irradiation values:

$$\eta = \frac{mc_p(T_{out} - T_{in})}{I_{sun}A}$$

Values are plotted with respect to a normalised ΔT / I_{sun} value. 1st or 2nd order interpolations are allowed by both regulations, specifically and according to the European standard, a

second order fit shall not be used if the value deduced for a_2 is negative. It follows that efficiency curve in both standard rules is expressed as a variable of *x* that depends in turn on temperature field:

$$\eta = \eta_0 - a_1 x - a_2 x^2$$

where the η_0 terms (or intercept term) describes the maximum performance collector could achieve, the a_1 and a_2 terms state for the energy losses. Actually, the useful energy from collector in steady state condition could be written as a function of incoming solar energy minus the overall energy losses, it follows:

$$Q_u = A_c F_R [I_{sun}(\tau\alpha) - U_L(T_{in} - T_{amb})]$$

$$\eta_i = \frac{Q_u}{A_c I_{sun}} = F_R(\tau\alpha) - \frac{F_R U_L (T_{in} - T_{amb})}{I_{sun}}$$

where F_R is the removal factor, U_L the overall loss coefficient. It is common to assume a linear dependence of U_L with temperature, $U_L = a_1 + a_2(T - T_{amb})$ from which belong the 2nd order expression for efficiency. Anyway, this second coefficient is sometimes discharged.

The main difference between the regulations stays in the way ΔT is evaluated by recorded data. As assumed in the generic efficiency equation the most easily deducible is:

$$\Delta T = (T_{in} - T_{amb})$$

Moreover the difference between the arithmetic average of inlet and outlet fluid is sometimes used as well as others assumptions, in order to best solve energy losses evaluations. Present works deals with the previous value as well as the one introduced by European and Italian standards. Specifically, they uses the reduced temperature difference (T_m^*), expressed in funcion of fluid mean temperature (t_m):

$$T_m^* = \frac{(t_m - t_a)}{I_{sun}}$$

$$t_m = t_{in} + \frac{\Delta T}{2} = t_{in} + \frac{T_{out} - T_{in}}{2}$$

$$\Delta T = (T_m^* - T_{amb})$$

Regarding T_{amb} it is necessary to stress attention on the most appropriate value for STC-wall efficiency calculation. Actually, if an integrated solar collector is considered, top and back losses are proportional respectively to the outdoor temperature and to the indoor temperature. For that reason and taking into account that the first are generally predominant, the ambient weighted temperature substitutes the T_{amb}:

$$T_{amb,w} = \frac{T_{outdoor}U_{top} + T_{indoor}U_{back}}{U_{top} + U_{back}}$$

$$U_{top} = \left(\frac{1}{h_{outdoor}} + \frac{s_{glass}}{k_{glass}} + \frac{1}{h_{channel}}\right)^{-1}$$

$$U_{back} = \left(\frac{1}{h_{channel}} + \sum \frac{s_{ST-layer}}{k_{ST-layer}} + \frac{1}{h_{indoor}}\right)^{-1}$$

where $h_{outdoor}$ and h_{indoor} are the coefficient prescribed by UNI EN ISO 6946 and accounts on radiative and convective heat exchange towards the indoor and outdoor ambient. Simulations run then for the validated models corresponding to suitable irradiation values, for each of them three different flow rates are supposed, see tab. 14.

tab. 14 Flow speed according to UNI 8937/1987

specific volumetric flow rate [$m^3\ m^{-2}s^{-1}$]	Prototype A [$m\ s^{-1}$]	Prototype B [$m\ s^{-1}$]
0.05	0.69	1.22
0.03	0.41	0.73
0.01	0.14	0.24

Moreover, simulations run for prototypes and STC-walls introducing the following inlet temperatures:

$$T_{in} = T_{amb}$$

$$T_{in} = T_{amb} \pm 5°C$$

$$T_{in,(n)} = T_{out,(n-1)}$$

where n stays for the number of simulation. First two assumptions allow to best solve the y=1 axis interception, while the simulations at $T_{in,(n)}=T_{out,(n-1)}$ stops when the outlet/inlet temperature difference reaches 5°C, as prescribed by UNI 8937/1987. In this way, all working operating conditions are fulfilled and the sorted efficiency curve appropriately gives back the collector performance. Second order approximation is used where possible as prescribed by EN 12975-2:2006.

4. FEM SIMULATION AND REFERENCE CASES

Present chapter describes software models applied to the reference collectors: prototypes A-B FEM models as well as STC-wall A-B models are presented and correspondent validations proposed for the basic prototypes, outlining the limit of the models themselves. In order to clarify the chapter structure a brief summery is firstly proposed according to main investigated values: T_{out}, T_{node} at prescribed working steady state conditions. Indeed, it is firstly necessary to distinguishing the validation/calibration step from proper simulation phase. Data from experimental campaign are initially used in order to check validity and limit of the system for the prototypes A and B, while during simulation phase main inputs belong to the standard regulations, as exposed in previous chapter.

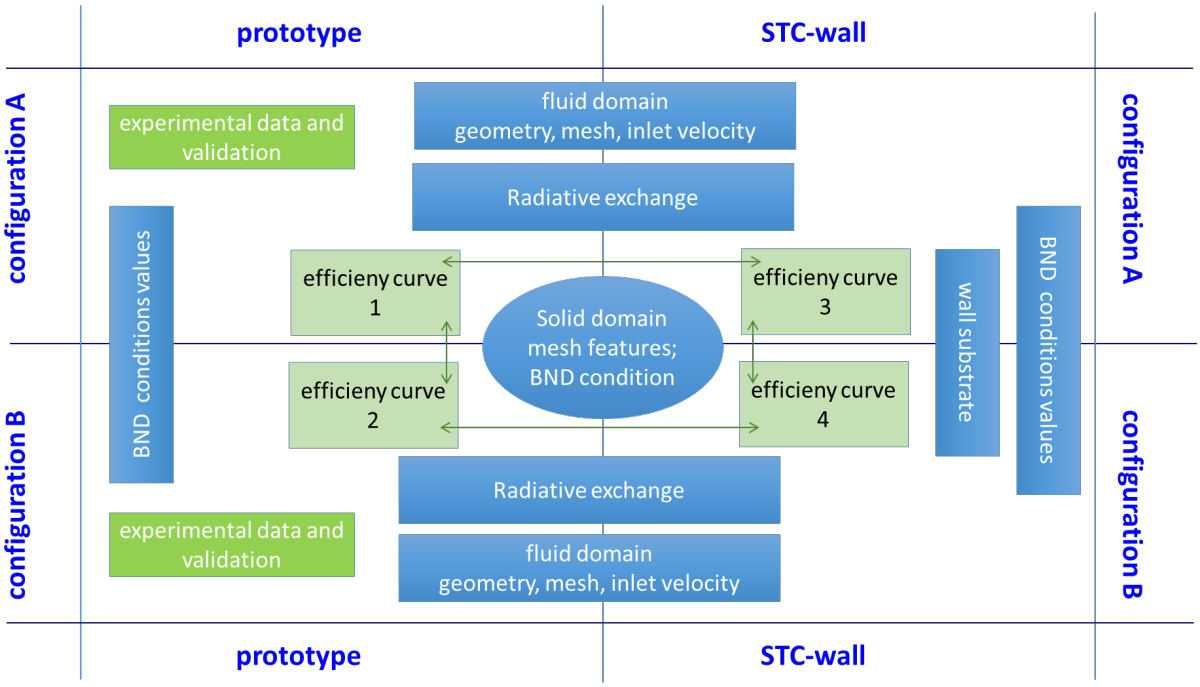

Fig. 33 Analogies and differences among FEM models.

Other transversally differences and similitudes among the four models exist and drive present chapter structure, see ***Fig. 33***:

A. **general model.** Considering boundary conditions are the same for all model varying only their value from prototype to STC-wall one physic general model is identify.

Differences are needed for distinguishing the internal radiative exchange and the relationship with the radiative source from Configuration A and Configuration B.

B. **mesh for solid domain.** All models have same typical dimension for solid elements, distinguishing two different orders of magnitude: insulation and wall layers (the latter only in STC-wall) for one part; glass, plate and TiNOX (the latter only in STC-wall) for the other parts. Consequently mesh is assessed only one time for all models and the verified proportion among minimum and maximum size of elements respect in all models;

C. **mesh for fluid domain.** Channel geometry varies from configuration A to configuration B, hence mesh features must meet different instances.

D. **position of the cut-line at the exit section.** The desired T_{out} value is computed evaluating the temperature field along a cut-line that has to be fit at a suitable distance so that fluid is properly mixed. Considering velocity field varies according to inlet fluid speed three evaluations are for STC-wall and prototype A; while other three regards STC-wall and prototype A.

4.1 FEM models

General model

For simplifying calculations, physics/geometrical symmetries were exploited and mesh design influence on results investigated for first. It is worth to notice that out-boundary system is the same in both models while internal radiative exchanges and fluid field deeply change comparing prototype A and prototype B models.

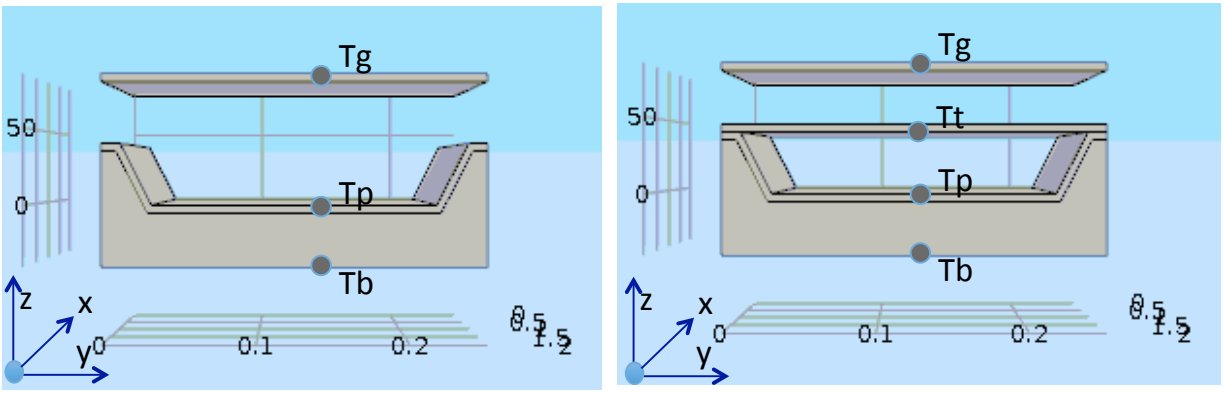

Fig. 34 Comsol© models and investigated values with respect to geometric reference system; on the left prototype A, on the right prototype B.

For all models, according to the purpose of the present study, the physical FEM model is split in three parts:

1. The first model is a 3D one and is suitable for determining intermediate T_g and T_p values to be used as input in the second model;
2. The second model is a 2D one and is suitable for evaluating the outlet temperature of air stream T_{out} according to the previous temperatures and to a specified inlet temperature;
3. The third 3D model is finally suitable for evaluating the temperature field within the STC-wall ($T_{x,y,z}$), sorting the node temperatures.

The three models run serially (***Fig. 35***) returning the radiosity and temperature field (from module 3) and the velocity and temperature field among the fluid stream (from module 2). All results were sorted and processed in order to obtain the investigated values:

$$T_{node} = T_{\left(x=\frac{H}{2},\ y=\frac{p}{2},\ z_i\right)}$$

$$T_{fluid,out} = f\left(T_{x=H,\ y_i,\ z_i}\right)$$

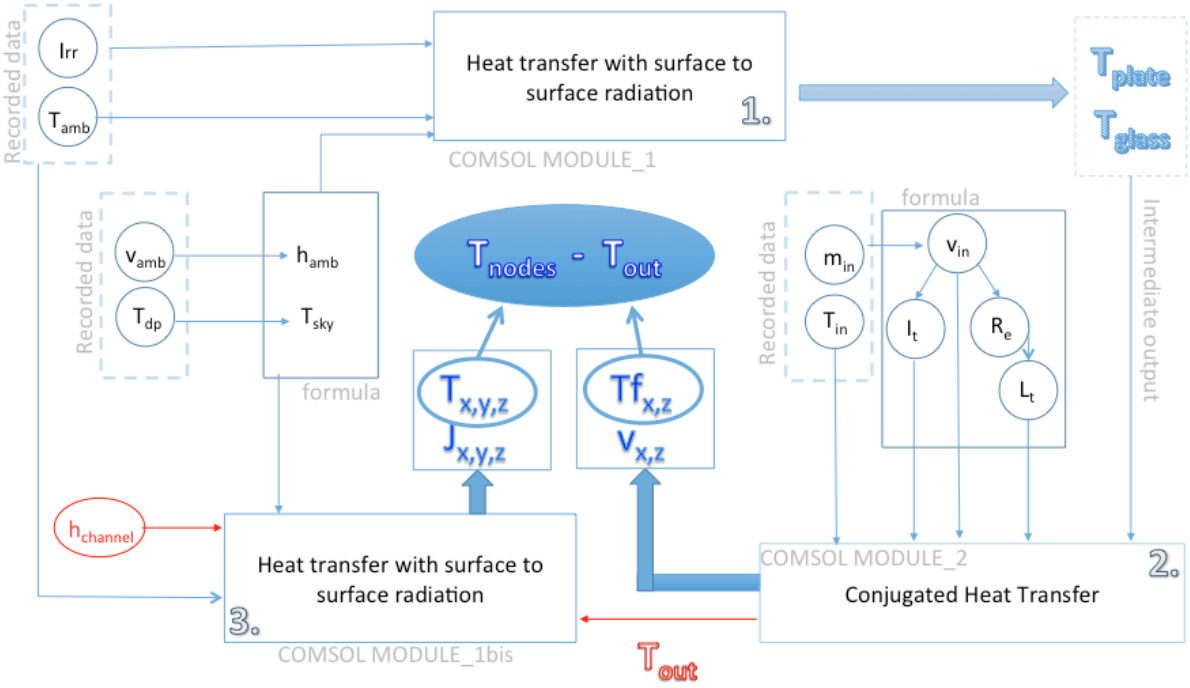

Fig. 35 Flow diagram from the main FEM model.

Algorithm and termination method.

The employed solver for all sub-models is the direct linear solver PARDISO that works on the general system of the form $Ax = b$ using the LU factorization for the matrix A. Termination accounts on Newtonian method for which f(U)=0 where f(U) is the residual vector of solution U, starting from a guess value U_0. A linearized model is then form by the software and solved: $f'(U_0)\delta U = -f(U_0)$. Afterword, next iterations work on $U_n = U_{n-1} + \lambda\, \delta U$ where λ is the dumping factor; error is then estimated with respect to previous iteration $E = f(U_n)/f'(U_{n-1})$ until this value is less then the one in previous iteration by reducing the dumping factor and computing again U_n or until the dumping factor underflows the minimum introduced value for it.

The software stops the iterations when the relative tolerance exceeds the relative error computed as the weighted Euclidean norm:

$$err = \left(\frac{1}{N} \sum_{i=1}^{N} (|E_i|/W_i)^2 \right)^{0.5}$$

where N is the number of degree of freedom and W_i=max(|U_i|, S_i); the scale factor is introduced in the models as the average of solutions U_j for all corresponding $DOFs_i$ times a factor (10-5 to 1, according to the complexity of problem).

It is worth to notice that models 1-3 work with fully-coupled variables while model 2 uses two segregated group: one for domain-wall temperatures and for velocity and pressure fields, another for kappa and epsilon variables. For each group the direct method is applied and required parameters are set as shown in tab. 15.

tab. 15 Termination parameters	models 1-3	model 2
relative tolerance	0.001	0.001
maximum number of iteration	50	300
tolerance factor	1	1
minimum dumping factor	1e-06	1e-06

Physics and geometry, modules 1-3.

In order to stress attention on the radiative heat exchange according to the view factor calculation, a 3D model is chosen. The main geometrical features such as the corrugation lengths (p, l_1, l_2, l_3), height (h) and angle α are introduced as parameters in order to easily modify the geometry if required, see ***Fig. 36***.

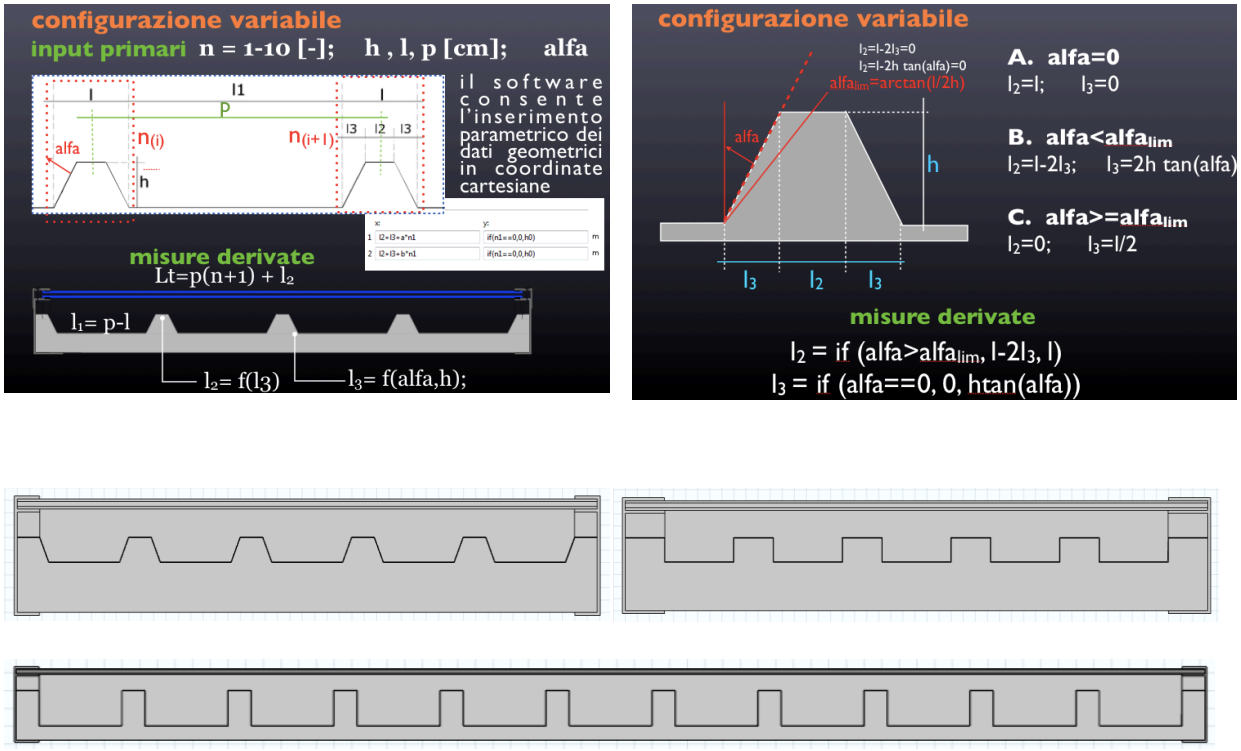

Fig. 36 Corrugation characteristic dimensions (l, l1, l2, l3, a) as well as insulation and air-gap thickness (respectively si and sa) and overall dimensions of the collector (width and length) were introduced as geometrical variable in the parameter schedule.

These models bases on same general equation considering no internal source is provide and steady-state condition are considered:

$$\nabla \cdot (-k\nabla T) = 0$$

Anyway, the modules differ each other for internal boundary physics (cover surface and plate surfaces in configuration A; cover surface, TiNOX up-down surfaces and plate surface for configuration B) while geometries and mesh settings are identical. Specifically the heat transfer between channel walls and fluid stream is quit in module 1 where only radiative exchanges are introduced in order to find out preliminary temperature at glass and plate interfaces to be processed in module 2.

Common Boundaries Conditions. Heat flux conditions in all boundaries are introduced by means of an appropriate heat transfer coefficient and a prescribed temperature. Convective heat flux on upper and bottom surfaces and radiative heat flux on upper cover surface are suitable for describing the main physic phenomena concerning the interactions with the indoor and outdoor ambient. Specifically, wind effects and radiative exchange with the sky at the upper cover surface and convective resistance at the bottom surface. Moreover an other notice comes if prototype and STC-wall are compared; indeed upper boundary is exactly the same in both cases but the bottom boundary for STC wall fronts the indoor while for a stand-alone collector faces again the outdoor. For this reason, even if the main idea of considering an heat flux as boundary condition is maintained for STC-wall model and for prototype model, in the first case the convective coefficient is determined by correlation in function of wind speed while in the second case the most common regulation for determining heat transfer throughout an building envelope component is applied and coefficient value includes both radiative and convective effects toward the indoor ambient. In the same way external temperature is considered for not-integrated elements while fixed indoor temperature for the STC-walls, see tab. 16.

tab. 16 Upper and bottom Boundary condition

upper boundary	$-\boldsymbol{n}\,(-k\,\nabla\,T) = \varepsilon\sigma\left({T_{sky}}^4 - T^4\right)$ $-\boldsymbol{n}\,(-k\,\nabla\,T) = h(T_{ext} - T)$	**Prototype/STC-wall:** T_{ext}=$T_{outdoor}$; h=f(v_{wind})
bottom boundary	$-\boldsymbol{n}\,(-k\,\nabla T) = h(T_{ext} - T)$	**Prototype**: T_{ext}=$T_{outdoor}$; h=f(v_{wind}) radiative effects are neglected
		STC-wall: T_{ext}=T_{indoor}; h from UNI EN ISO 6946 including radiative effects

Symmetry and **open boundary** conditions are then introduced both for prototype and STC-wall respectively at the sides and at inlet/outlet sections in order to stabilise the target results (T_{nodes}). Precisely, symmetry is similar to an insulation condition and it means that there is no heat flux across the boundary:

$$-\boldsymbol{n}\,(-k\,\nabla T) = 0$$

Conceptually it stays for an in-coming/out-coming heat flux across the boundary itself describing hypothetical interaction between two identical symmetrical physical systems. Otherwise, the open boundary means that the heat can flow out of the domain or into the domain with a specified exterior temperature (T_0=T_{amb}). It is introduced to add a boundary condition for modelling heat flux across boundary that could be extended (as it would happen, if a façade component were considered):

$$T = T_0 \qquad \text{if} \qquad \mathbf{nu} < 0$$

$$-\nabla T\,\boldsymbol{n} = 0 \qquad \text{if} \qquad \mathbf{nu} \geq 0$$

Until now, all common features among models referring to STC-wall, prototype and corresponding Configuration A and B have been outlined; following, it will be stressed attention on that features distinguishing the models and specifically configuration A and B. Specifically it regards radiative exchanges and generally internal boundaries conditions that profoundly change between configuration A and B.

Solar source and Internal radiative exchange

Basically, software distinguishes between opaque and transparent materials according to pre-defined wavelength bands by insert wavelength break points that for the analized FEM models is at λ=2500 nm, considering how glass and plate optical properties change in accordance to wavelength. The two bands then correspond to visible and near Infrared spectrum (B1) and middle/far-Infrared band (B2). For this reason, radiative exchange and source are based on the Fraction Emissive Power integral equation from Planck's Law for accounting on wavelenght dependance of radiative exchange:

$$FEP_{Bi}(T) = \frac{15}{\pi^4}\int_{c_2/\lambda_2 nT}^{c_2/\lambda_1 nT} \frac{\xi^3}{e^{\xi}-1}\,d\xi$$

where ξ is the ratio between the constant C_2 and the product among refractive index (n), wavelenght (λ), temperature (T): $\xi = C_2/\,n\lambda T$; while $15/\,\pi^4$=$((C_2/C_1)_S)^{-1}$.

Solar source is then introduced by means of a heat flux power q_0 reaching surfaces and the source temperature (T_s=5760K) for determine the power distribution along the spectrum according to Planck's law and Wien dispacement law, while direction is taken into account by a direction vector ($\mathbf{i_s}$= i_x,i_y,i_z) according to the geometrical reference system:

$$G_{ext,Bi} = F_{ext,Bi}\boldsymbol{i}_s\, q_0 FEP_{Bi}(T_s)$$

Moreover, only the emissivity value in each band is required while absorptivity, reflectivity and trasmissivity coefficient are not directly required, consequently Kirchhoff's law of thermal radiation is applied and $\alpha_{Bi} = \epsilon_{Bi}$. Indeed, trasmissivity coefficient is an on/off option setting: each geometry is opaque or transparent band by band, so the reflectivity coefficient when the medium is opaque is $\rho_\lambda = 1 - \alpha_\lambda = 1 - \varepsilon_\lambda$ otherwise body is totally transparent by default. Analysing the model, differences between configuration A and B are needed. So that, according to previous studies and according to the specified bands definition, glass is transparent into B1 while it is opaque in B2 for enabling green-house effect inside the collectors. For that reason and wanting to introduce the effect of tramissivity properties of glass the trasmission coefficient ($T_{tot} = \tau_\alpha \tau_\rho$, as defined in chapter 3) id directly applied to the radiative power input as follow:

$$q_0 = I_{sun}\mathrm{T}_{tot}$$

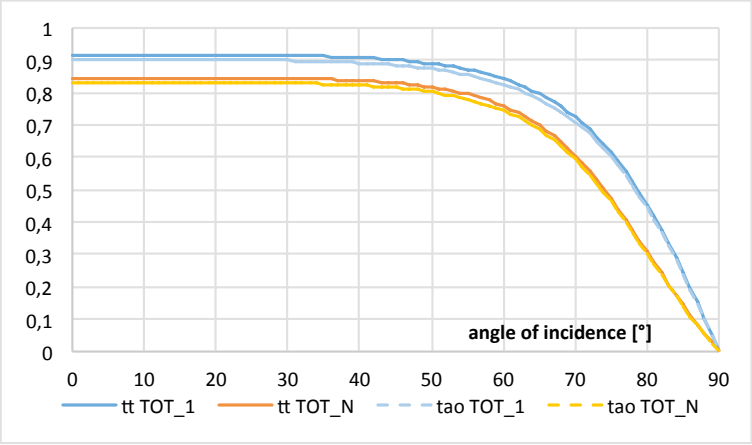

Fig. 37 Trasmissivity angle incidence dependence for a standard glass (n=1.256; k= 4m^{-1}), 1 cover (tt TOT_1 and tao TOT_1) and 2 cover (tt TOT_2 and tao TOT_2); continuous line stays for only trasmissivity effect while dotted line stays for trasmissivity and absorbivity effecst.

Finally, once the surface participating in the radiative exchange are defined as reported in ***Fig. 31*** and ***Fig. 32***, respectively for configuration A and B, "surface to surface radiation" boundary conditions is applied with respect to the defined wavelength bands. Specifically by a general node in the physics interface referring to bulk domain (glass, TiNOX and plate layer) are defined as opaque or transparent, while at surface level radiative exchange are enable where needed band by band, see **tab. 17**. Particularly, it is necessary to distinguishing opaque and transparent domains as well as define band-by-band which surface participates at the radiative exchange with surrounding surfaces and ambient and contemporary with the solar source, then:

- the absorber is opaque and participate to radiative exchange in both band. It regards the upper surface of plate for configuration A and the upper surface of TiNOX for configuration B

- in both configuration glass is transparent in B1 meaning no radiative participation happens as if it did not exist while in B2 radiative exchanges are enable at both bulk and surface level

- the enclosure duct surfaces in configuration B belong all to opaque material but no radiative exchange in B1 is enable since no solar radiation reaches the surface while at the same time they emits/receives radiation by they way they facing each other and by the temperature they reach.

tab. 17	**bulk node**		**surface node**			
			configuration A		configuration B	
	B1	**B2**	**B1**	**B2**	**B1**	**B2**
glass_down	transparent	opaque	none	on	none	on
TiNOX_up	opaque	opaque	-	-	on	on
TiNOX _down	opaque	opaque	-	-	none	on
plate_up	opaque	opaque	on	on	none	on

Radiative thermal balance between surfaces when external source is on is then computed:

$$-\boldsymbol{n}\,(-k\,\nabla T) = \sum_{i=1}^{n} \mathcal{E}_{Bi,u}\left(G_{Bi,u} - e_b(T)FEP_{Bi,u}(T)\right) + \sum_{i=1}^{n} \mathcal{E}_{Bi,d}\left(G_{Bi,d} - e_b(T)FEP_{Bi,d}(T)\right)$$

where *i* is the number of wavelenght band; *u, d* stays for radiation direction, up and down with respect to the reference system and to surface, and $e_b(T) = n^2\sigma T^4$ is the black body radiation.

Finally, G is the sum of different contributions according to band subdivision: the irradiation from external sun source ($G_{ext,Bi}$), the radiation belonging to other surfaces in the model ($G_{m,Bi}$) at the calculated temperature and the radiation coming from outboundaries ambient ($G_{amb,Bi}$) at a given temperature (T_{amb}). Specifically, the latest terms are evalueted once in the *up* direction, once in the *down* direction by means of:

$$(1 - \varepsilon_{Bi})G_{m,Bi} = J_{Bi} - \varepsilon_{Bi} e_b(T) FEP_{bi}(T)$$

$$G_{amb,Bi} = F_{amb,Bi} e_b\left(T^4_{amb,Bi}\right) FEP_{Bi}\left(T_{amb,Bi}\right)$$

Heat transfer at internal boundaries

Internal boundaries, such as outlined in ***Fig.* 38** for both prototype, show radiative and convective resistances introduced in the model by means of:

$$-\boldsymbol{n}\,(-k\,\nabla\,T) = h(T_{ext} - T)$$

As already outlined for the properly duct walls in both configurations (red dotted line in the figure) this boundary conditions are turned on only in module 3, while for air-gap walls they are turned on in both modules 1 and 3. Moreover the meaning of each required temperature (T_{ext}) introduced as input change from one case to the other as well as the unknown h coefficients whose rate is matter of specific calibration processes for both prototype A and B.

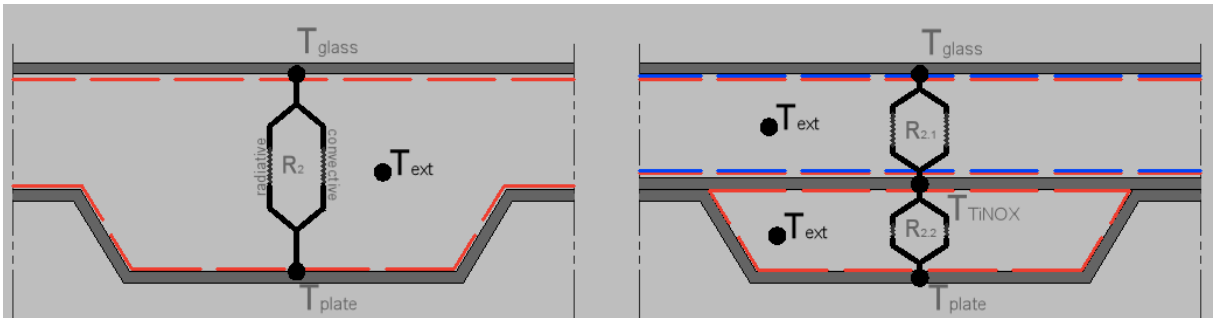

Fig. 38 Boundary conditions at internal walls.

Specifically, in module 3 for conditions at duct boundaries (red dot line in ***Fig.* 38**) in both configurations the required external temperature is the fluid one from model 1-2 while in

model 3 the value of h is assessed comparing results to recorded data and then validated for each examined external condition.

Regarding the air-gap walls (blue dot line in ***Fig.* 38**), it is necessary to distinguish initial values applied in module 1, where fixing $T_{ext}=T_{amb}$ as a first approximation simulations are run until the desired outlet temperature from model 2 reach the recorded one, to that applied in module 3. Once the first two models are calibrated and validated for different external conditions, the $h_{channel}$ value is again assessed in model 3 introducing a correlation for $h_{air\text{-}gap}$ already available in the software and relating h to the corresponding Rayleigh number (see tab. 11) and consequently to temperature difference between the plate. This fact is particularly suitable since plate temperatures themselves affect convective heat transfer between flat plates at different temperature. Following expression is then used:

$$h_{air-gap} = \frac{k_{air} Ra_h}{24\ L}$$

where k_{air} is the air conductivity, h is the plate distance and L the length of collector, while T_{ext} is fixed as: $T_{ext}=(T_{TiNOX}+T_{plate})/2$.

Physics and geometry, model 2.

Second model is suitable for determining the outlet temperature whose values are used as main reference in assessing the mesh as well as in calibrating and validating the model. It is worth to notice that the two models corresponding to the two configuration have the same boundary system and physic while due to the different geometry and distinguishing each inflow velocity specific values for any required parameter need to be assessed case by case.

Two 2D model is chosen sectioning longitudinally the channel in configuration A and B and providing a 90°shape at outlet sections in order to enable properly mixing of the fluid, fig. 21. The dependent variables in the model (field variables) are for the Velocity field **u** (m/s), for the Pressure p (Pa), and for the Temperature T (K), while a Kays-Crawford model is suitable for sorting the heat transfer in turbulence flow according to the general governing equation:

$$\rho c_p \boldsymbol{u} \cdot \nabla \mathrm{T} = \nabla(\mathrm{k}\nabla \mathrm{T})$$

At thermal level, boundary system provides fixed temperature for most of the duct walls and a proper correlation for the duct wall at the exit as shown in ***Fig. 39***; specifically they are:

- temperature at inlet fixing by the author,
- temperature at glass and plate, TiNOX borders belonging to model 1,
- heat flux in the final part of the duct where channel corns at 90°, dot green lines in ***Fig. 39***:

$$-\boldsymbol{n}(-k\ gradT) = \ddot{0}$$

The latter is a suitable boundary condition for convection-dominated heat transfer at outlet boundaries and states that the only heat transfer over the boundary is by convection allowing fluid to mix properly without energy losses toward the external ambient; indeed, the temperature gradient in the normal direction is zero and no radiation exchange influences the heat exchange.

At the same time, parameters characterising the fluid motion are evaluated case by case and applied as input at the Comsol model in order to sort the desired value (T_{out}).

tab. 18 air properties at T=350K [6]

ρ [kg m^{-3}]	cp [kJ(kg K)$^{-1}$]	μ 10^{-7} [Ns m^{-2}]	ν 10^{-6} [m^2 s^{-1}]	k [W (mK)$^{-1}$]	α [m^2 s^{-1}]	Pr [-]
0.9950	1.009	208.2	20.92	0.030	29.9	0.700

Reynolds number as well as the friction factor is then suitable to identify the flow region by means of Moody diagram, ***Fig. 40***. Specifically Reynolds number at the different velocity is based on hydraulic diameter: $D_h = 4Area/Perimeter$, referred to the transversal section of the collector: the channel with its corrugations in prototype A and the typical channel in prototype B, ***Fig. 39***.

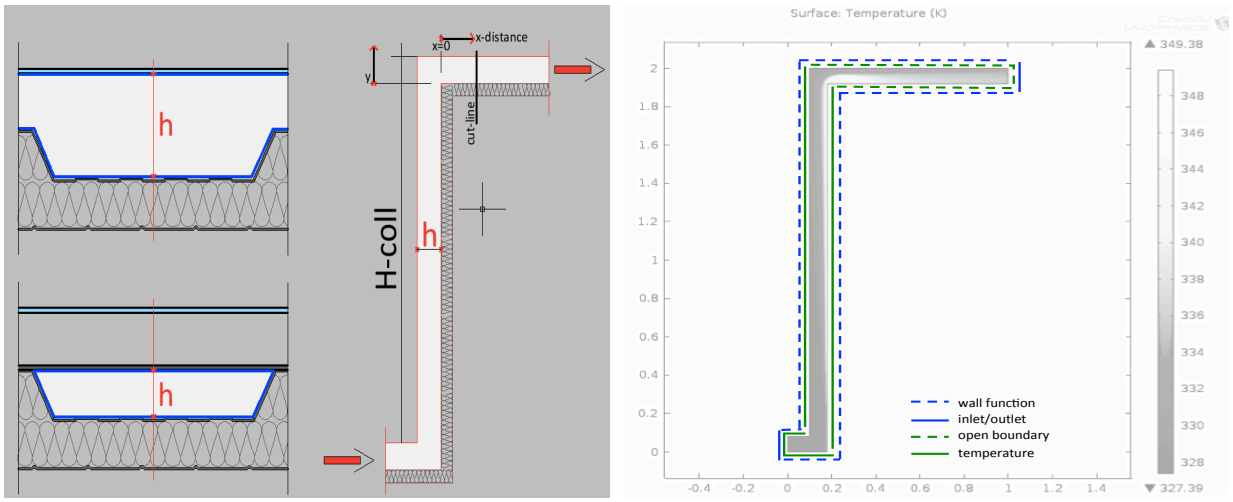

Fig. 39 Fluid flow geometry, prototype A - B comparison on the left, boundary conditions scheme on the right.

Once Reynolds number is computed, Petukhov correlation (f_P) as reported in **[6]** usable in a Reynolds range between 3000 and $5*10^6$ and the common correlation (f) for Re<3000 allow determining the friction factor at the sorted Reynolds number and consequently the fluid flow region, tab. 19.

$$Re_{Dh} = \frac{v\, D_h}{\nu}$$

$$f_P = (0.790\ \ln Re_{Dh} - 1.64)^{-2} \qquad ; \qquad f = \frac{64}{Re_{Dh}}$$

tab. 19 Fluid Flow field

reference			mass flow rate	v [ms^{-1}]	Re	friction	lam	trans	turb
prototype A	D_h=0,14 m	A.1	m= 0.01 [$m^3m^{-2}s^{-1}$]	0.14	1235	0.05		x	
		A.2	m= 0.03 [$m^3m^{-2}s^{-1}$]	0.41	3615	0.04		x	
		A.3	m= 0.05 [$m^3m^{-2}s^{-1}$]	0.69	6084	0.04		x	
prototype B	D_h=0,06 m	B.1	m= 0.01 [$m^3m^{-2}s^{-1}$]	0.24	848	0.08		x	
		B.2	m= 0.03 [$m^3m^{-2}s^{-1}$]	0.73	2579	0.05		x	
		B.3	m= 0.05 [$m^3m^{-2}s^{-1}$]	1.22	4309	0.04		x	

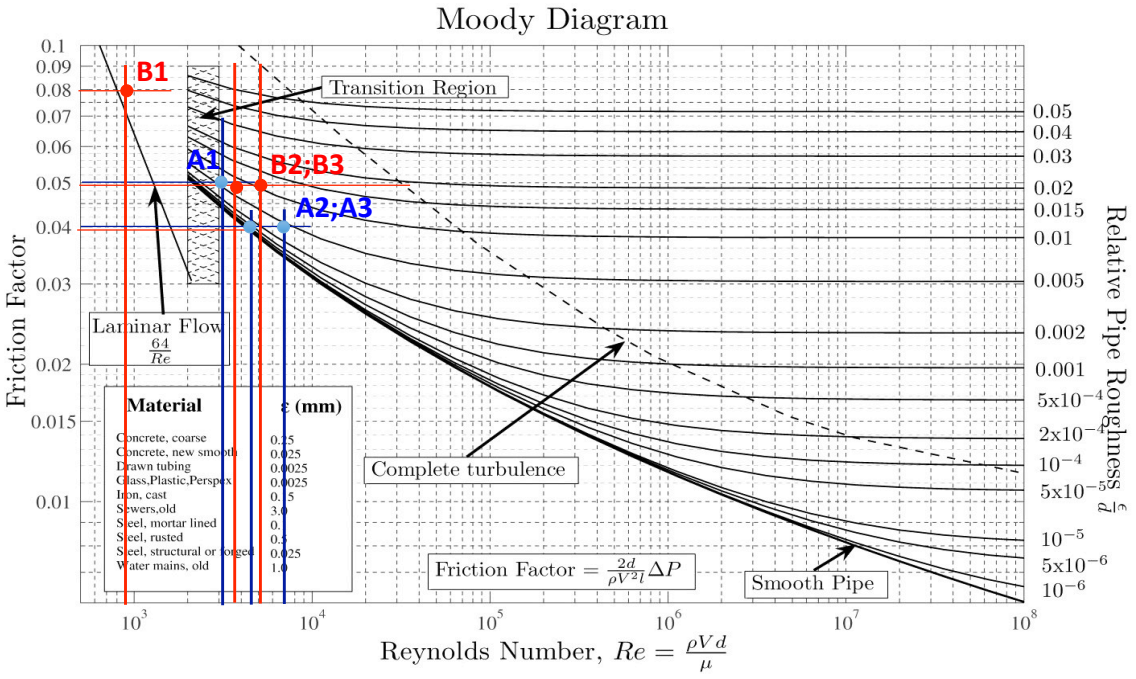

Fig. 40 Moody diagram and fluid flow region identification for each case, points are addressed according to table 10.

As a result, assuming the flow fluid is incompressible and Newtonian, κ– ϵ model is used and RANS equations applied:

$$\rho\,(\boldsymbol{u}\cdot\nabla)\boldsymbol{u} = \nabla\cdot\left[-p\boldsymbol{I} + (\mu+\mu^T)(\nabla\boldsymbol{u}+(\nabla\boldsymbol{u})^T) - \frac{2}{3}(\mu+\mu^T)(\nabla\cdot\boldsymbol{u})\boldsymbol{I} - \frac{2}{3}\rho k\boldsymbol{I}\right] + F$$

$$\nabla\cdot(\rho\boldsymbol{u}) = 0$$

$$\rho\boldsymbol{u}\cdot k\nabla = \nabla\left[\left(\mu+\frac{\mu_T}{\sigma_k}\right)\nabla k\right] + P_k - \rho\epsilon$$

$$\rho\boldsymbol{u}\cdot\nabla\epsilon = \nabla\left[\left(\mu+\frac{\mu_T}{\sigma_\epsilon}\right)\nabla\epsilon\right] + C_1\frac{\epsilon}{k}P_k - C_2\frac{\epsilon^2}{k}\rho$$

where μ is the dynamic viscosity, μ^T is the turbulent dynamic viscosity, p the pressure, ρ the density of fluid, k is the turbulent kinetic energy, P_k the production rate and F the volume force. Specifically, k ϵ P_k and μ^T are related each others in the models by:

$$P_k = \mu_T \left[\nabla \boldsymbol{u} : (\nabla \boldsymbol{u} + \nabla \boldsymbol{u}^T) - \frac{2}{3}(\nabla \cdot \boldsymbol{u})^2 \right] - \frac{2}{3}\rho k \nabla \cdot \boldsymbol{u}$$

$$\mu^T = \rho C_\mu \frac{k^2}{\epsilon}$$

where L is the length scale while σ_ε, σ_κ, C_1, C_2 and C_μ are five parameters whose common values introduced in the model are shown in tab. 20.

tab. 20 Model constant values

σ_ε=1.3	σ_κ=1	C_1=1.44	C_2=1.92	C_μ=0.09	k_v=0.41	B=5.2

Regarding the boundaries, it is possible to distinguish the inlet section from the outlet where specified condition respectively of velocity and pressure are imposed from all the others boundary where the wall function are applied, ***Fig. 39***.

Wall function boundaries.

Wall functions are generally employed in the region nearby a solid wall where the usual expression for k and epsilon are not valid anymore. The model automatically computes such a distance from the wall channel:

$$\delta_w^+ = \frac{\rho u_\tau \delta_w}{\mu}$$

where δ_w^+ is the so called wall lift-off in viscous unit, δ_w is the wall lift-off in meter while u_t is the friction velocity: $u_\tau = {C_\mu}^{1/4}\sqrt{k}$ which becomes 11.06. This distance defines the part of domain where wall functions (see tab. 21) are applied to calculation; then introducing the no-penetration condition: $\boldsymbol{u} \cdot \boldsymbol{n} = 0$ where u is the velocity vector and n the diretional one; while $\boldsymbol{u}_{tang} = \boldsymbol{u} - (\boldsymbol{u} \cdot \boldsymbol{n})\boldsymbol{n}$ it follows that at boundaries stays:

$$\left[(\mu + \mu^T)(\nabla \boldsymbol{u} + (\nabla \boldsymbol{u})^T) - \frac{2}{3}(\mu + \mu^T)(\nabla \cdot \boldsymbol{u})\boldsymbol{I} - \frac{2}{3}\rho k \boldsymbol{I} \right] \boldsymbol{n} = -\rho \frac{u_T}{\delta_w^+} \boldsymbol{u}_{tang}$$

The turbulent kinetic energy is subject to a Neumann condition $(\boldsymbol{n} \cdot \nabla k) = 0$ and, introducing the von Kàrman constant (k_v) the boundary condition for epsilon reads:

$$\epsilon = \frac{C_\mu^{3/4}\, k^{3/4}}{k_v \delta_w}$$

tab. 21 wall functions

Increasing Reynolds number the viscous sublayer of a boundary layer is so thin that it is difficult to use enough grid points to resolve it. This problem could be avoided by introducing the wall functions which rely on the existence of a logarithmic region in the velocity profile. Models accounts on: $$u_\tau = \frac{\lvert u \rvert}{k_v^{-1} \ln(\delta_w) + B}$$ where k_v is the von Kàrman constant and B is an empirical constant related to the thickness of the viscous sublayer.	Velocity profile as a function of distance normal to the wall: experimental data (solid line) versus results from formula. 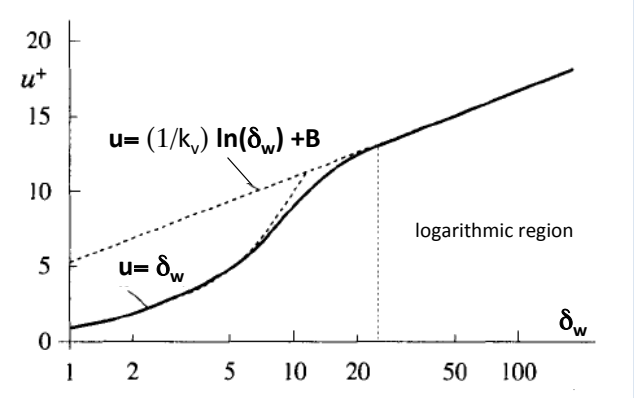 **[5]**

Inlet boundary.

At inlet, a normal flow velocity value (U_o) on which kinetic energy and dissipation rate depend to is introduced. Consequently, at inlet boundary it reads:

$$\boldsymbol{u} = -U_0 \boldsymbol{n}$$

$$\boldsymbol{k} = \frac{3}{2}(\boldsymbol{U_0}\, \boldsymbol{I_T})^2 \qquad\qquad \boldsymbol{\epsilon} = \boldsymbol{C_\mu}^{3/4} \frac{\boldsymbol{k}^{3/2}}{\boldsymbol{L_T}}$$

As known, k and epsilon values at boundary are seldom available for that reason software introduces the previous approximations in function of the turbulent intensity (I_T) and the turbulent length scale (L_T) whose values are required. Specifically, the turbulent intensity is defined as $I_T = \sqrt{\overline{u^2}}/U_0$ and is approximately 1-20% with respect to the inflow velocity **[4]** while the turbulent length scale being the measure of the eddies size varies generally from 0.01-1 with respect to the typical scale of **[4]**. Present study relies with the following assumption from **[4]**:

$$l_T = \sqrt{Re}\, D_h \qquad\qquad I_T = \frac{v}{10}$$

Outlet boundary.

Considering no relevant variation in pressure could be recorded, the outlet section condition is provided by a constant pressure value (p_0=1atm) discharging viscous stress, for which consequently follows:

$$p = p_0 \qquad \nabla k \cdot \boldsymbol{n} = 0 \qquad \nabla \epsilon \cdot \boldsymbol{n} = 0$$

$$\left[(\mu + \mu^T)(\nabla \boldsymbol{u} + (\nabla \boldsymbol{u})^T) - \frac{2}{3}(\mu + \mu^T)(\nabla \cdot \boldsymbol{u})\boldsymbol{I} - \frac{2}{3}\rho k \boldsymbol{I}\right] \boldsymbol{n} = 0$$

Mesh for solid domain - module 1-3

Considering the main change in temperature field will be recorded in the transversal direction a swept method for mesh generation is suitable; different mesh configurations are performed and results compared. Specifically the temperature trend in the cross section at the middle length of the component ($T_{(H/2,p/2,z)}$) is considered for this purpose. Tests were made just on prototype A model since the two model are substantially the same at mesh assessment level. Both triangular and quadrilateral shapes were tested; moreover hence plate and glass thicknesses are really different from that of insulation panel two main features are used. The minimum and maximum dimensions for mesh elements in cross direction are proportional to the plate and glass thicknesses while the number of element along the collector length is set at 40. It is worth to notice that plate thickness, as well as TiNOX layer, is extremely small making difficult to design the mesh elements; for this reason a higher thickness is introduced choosing a *conductive equivalent coefficient*. In this way, at least 3 mesh elements in the cross direction along glass plate and TiNOX thicknesses is assured bettering the results resolution in the reason why 3 temperatures are available for each layer field and are evaluated at different boundary conditions in each element: one mesh element bounds with the outdoor ambient, another to the inside model and another stays in between. This involves that mesh element dimensions and characteristics for glass, plate and TiNOX layer are fixed a part of other: specifically the maximum and minimum dimensions are always equal to $s_p/3$ while the element growth rate at so small dimensions is not influent. At the same time the minimum element size for insulation domain are fixed at $s_p/3$ in order to ensure continuity between plate and insulation meshes.

Moreover, minimum and maximum dimensions for mesh element were varying in the case of insulation and wall layers, according to table 9. Reciprocal temperature difference between models with different mesh design are computed once for the triangular shape element, once for the quadrilateral ones; finally results among each shape are compared each other. *Fig.* 22 shows no relevant differences in results among the different mesh design: doubling the number of element and the total DOFs the difference is less than 0,1 °C. Mesh 5 configuration with triangular element is then chosen allowing a faster calculation.

tab. 22 mesh	minimum size	maximum size	growth rate
M1	1/3 s_p	$4s_p$	1.50
M2	1/3 s_p	$3s_p$	1.50
M3	1/3 s_p	$2s_p$	1.50
M4	1/3 s_p	s_p	1.50
M5	1/3 s_p	s_p	1.25

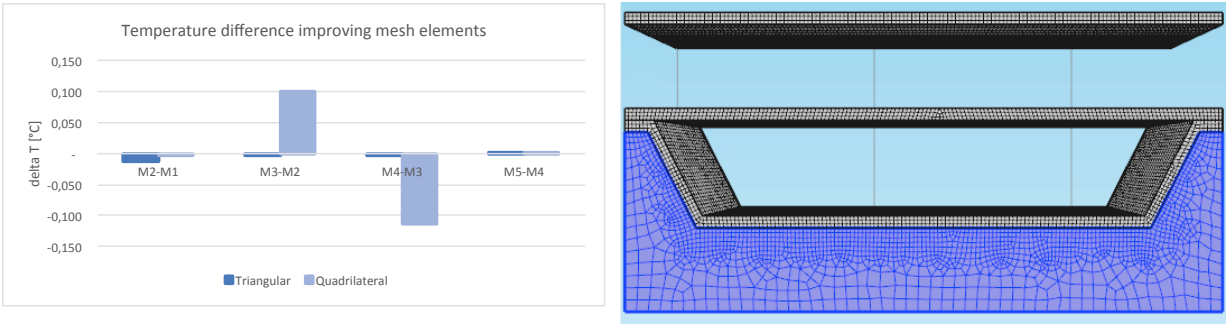

Fig. 41 Validation of mesh design according to Prototype A model (right) and resulting meshing in Prototype B (left)

Mesh for fluid domain – module 2

Once the main feature for fluid domain are established according to the physics, software determines a physic-controlled mesh that is the same for both prototypes and it is introduced as reference (M1) in mesh independence test. It is worth to notice that element growth rate is almost 1 and cannot be changed anymore while it is possible to reduce size of mesh element or improve the resolution for boundary layers in which wall functions are applied. Meshes varies then according to table 10; specifically once the elements size are

equal to the half of those in M1 (it is M2 mesh); once boundary layer are doubled (M3) and finally M4 includes both changes with respect to M1.

tab. 23 Prototypes A-B, mesh features for independent test

MESH	n. BND layer	BND-layer thickness	maximum element size	minimum element size	element growth rate
M1	5	0.0134	0.0067	2E-05	1.05
M2	5	0.0134	0.0067*0,5	1E-05	1.05
M3	10	0.0134/2	0.0067	2E-05	1.05
M4	10	0.0134/2	0.0067*0,5	1E-05	1.05

If comparing the desired output value (T_{out}) sorted at the exit of the channel and computed point by point along the cut line, no relevant differences are noticed. Specifically M3-M1 difference is 0.03K while comparing M2-M1 and M4-M5 0,1K difference is recorded. Ratio between results for M2-M3-M4 different meshes with respect to M1 is anyway equal to 100%. For that reason and considering such a difference cannot affect efficiency curve results, M1 is chosen as mesh for next analysis. Once this resolution for mesh is defined, it is checked for first if the computed wall lift-off in viscous unit is at least equal to 11.06 and the resulting δ_w compared with the characteristic dimension of channel is appropriate. For all models at different inlet velocity the first check is verified δ_w^+=11.06 all along the wall, while the lift-off δ_w is generally small enough if compared to the characteristic dimension of the two ducts. Only results for the lowest specific volumetric flow rate shows higher results for the maximum δ_w dimension as shown in ***Fig. 42***.

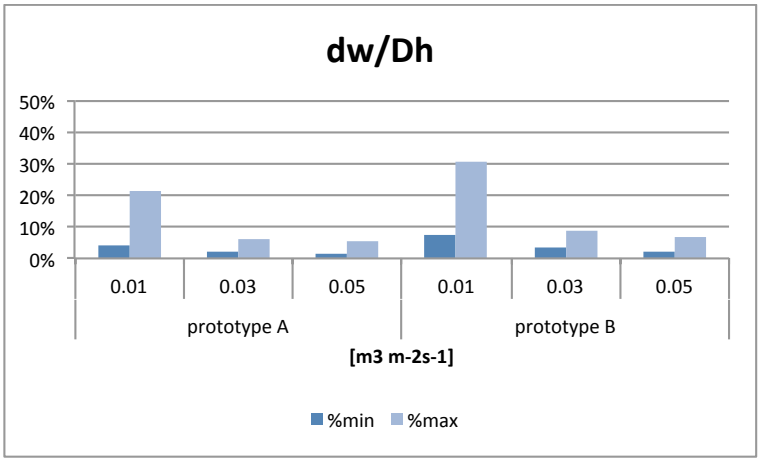

Fig. 42 Wall lift-off ratio with respect to the D_h for configuration A-B and at different inflow velocity

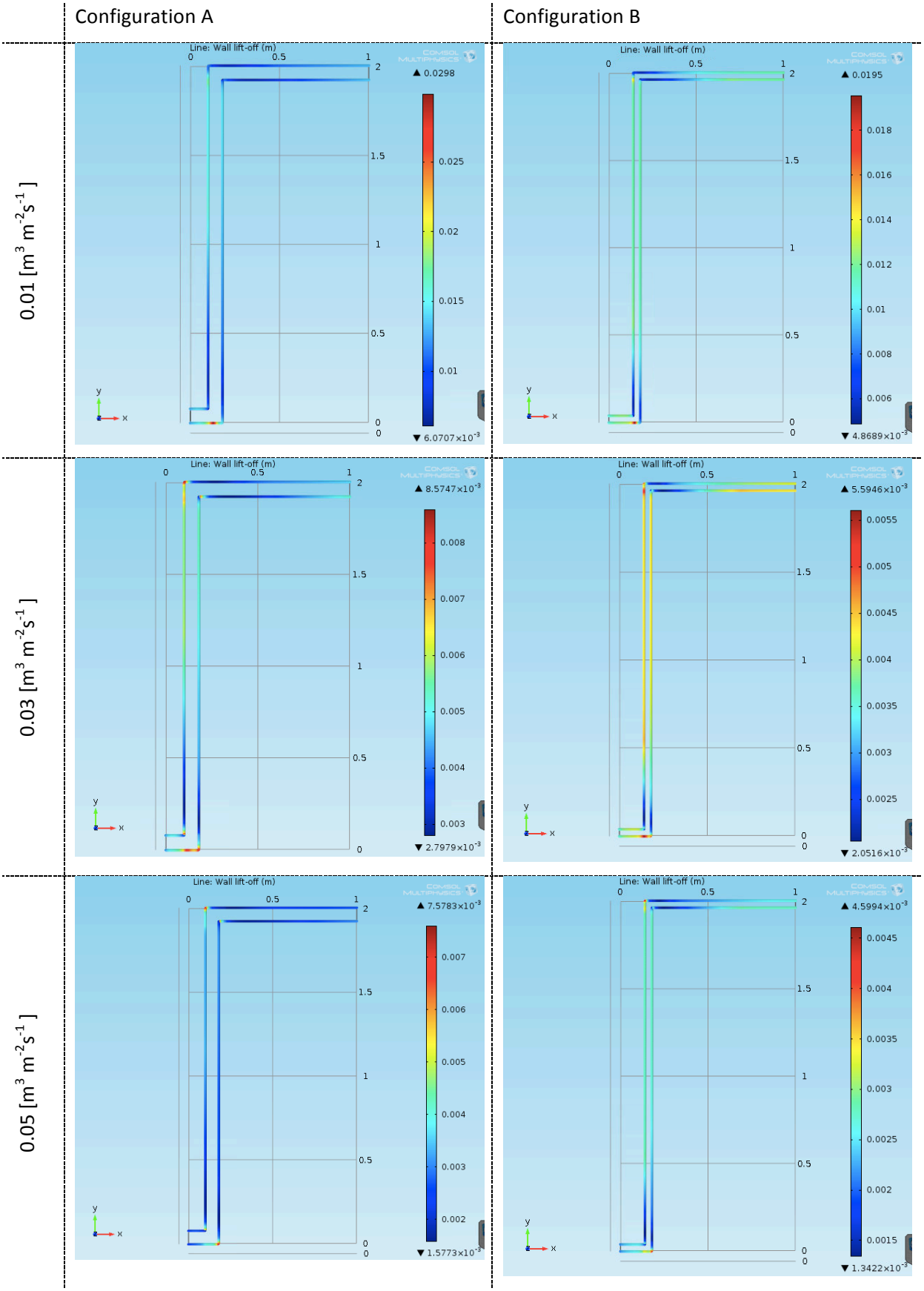

Fig. 43 Wall lift-off results for the two configuration and at different inflow velocity.

Sorting outlet temperature

Once mesh and boundary layers are defined, it is necessary to identify the right cut-line (x-distance in ***Fig. 39***) where fluid is properly mixed and the evaluated averaged T_{out} suitably represent the exit temperature. For this purpose the standard deviation (σ) with respect to the average temperature value along the cut-line x=a; as well as the comparison between the T_{out} arithmetic average value and the weighted value with respect to velocity are considered.

$$T_{out,x} = \frac{\sum_{y=0}^{100} T_{out(x;y)}}{100}$$

$$T_{out\_w,x} = \frac{\sum_{y=0}^{100} \left(T_{out(x;y)} * u_{(x;y)}\right)}{\sum u_{(x;y)}}$$

where 100 represents the number of temperature/velocity values sorted along the generic x=a cut-line whose position varies from a=0 until a=0,8 m, see *fig.* 21. This procedure is reiterated for prototype A and B at the different inflow velocity and results shown in *fig.* 22. At first sight, it is evident prototype A and prototype B have different behaviour according to their specific geometry since no relevant difference varying inlet velocity are recorded in each group of results. Moreover, the group referring to prototype B achieve an asymptotic behaviour at x=0, 4m and a really low standard deviation value is found, σ=0.01.

Meanwhile, the minimum magnitude of σ in Prototype A cluster is 0,7K at x=0.8 m for m=0.05 $m^3m^{-2}s^{-1}$. Even if the curve does not achieve an appropriate slope; the sorted value is considered reliable with the present analysis considering also further analysis in tab. 24, tab. 25, tab. 26, tab. 27, tab. 28, tab. 29. Indeed if the velocity profile at different cut-line position is considered, profiles at x=0.8m for prototype A shows an appropriate trend and differences between arithmetic and weighted average values tend to nullify.

Considering all that reasoning and having achieve appropriate accuracy in sorting T_{out}, arithmetic mean values at x=0,08m are considered in the present work for the following analysis.

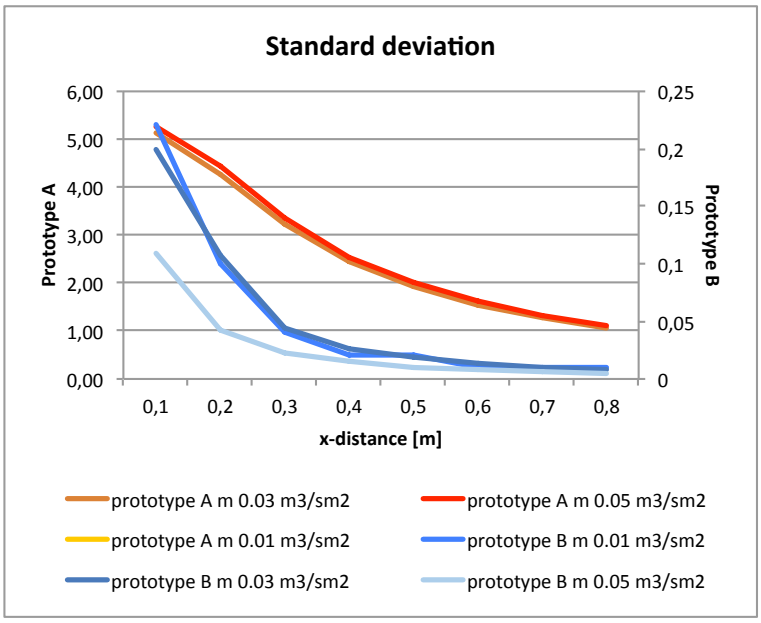

Fig. 44 Standard deviation of outlet temperature for prototype A and B at the different x-distance of cut-line form entrance to exit.

tab. 24 Prototype A - 0.01 [$m^3\ m^{-2}s^{-1}$]	
$v_{min}=5.65\ 10^{-7}$	$v_{max}=0.25$

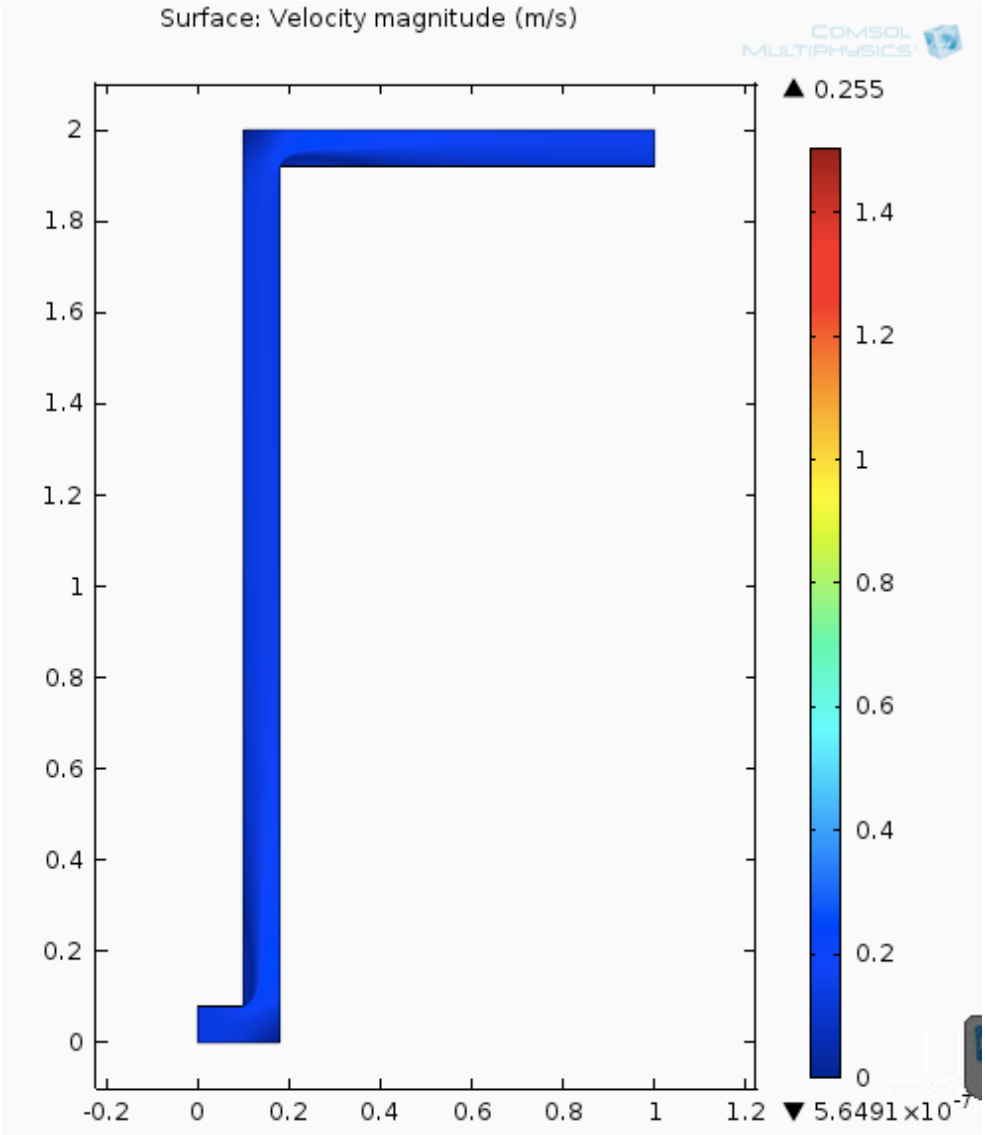

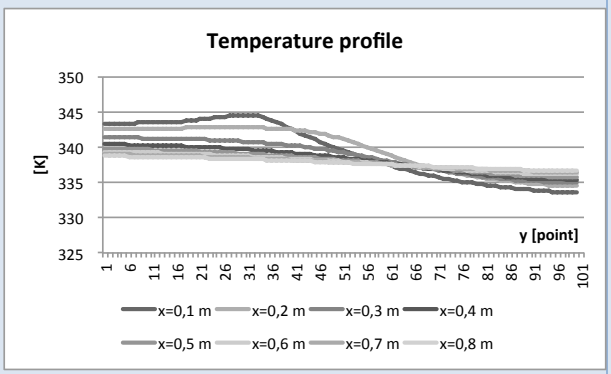

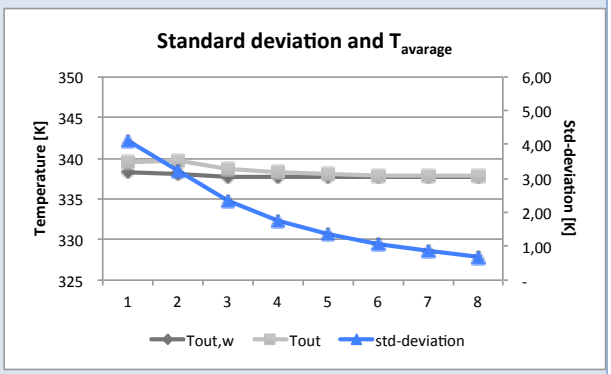

CUT LINE AT 0.8 m, σ=0,69 K

tab. 25 Prototype A - 0.03 [$m^3\ m^{-2}s^{-1}$]	
v_{min}=4.29 10^{-6}	v_{max}==0.77

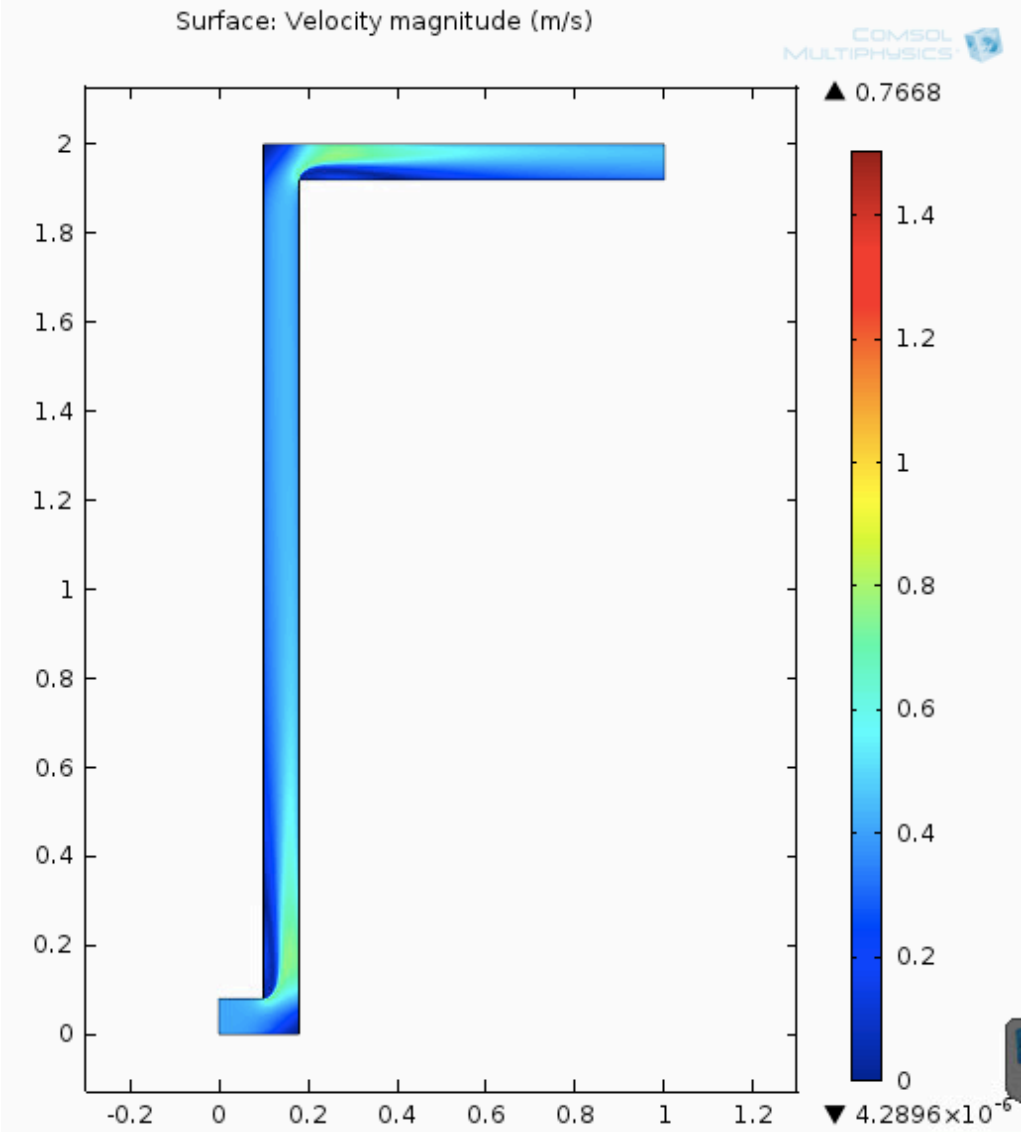

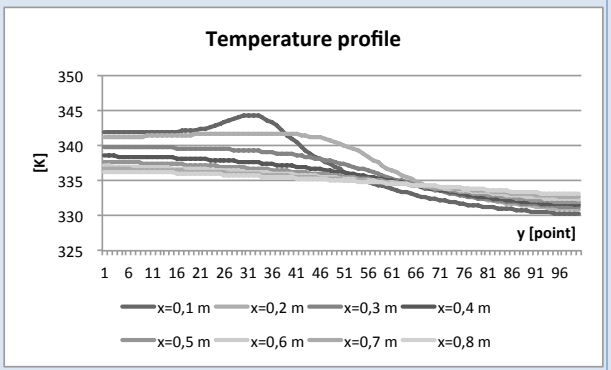

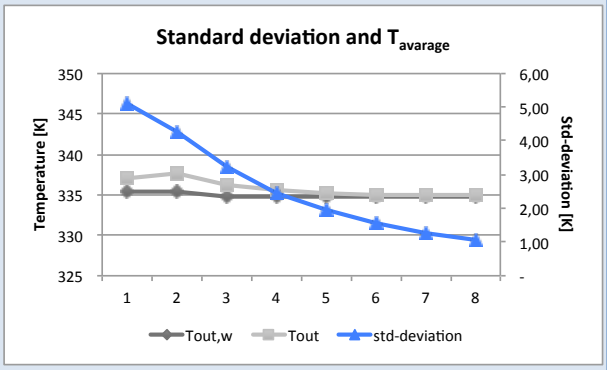

CUT LINE AT 0.8 m, σ=1,05 K

tab. 26 Prototype A - 0.05 [$m^3\ m^{-2}s^{-1}$]	
v_{min}=5.39 10^{-6}	v_{max}=1.4

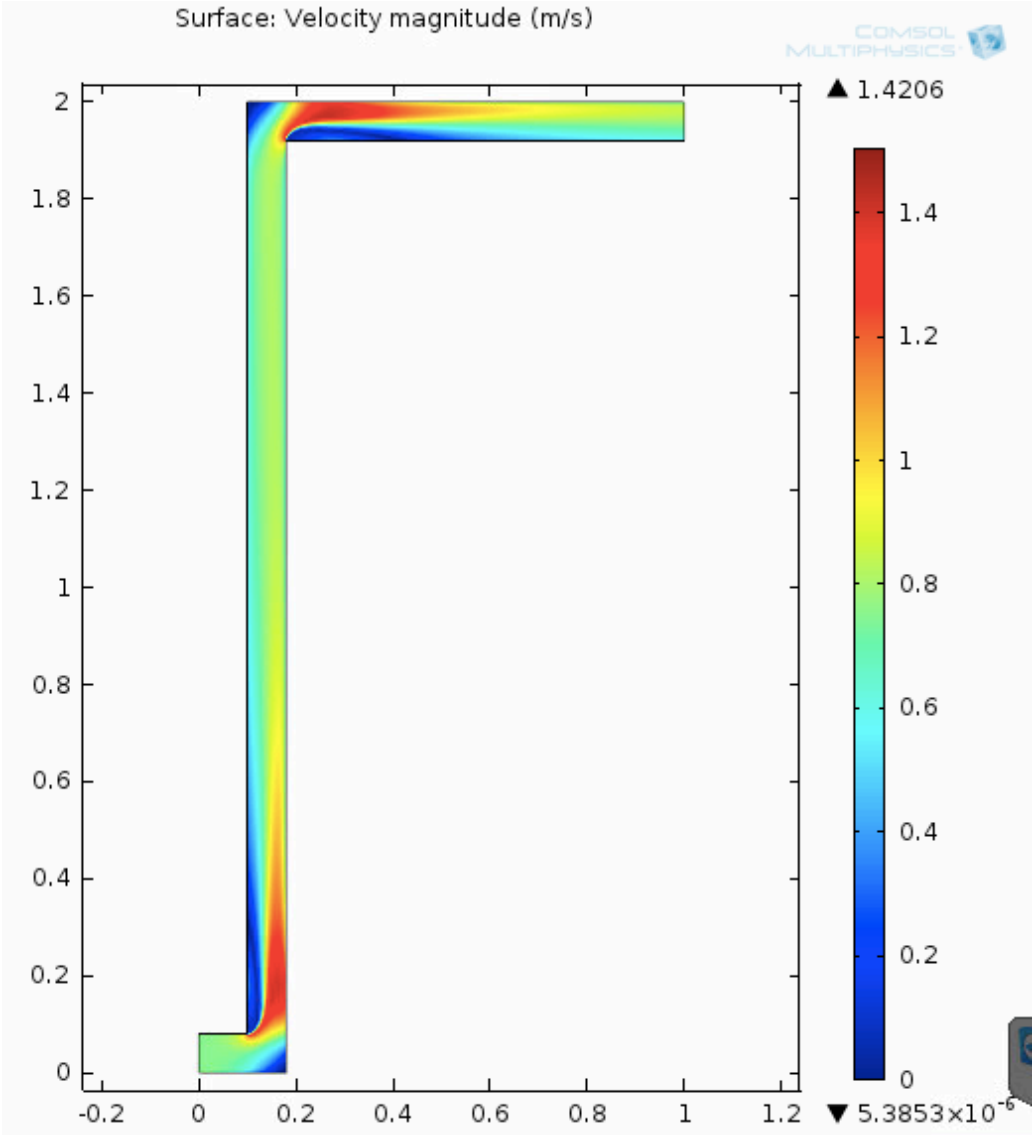

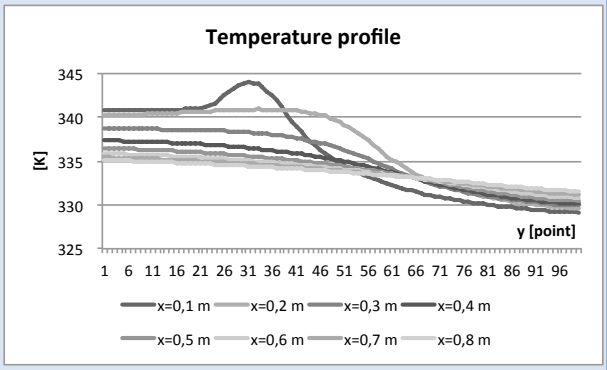

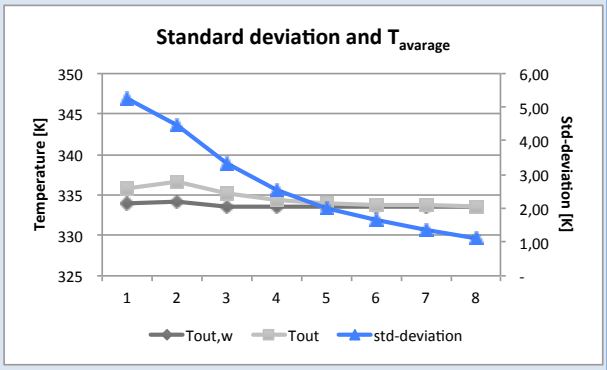

CUT LINE AT 0.8 m, σ=1,11 K

tab. 27 Prototype B - 0.01 [$m^3\ m^{-2}s^{-1}$]	
$v_{min}=5.39\ 10^{-6}$	$v_{max}=0.42$

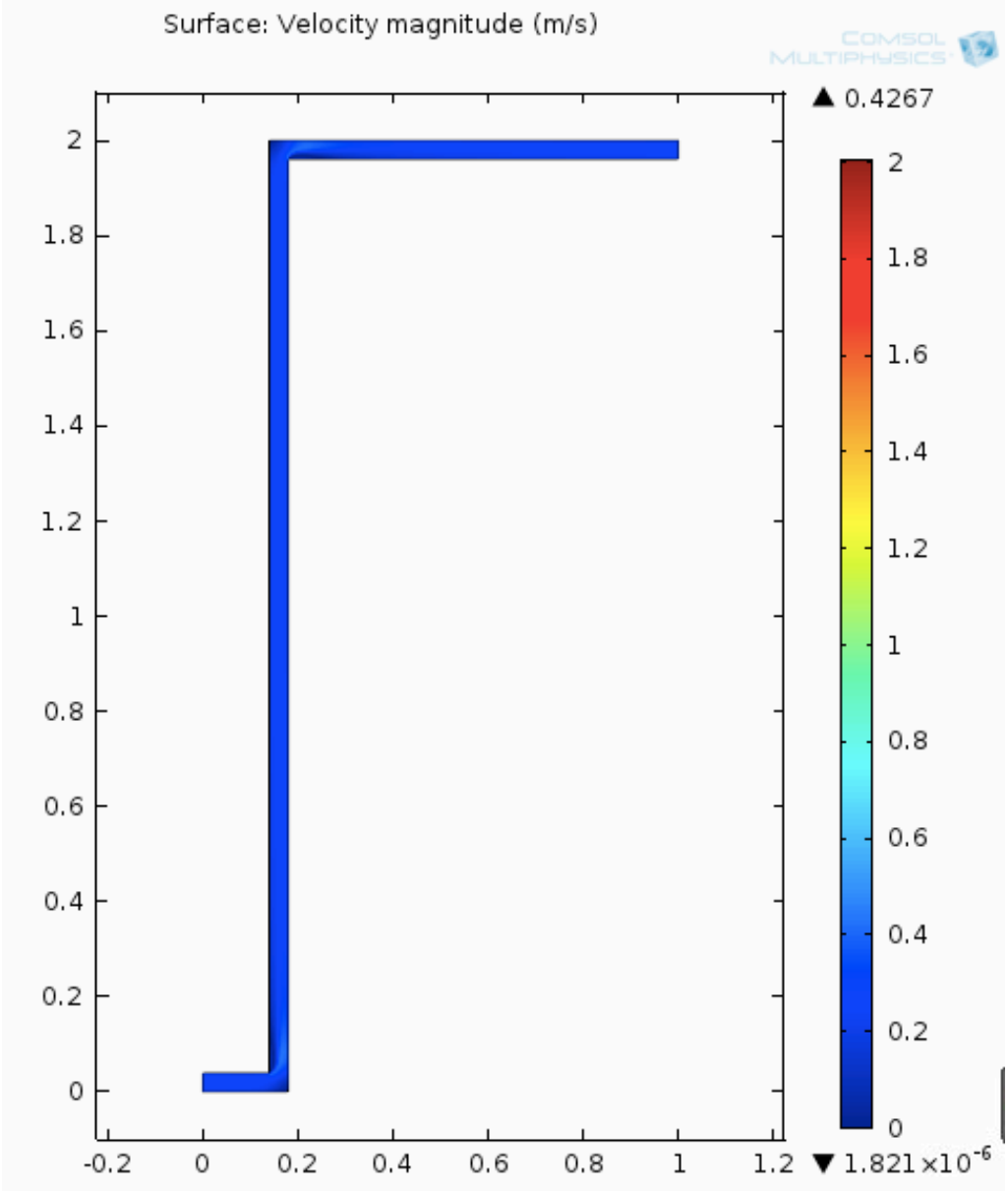

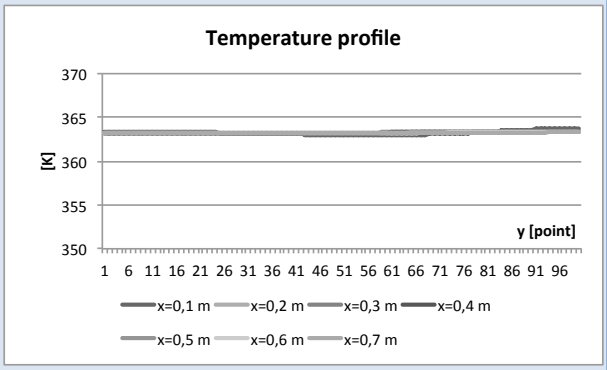

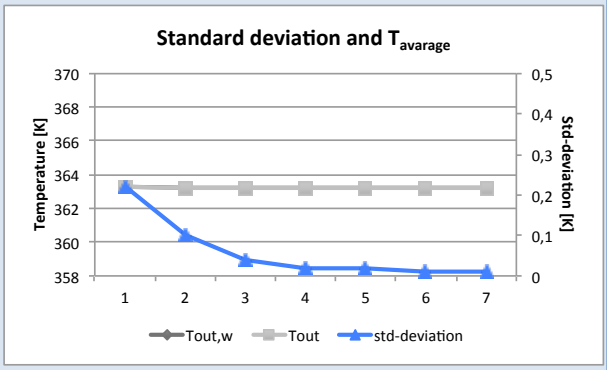

CUT LINE AT 0.8 m, σ=0,01 K

tab. 28 Prototype B - 0.03 [m3 m-2s-1]	
v_{min}=5.39 10^{-6}	v_{max}=1.4

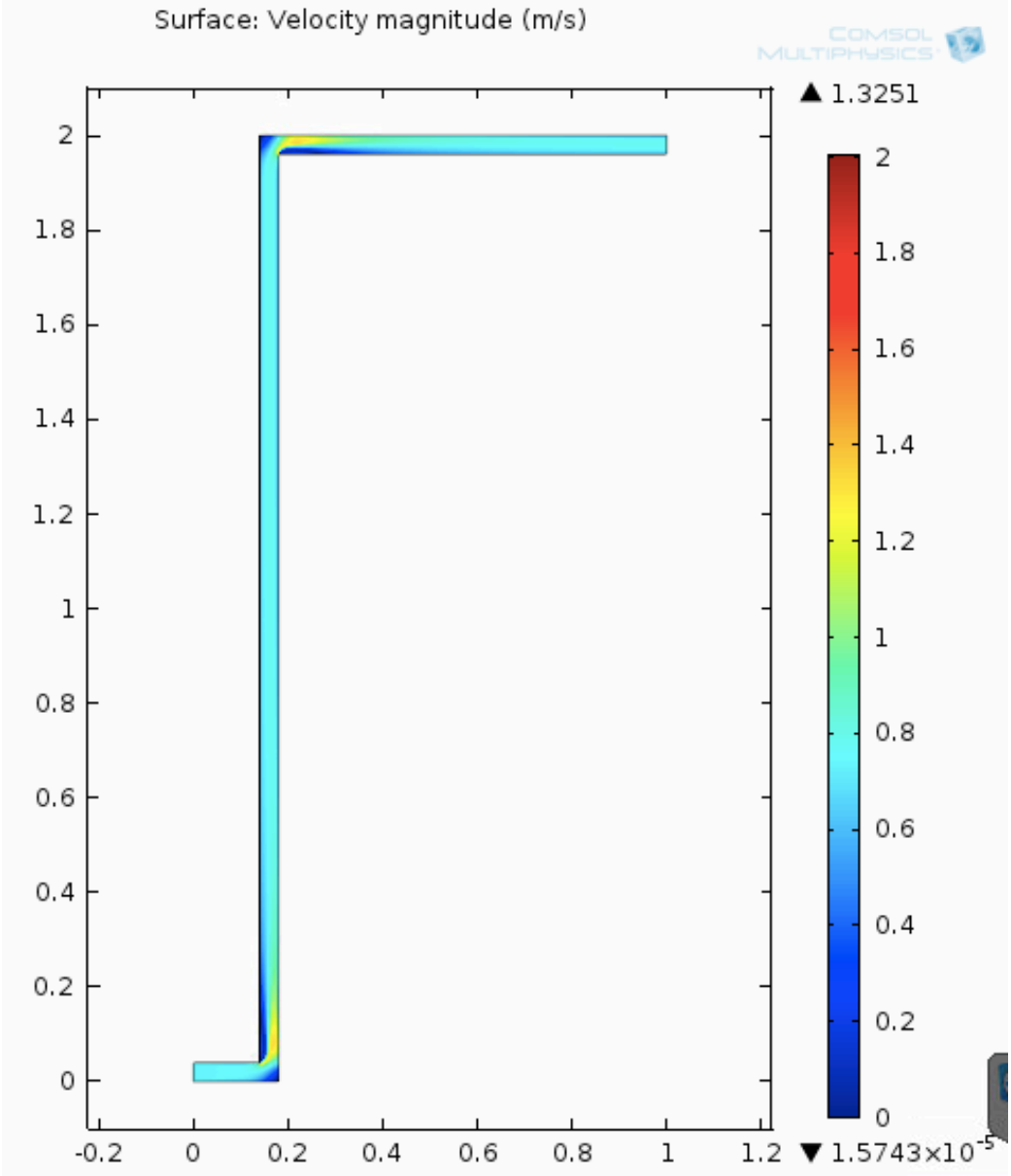

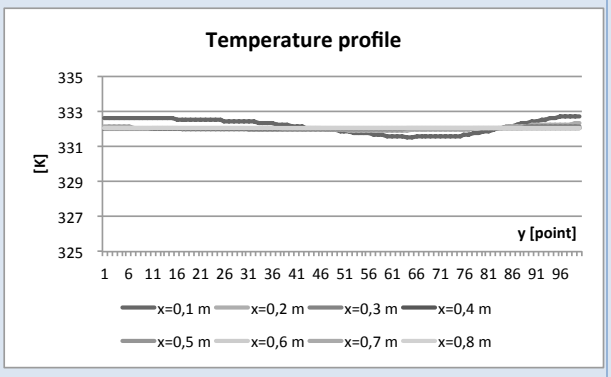

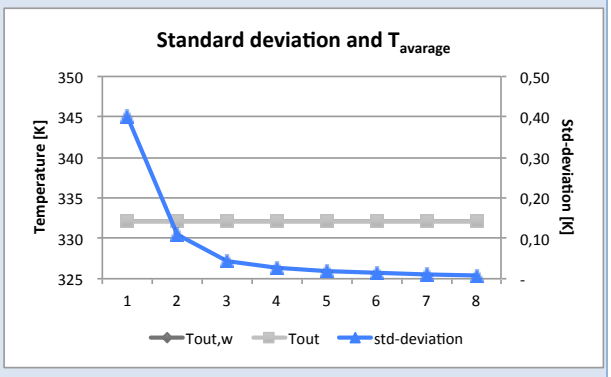

CUT LINE AT 0.8 m, σ=0,01 K

tab. 29 Prototype B - 0.05 [$m^3\ m^{-2}s^{-1}$]	
v_{min}=2.12 10^{-5}	v_{max}=2.2

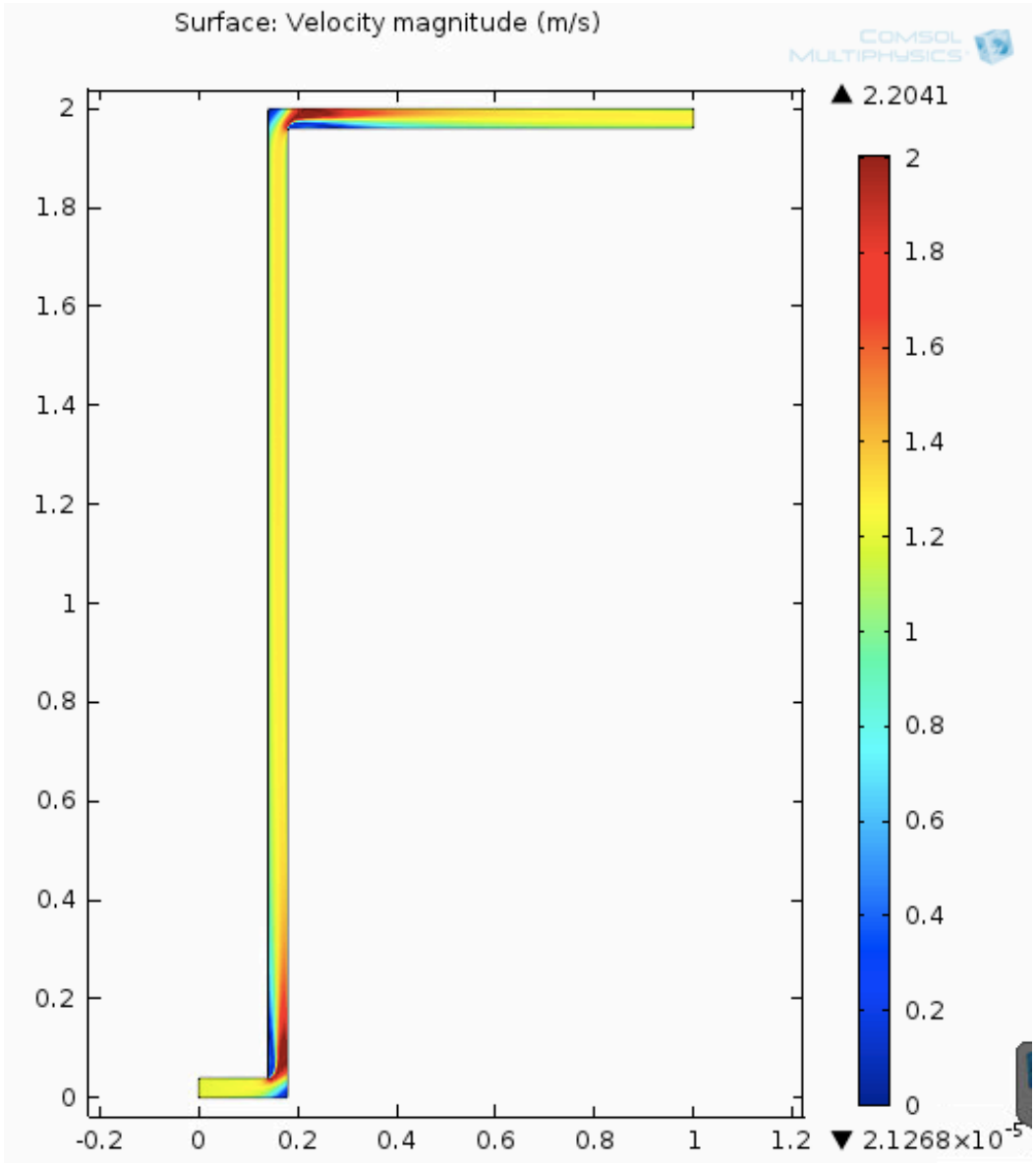

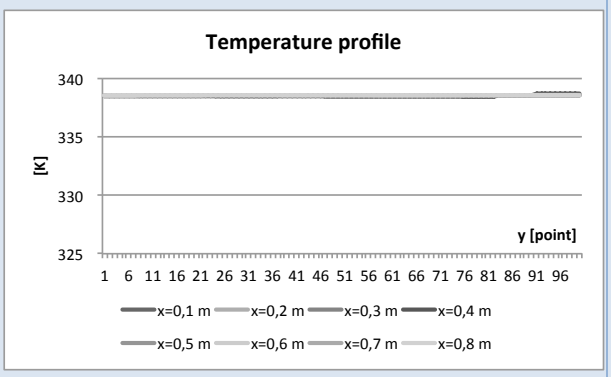

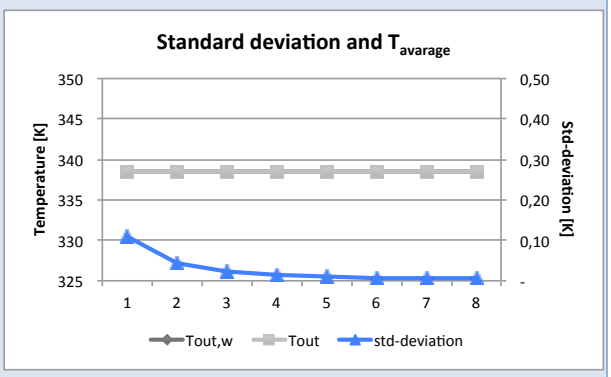

CUT LINE AT 0.8 m, σ=0,01 K

4.2 Validation and calibration.

Data and Initial Conditions. Validation and calibration account on model purposes, T_{out} and T_p are then the detected value for comparing the software outputs to the available recorded data. Weather data and checked temperatures from the experimental campaigns are recorded with a 30 second time step, and are then processed in order to obtain average value in a time-lapse about 15-20min. Only time-lapse when steady-state conditions are achieved are chosen, according to standard prescription for sorting consistent efficiency curve. Moreover, some inputs not directly detected during the experimental campaign are evaluated by means of appropriate correlations from literature starting from the available recorded data and physical working condition.

Differences between Prototype A and B are furthermore necessary if it is considered that calibration parameters change according to the physics at internal boundaries and available data are detected during two different experimental campaign. Specifically, some needed input are actually unknown and values are determined by a calibration procedure whose results are afterwards validate for each chosen ambient condition. Such values are:

- emissivity coefficients for plate (ε_{B1}, ε_{B2}) and heat transfer coefficient at duct walls ($h_{channel}$) in prototype A;
- heat transfer coefficient at duct and at air gap walls ($h_{channel}$, $h_{air\text{-}gap}$) in prototype B.

A general criterion is introduced for sorting reliable value and only solutions leading to a deviation less then 5% from recorded data are considered valid.

Prototype A

It is worth to notice that two are the main unknown inputs: the plate emissivity and the convective coefficient at duct walls; model is then calibrated according to these unknown parameters for the higher irradiation condition and then calibrated considering all other sorted external conditions. Specifically emissivity values were suitable for calibrating the model 1 and 2; while convective coefficient is used for the same purpose in model 3. In this way the whole FEM model works correctly in such a specified range of irradiation value.

tab. 30 shows all the needed input at external boundaries distinguishing data that are directly available from the experimental campaign and data that needs to be calculated according to the most common and suitable correlation. Specifically Tsky is calculated by means of correlation from **[3]** already report in tab. 11:

$$T_{sky} = T_{amb}*(0{,}711+ 0{,}0056\ T_{dp} + 0{,}000073\ T_{dp}^{2} + 0{,}013\ \cos(15t)$$

where T_{dp} is the dew point temperature and t is the time (hour of the day from midnight).

tab. 30	Basic input from experimental campaign					Derived input		Checked output	
time [h]	I_{sun} [W m^{-2}]	T_{in} [°C]	T_{amb} [°C]	v_{wind} [m s^{-1}]	mass flow [Kg h^{-1}]	T_{sky} [°C]	h_{wind} [W $K^{-1}m^{-2}$]	T_p [°C]	T_{out} [°C]
13:00	998	33	28	1.8	236	6	7.8	58	46
15:00	869	32	28	1.8	239	7	7.8	54	44
16:00	723	29	25	4.9	226	8	14.7	45	37
17:00	538	28	25	3.6	229	8	12.0	39	34
18:00	319	27	24	3.1	229	8	10.9	31	30

Moreover, considering mass flow is almost constant, mean value is sorted and velocity of fluid [ms^{-1}] is calculated as required by the software. Finally model asks for convective coefficient for heat exchange toward the surrounding external ambient from the cover and bottom surfaces, h_{wind}. During validation phase, outdoors wind speed (v_{wind}) is considered and the h_{wind} values is applied to both boundaries surfaces. Determination of this value is generally difficult and many correlations are available. h_{wind} mainly depends on wind conditions (direction and velocity, in turn influenced by local position) as well as on geometrical features of the interested surfaces. Due to this variability of conditions, many correlations are proposed **[3]**. In order to obtain a reasonable value some of them are compared for sorting the h_{wind}. Specifically, they have been evaluated:

- the Sparrow correlation as proposed by Pohlhausen, based on wind tunnel studies,
- the McAdams correlation as proposed by Watmuff, based on 0.5m^2 surface tests,
- the Mitchell correlation for flush-mounted collector.

Considering results are almost comparable (tab. 31) and considering none of these correlation perfectly matches the analysed case, a mean value among the results is supposed to be suitable as input in the model.

tab. 31 h_{wind} comparison among avilable correlation

Pohlhausen:

$$h_{wind} = \frac{N_u k}{D_l} = \frac{(0.86\, Re_{Dh}{}^{1/2} Pr^{1/3})}{D_l} k$$

Watmuff: $h_{wind} = 2.8 + 3v_{wind}$

McAdams: $h_{wind} = \max\left[5, \frac{8.6\, v_{wind}{}^{0.6}}{L^{0.4}}\right]$

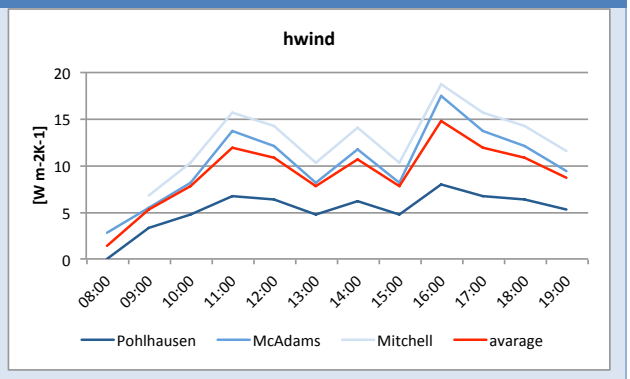

where $D_l = 4area/perimeter$ refering to the collector cover dimensions and $L = \sqrt[3]{building\ volume}$ is the characteristic length of building where the solar collector is installed.

Other necessary inputs regard material properties and are easily sorted by literature and shown in tab. 32. Only radiative properties in the different wavelength bands are not straightly available, as already outlined. It is useful to remember that according to the present FEM model the only needed coefficient are:

- the trasmissivity of glass cover that is applied at the sun source for accounting on optical interaction between solar radiation and cover;
- the emissivity values of cover and plate from which absorption coefficients for all materials and the reflection coefficients for the opaque ones belongs to.

tab. 32 Material Properties – model 1-3

Geometry	κ [W/m^{2}K]	ρ [Kg/m^3]	c_p [J/kg K]	ε [-]		Simulation note
				B1	B2	
Insulation – High density - PUR	0,025	30	1800	-	-	
Absorber plate - Steel	44.5	7850	475	?	?	An equivalent lambda value (λ_{eq} = 200 W/mK) has been introduced considering a fictitious thickness according to mesh design needs.
Air	0,030	0,99	1009	-	-	
Glass – standard	1,40	2200	750	0	0,837	Glass is considered as transparent medium into the visible and near IR band. Moreover, an equivalent lambda value (λ_{eq} = 3,5 W/mK) has been introduced.

B1:band 1; B2:band 2; UNI 12524/2001 "Building materials and products-Hygrothermal properties-Tabulated design values" for thermodynamically properties; "Optics" software by LBNL for glass radiative properties.

Specifically, the τ_{tot} coefficient for glass is calculated introducing the absorption τ_a coefficient accounting on absorption phenomena by the glass and the reflection τ_t coefficient depending on reflection phenomena toward the external ambient and changing according to the incident angle:

$$\tau_{tot} = \tau_t \tau_a = \left[\frac{1}{2}\left(\tau_{per} + \tau_{par}\right)\right]\left(e^{\frac{Kd}{\cos \vartheta_2}}\right)$$

where τ_{per} and τ_{par} are respectively the perpendicular and parallel components of the unpolarised radiation as reported in chapter 3, K [m^{-1}] is the extinction coefficient for standard glass, d is the cover thickness and θ_2 the refraction angle. During validation-calibration phase, the τ_{tot} for single-glass cover is evaluated sorting the incident angle θ_1 in the chosen day and for the tilted surface located in Palermo, results are shown in ***Fig. 45*** while typical emissivity value in the second band is considered for glass. These values are introduced in the model for finding out the effective irradiation reaching the surface and entering the physical system as a net value with respect of reflection/absorption losses by the glass.

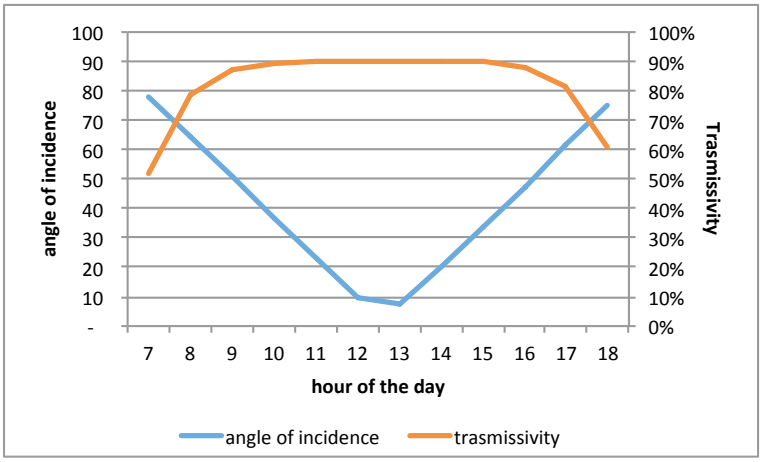

Fig. 45 Trasmissivity and incident angle for the tilted surface during the tested day in Palermo

The remaining coefficients to talk about are the emissivity of the absorber plate and the convective coefficient at the channel walls, the ones that are subject to calibration procedure. According to the way the FEM model is built up, first and second modules were assessed calibrating the plate emissivity in the two wavelength bands with respect to

recorded data. One consideration has been done previously: the only fact known is the colour sensation. Hence, it is possible to narrow the field of investigation starting from that point. Some reflectance spectra belonging to Synnefa et al. [55] and having similar colour sensation of the analysed absorber plate, are introduced and mean value sorted in B1 as $|\varepsilon = \alpha = 1 - \rho|_{0-2500\lambda}$, see tab. 33. For each colour two spectra are available: standard (with s_ prefix) one and cooling ones (with c_ prefix). Model is then run several times fixing one at time the ε_{B1} in the range of 0.6 to 0.9 while changing the ε_{B2}. Each ratio between the sorted temperature by simulation (T_{out}) and the recorded temperature (T_{rec}) is then correlated to the correspondent ε_{B2} and curve trends are introduced by 2nd order approximation. In this way, single value of ε_{B2} for which $T_{out,comsol}/T_{out,rec}$ is found out for any fixed ε_{B1} and results leading to an almost unitary ratio is considered as valid. The interception between the 2nd order curve and the y=1 axis is usable for determining the ε_{B1} to be introduced in the final model.

tab. 33 Reflectance spectra, colour sensation and emissivity value in B1

colour	R	G	B		e_{B1}
s_brown	142	91	76		0,78
c_brown	136	84	70		0,61
s_chocolate	114	79	66		0,91
c_chocolate	107	69	64		0,70
s_lightbrown	153	103	67		0,80
c_lightbrown	155	102	58		0,60

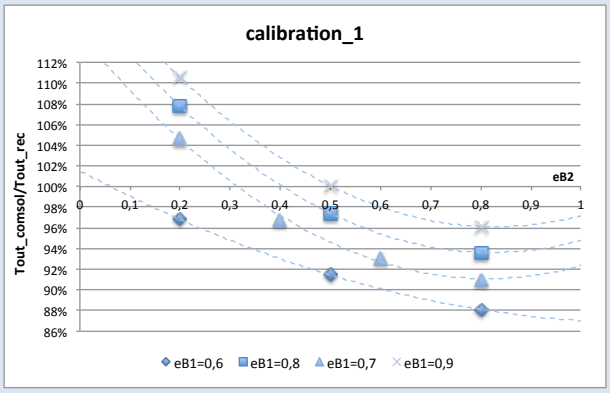

At a first sight, curve for ε_{B1}=0.6 involves the less realistic solution intercepting the y=1 axis at x=0,06 while solution for ε_{B1}=0.7 and ε_{B1}=0.8 curves are pretty fine but requires an ε_{B2} about 0.30-0.40 that are typical for low-emitting surface, what the plate surface is not, and anywayout of the field of interest for the present work aiming to obtain a low-cost prototype. Finally curve for ε_{B1}=0.9 is the best and suitable solution, obtaining $T_{out}/T_{rec} = 1$ at ε_{B2}=0.5.

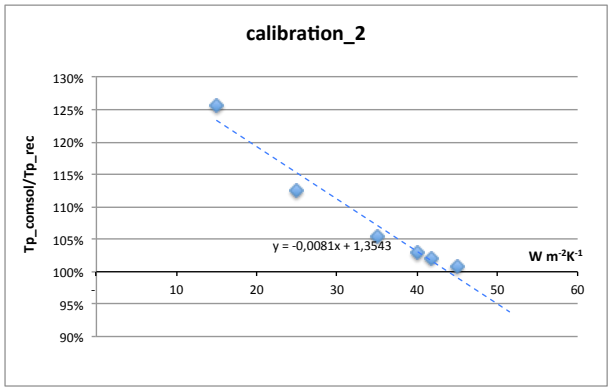

Fig. 46 h-channel calibration according to recorded data.

Once the emissivity coefficients for absorber plate have been determined, module 3 is run for sorting the $h_{channel}$ value, ***Fig. 46***. Once again model is run several time changing h value from 15 to 35 $Wm^{-2}K^{-1}$ and a 1st order fitting curve drown in order to find the suitable intersection with y=1 axis. Procedure is repeated until the condition $T_{p,comsol}/T_{p,rec} = 1 \pm 0.05$ is achieved at $h_{channel}$ = 45 $Wm^{-2}K^{-1}$.

Results of calibrations are then validated running the whole model while changing weather data and inlet temperature inputs in order to validate it at different irradiation conditions: I_{sun}=1000, 870, 720, 540 and 320 Wm^{-2}. Comparison between data belong to the experimental campaign and results from the software shows a good resolution with percentage error between sorted temperature and recorded temperature laying in the chosen range of 5%.

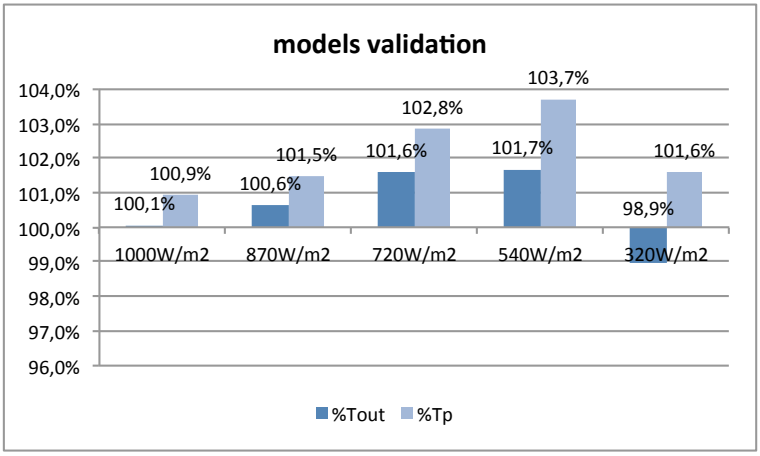

Fig. 47 models validation at different irradiation values.

Prototype B

Following same procedure for Prototype A, Prototype B model is calibrated and validating according to the data from the experimental campaign underwent in summer 2011, see tab. 34. In this case, Tsky values from **[3]** for clear sky conditions are considered as well as h_{wind}=9 $Wm^{-2}k^{-1}$ introduced, corresponding these values to the suitable wind speed and irradiation condition for testing solar collector.

tab. 34	Basic input from experimental campaign					Derived input		Checked output	
time [h]	I_{sun} [W m^{-2}]	T_{in} [°C]	T_{amb} [°C]	v_{wind} [m s^{-1}]	mass flow [Kg h^{-1}]	T_{sky} [°C]	h_{wind} [W $K^{-1}m^{-2}$]	T_p [°C]	T_{out} [°C]
13:40	970	40,0	32,7	-	162	5	9	-	58,4
13:00	900	40,0	37,7	-	114	5	9	-	66,5
11:00	740	24,8	27,5	-	160	5	9	-	43,6
12:00	630	35,2	33,1	-	103	5	9	-	55,1

Essentially material properties are those reported in tab. 32 for prototype A except for the TiNOX absorber plate whose radiative characteristics are available from manufacturer: the emissivity for B2 is equal to 0.04 while the absorption in B1 is 0.96 while for specific heat, thermal conductivity and density data refer to the aluminium substrate taken from literature: k=160 $W(mK)^{-1}$, ρ=2800 kg m^{-3} and cp=880 $J(kg\ K)^{-1}$ **[25]**.

Moreover regarding the bottom plate radiative characteristics, the ones from previous validations are chosen being this element absolutely the same element in configuration A: ε_{B1}=0.9 , ε_{B2}=0.5.

For model B, the unknown value for which calibration takes place is:

- the heat transfer coefficient at the air-gap walls, $h_{air\text{-}gap}$;

- the heat transfer coefficient at the duct walls $h_{channel}$.

Firstly hair-gap is assessed in the way T_{out} from software is comparable with the one from experimental campaign. Differently from previous model, while running models for the different chosen ambient condition, it was not possible to find a unique value respecting the desired condition: $T_{out,comsol}/T_{out,rec} = 1 \pm 0.05$.

Anyway if results for different conditions were considered, it would be notice that the order of magnitude is comparable lying in a range between 10 and 15 $Wm^{-2}K^{-1}$ and similar values are found at the same inflow velocity. Actually, the most common correlation for convective coefficient between two parallel plates at different temperature reports as variable the Rayleigh number influenced in turn by the temperature difference between surfaces themselves and definitively these temperature are in the examined physical system related to the inflow velocity, especially in the case of TiNOX layer and consequently for all other T_{node}. For that reason such a correlation between $h_{air-gap}$ and v_{in} is looked for and proof of this theory searched introducing auxiliary external conditions at different v_{in}, tab. 35. Unlikely, the minimum inlet flow velocity in the experimental campaign is v_{in}= 0,5 ms^{-1} consequently model for m=0.01 $m^3m^{-2}s^{-1}$ cannot be directly validated.

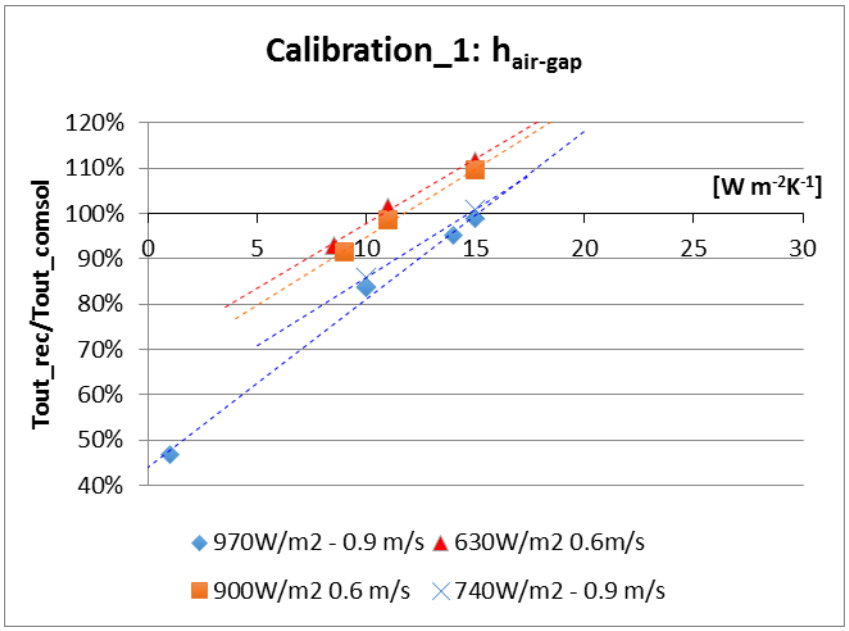

Fig. 48 *Model calibration according to $h_{air-gap}$ for different ambient conditions.*

Results of $h_{air-gap}$ with respect to v_{in}=0,9 ms^{-1} and v_{in}=0,6 ms^{-1} are plotted and a linear correlation sorted in the form of:

$$h_{air-gap} = Av_{in} + B$$

tab. 35	Basic input from experimental campaign					Derived input		Checked output	
time [h]	I_{sun} [W m^{-2}]	T_{in} [°C]	T_{amb} [°C]	v_{wind} [m s^{-1}]	mass flow [Kg h^{-1}]	T_{sky} [°C]	h_{wind} [W $K^{-1}m^{-2}$]	T_p [°C]	T_{out} [°C]
11.20	810	45,0	29,4	-	151	5	9	-	56,9
10.45	769	40,0	33,5	-	94	5	9	-	60,2
13.10	915	45,0	34,9		178	5	9	-	61,0

Model runs then at v_{in}=1,0 ms^{-1} and v_{in}=0,5 ms^{-1} considering the sorted $h_{air-gap}$ by the previous formula and results used for improving the correlation resolution (**Fig. 49**).

As supposed the new sorted v_{in}-$h_{air-gap}$ lies in the sorted lines so that A and B coefficient in previous formula are definitively sorted.

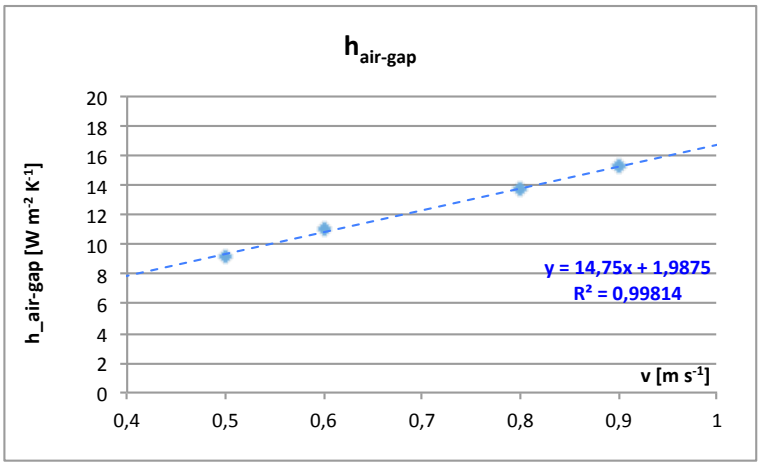

Fig. 49 Correlation between inflow velocity and $h_{air-gap}$

Finally, results of simulations in terms of $T_{out,comsol}/T_{out,\,rec}$ are considered in function of the inlet velocity (***Fig. 50***) and a good reliability for the model detected inducing to think that it could be considered as valid also in the case of m=0.01 $m^3m^{-2}s^{-1}$. Indeed, deviation from the recorded data always lies under the 3% and it is worth to notice that validation took place for different inflow velocity as well and at different irradiation power without any correlation between them: comparable irradiation level were run at different inlet velocity leading to a good reliability of the model.

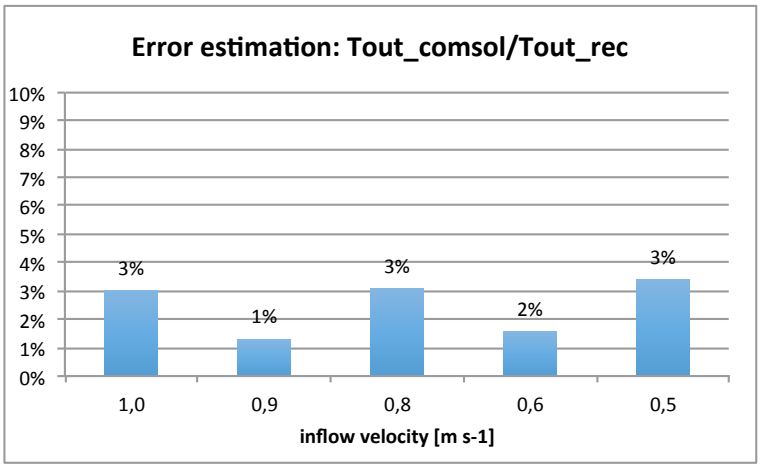

Fig. 50 Reliability of the model in function of the inlet flow velocity

Summery: reliability of FEM models

Present chapter represents the focal point of the whole work since all final results are related to the reliability of FEM model. Validation with respect to recorded data for prototype is of particular significance also for STC-wall simulation since physics does not effectively change from prototype to the integrated solar collector respecting boundary conditions while changing only input value. For that reason it is interesting to outline the main validation results for both prototypes A and B stressing attention on the fact that error estimation always lying in the desired range of -5%<err<+5%. Specifically, it was necessary to consider different input reference parameter in Prototype A and B validation according to their physics and to the available data (tab. 36).

tab. 36 realibility of model with respect to recorded data		T_{out}	T_p
prototype A	I_{sun}=1000 Wm^{-2}	-0.1%	-0.9%
	I_{sun}=870 Wm^{-2}	-0.6%	-1.5%
	I_{sun}=720 Wm^{-2}	-1.6%	-2.8%
	I_{sun}=540 Wm^{-2}	-1.7%	-3.7%
	I_{sun}=320 Wm^{-2}	+1.1%	+1.6%
prototype B	v_{in}= 1.0 ms^{-1}	+3.0%	-
	v_{in}= 0.9 ms^{-1}	+1.0%	-
	v_{in}= 0.8 ms^{-1}	+3.0%	-
	v_{in}= 0.6 ms^{-1}	+2.0%	-
	v_{in}= 0.5 ms^{-1}	+3.0%	-

Moreover, validation took place for T_{out} and T_p with respect to prototype A while only the outlet temperature could be checked for prototype B due to the lack of information, even that this allows to look for the efficiency curve in next chapter.

Finally, also the accuracy of sorted T_{out} is verified looking for the best way for processed output data in order to obtain a reliable T_{out} with respect to the model. The appropriate distance where putting a cut-line for sorting fluid temperature at the exit of duct is detected as well as the way to find out an unique value that well represent the exit temperature at the different inflow velocities. From that point of view results for prototype A are directly applicable to the corresponding STC-wall as well results for configuration B find immediately their correspondence (tab. 37).

tab. 37 fluid domain model: T_{out} accuracy

prototype A ; STC-wall A	0.01 [$m^3\ m^{-2}s^{-1}$]	0.14 [ms^{-1}]	0.69 K
	0.03 [$m^3\ m^{-2}s^{-1}$]	0.41 [ms^{-1}]	1.05K
	0.05 [$m^3\ m^{-2}s^{-1}$]	0.69 [ms^{-1}]	1.11K
prototype B ; STC-wall B	0.01 [$m^3\ m^{-2}s^{-1}$]	0.24 [ms^{-1}]	0.01K
	0.03 [$m^3\ m^{-2}s^{-1}$]	0.73 [ms^{-1}]	0.01K
	0.05 [$m^3\ m^{-2}s^{-1}$]	1.22 [ms^{-1}]	0.01K

5. APPLICATION TO REFERENCE CASES AND DISCUSSION

Considering the validated models for prototype A and B, models for STC-wall A and B are defined and all the four models run according to the standard prescription and consequently method presented in chapter 3. Efficiency curves are sorted at the different volumetric specific flow rate and compared each other in order to outline similarities and differences. Finally useful energy production over a typical year is evaluated in each case and outcomes related each other's.

5.1 STC-wall FEM model

STC-wall models differ mainly from a constructive point of view integrating the wall layer on the back (***Fig. 51***) while from a physical point and from the FEM-model points of view they are essentially the same to the corresponding prototypes, as already outlined. Actually the internal radiative exchange features as well as the internal convective boundary system is identical from prototype to STC-wall, while the external boundaries uses the same formula although introducing different values on the back boundary fronting the indoor ambient. Specifically, radiative exchange with sky and convective effects by wind on upper boundary as well as symmetry and open boundary conditions at front and sides are introduced; meanwhile on bottom and upper side $-\boldsymbol{n}\,(-k\,\nabla\,T) = h(T_{ext} - T)$ is applied and software reads:

- on the upper boundary facing outdoor ambient, h=9 $Wm^{-2}k^{-1}$ belonging to correlation to wind speed at a proper velocity for testing collector and $T_{ext}=T_{outdoor}$

- on the bottom boundary facing indoor ambient, h=1/0.13 $Wm^{-2}k^{-1}$ belonging to UNI EN ISO 6946 **[24**] and including radiative and convective resistances while $T_{ext}=T_{indoor}$

Finally, it is worth to notice that for the air-gap a solid element is introduced and values from UNI EN ISO 6946 regarding equivalent resistance for air-gap in function of its thicknesses introduced.

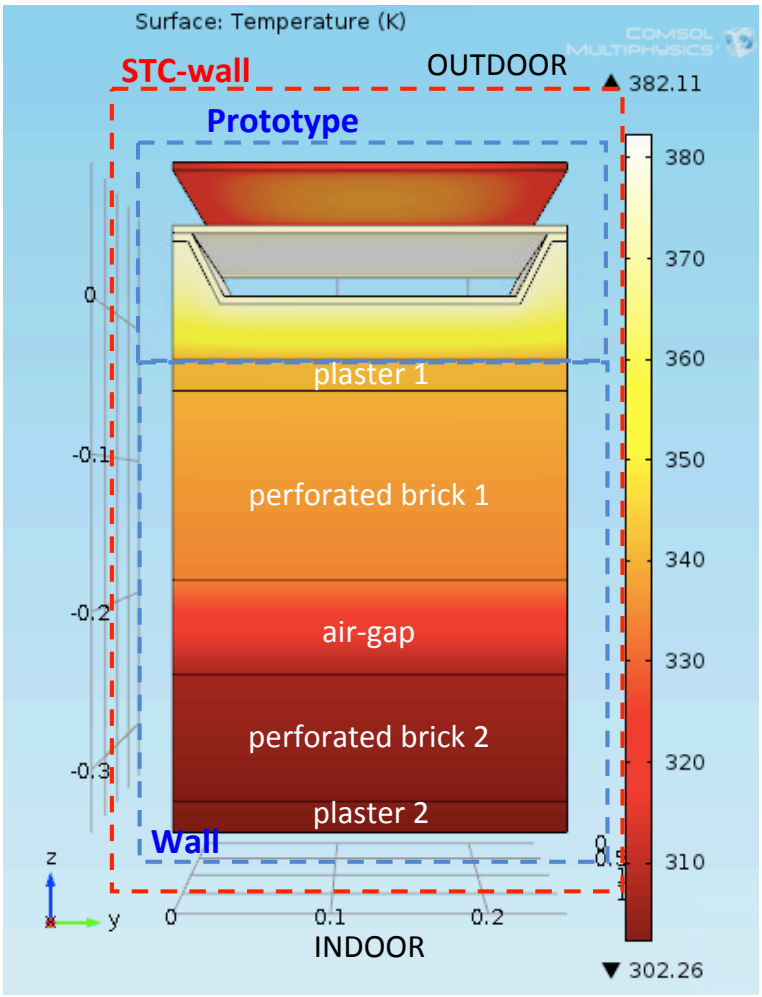

Fig. 51 Comsol model for STC-wall and main features of the component, results refers to model 1 run at 630 W/m².

Efficiency curve calculation and prototype/STC-wall outlines.

Applying prescriptions from the regulations to the four models, efficiency curve for prototypes and for STC-walls are sorted using a 2nd order fitting whenever possible. Briefly, simulations run according to tab. 38 where specifically, T_{amb} for the prototypes is the outdoor air temperature, while for STC-walls is the average weighted outdoor/indoor temperature as already defined in chapter 3.4:

$$T_{amb,w} = \frac{T_{outdoor}U_{top} + T_{indoor}U_{back}}{U_{top} + U_{back}}$$

tab. 38 input	$T_{in} = T_{amb}$	$T_{in} = T_{amb} \pm 5°C$	$T_{in,(n)} = T_{out,(n-1)}$
m= 0.01 [$m^3\ m^{-2}s^{-1}$]	$x = \frac{(T_{in} - T_{amb})}{I_{sun}}$; $y = \frac{m\ c_p(T_{in} - T_{amb})}{A_{coll} I_{sun}}$		
m= 0.03 [$m^3\ m^{-2}s^{-1}$]			
m= 0.05 [$m^3\ m^{-2}s^{-1}$]	$x^* = \frac{(T_m^* - T_{amb})}{I_{sun}}$; $y^* = \frac{m\ c_p(T_m^* - T_{amb})}{A_{coll} I_{sun}}$		

As a result an efficiency curve discharging the quadratic term assumes the form of:

$$\eta = \eta_0 - a\ x$$

$$y = \eta_0 = F_R(\tau\alpha) \qquad a = F_R U_L \qquad x = \frac{\Delta T}{I_{sun}}$$

Consequently, from an overall point of view and for making comparisons between prototypes, between STC-walls and among prototypes and STC-walls, the interception with axis is related to the main collector characteristics:

$$y = \eta_0 = 0 \qquad x = \frac{\Delta T}{I_{sun}} = \left|\frac{\eta_0}{a}\right| = \left|\frac{F_R(\tau\alpha)}{F_R U_L}\right| = \left|\frac{(\tau\alpha)}{U_L}\right|$$

$$x = \frac{\Delta T}{I_{sun}} = 0 \qquad \eta = \eta_0 = F_R(\tau\alpha)$$

First of all, it has to be noticed that ($\tau\alpha$) product depending on reciprocal radiative properties of cover and plate changes from Configuration A and Configuration B while no difference could be noticed between prototype and the corresponding STC-wall. It has been firstly evaluated according to formula in tab. 10:

$$(\tau\alpha) = \frac{\tau\ \alpha}{1 - (1 - \alpha)\rho_d}$$

- τ is the transmittance of the cover system depending on the incident angle;
- α is angular absorptance of the absorber plate;
- $\rho_d = \tau_a(1 - \tau_r) = \tau_a - \tau$ is reflectance of the cover system for diffuse radiation incident

becoming from the bottom side and depending on the overall transmission coefficient and on the transmission coefficient related to absorption phenomena by Beer's law (**tab. 8**). Generalising and considering the incident angle varying from 0 to 90°, calculation of ($\tau\alpha$) have been done for the two configuration and results shown in ***Fig. 52***. According to reciprocal ratio between outcomes for configuration A and B is considered and a constant reduction of 5% between the two analysed system recorded:

$$\frac{(\tau\alpha)_A}{(\tau\alpha)_B} = 95\%$$

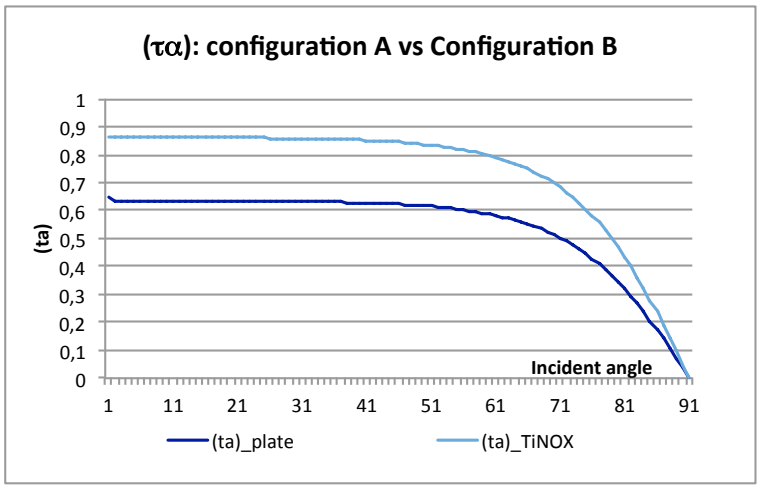

Fig. 52 (ta) product depending on incident angle for configuration A and configuraiton B.

Moreover comparing prototypes with the corresponding STC-walls the main difference is the U_L value and their thermal capacity Cc since, as aim of present work, the wall layer are included in the calculations. Specifically, considering the top configuration as well as the edge construction and the wall-integration technique in ***Fig. 24***, only back structure change in the reason the wall is considered as a part of the collector itself. It follows that main difference in U_L is in the value of $U_{b,prototype}$ and $U_{b,STC}$. Evaluating then this value for the prototype and for the STC-wall a reduction about 40% is recorded between the solar collector and the integrated one, **Fig. 53**.

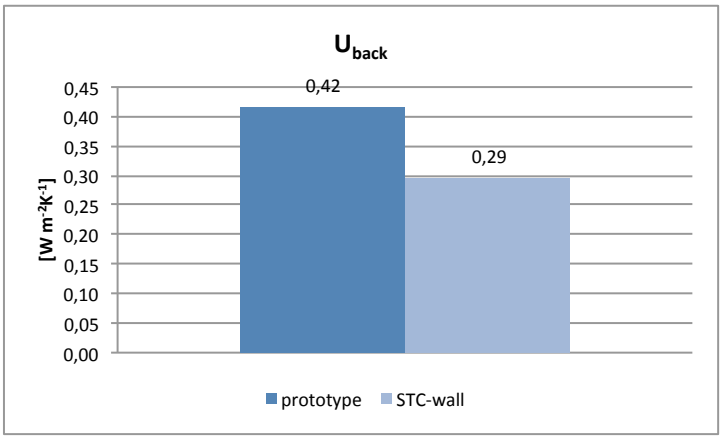

Fig. 53 back trasmittance comparison between prototypes and STC-walls.

Moreover, the STC-wall and collector capacity are evaluated and compared according to:

$$Cc = \sum_{i}^{n} p_i m_i c_i$$

where m is the mass of each *i* layer composing the analysed element, c its specific heat a p a weighting factor whose values varies according to EN 12975 from 1 for the absorber and liquid (this regulation refers to liquid solar collector) to 0,5 for insulation. These values, that are introduced by the regulation in order to account on the way each element participate at the thermal inertia of the component, have been adapted to the specific analysis of an air integrated solar collector, considering for solid element with high density p=1 and for insulation p=0.5, as rule did; while for air p is set a 0.5, too. Results are shown in ***Fig. 54*** and totally different order of magnitude is recorded between STC-wall and prototypes, as expected considering the wall layers in calculation.

thermal capacity	p [-]	ρ [kg m-3]	cp [J (kgK)-1]	s [m]	volume [m3]	
absorber	1	7850	475		0,0021	7.830,38
insulation	0,5	30	1800		0,105	2.835,00
fluid-channel	0,5	1	1009		0,147	74,16
glazing	0,01	2200	750		0,0012915	21,31
brick	1	775	837	0,2	0,572	371.042,10
plaster	1	1800	837	0,02	0,0572	86.177,52
air gap	0,5	1	1009	0,06	0,1716	86,57
ST-wall THERMAL CAPACITY					**kJ/K**	**468**
COLLECTOR THERMAL CAPACITY					**kJ/K**	**11**

Fig. 54 STC-wall and prototype thermal capacity comparison.

5.2 Prototypes efficiency curves

Fig. 55 compares performances for prototype A and B at different inflow specific mass flow rate, if interceptions at x-axis and y-axis are considered some interesting notices come.

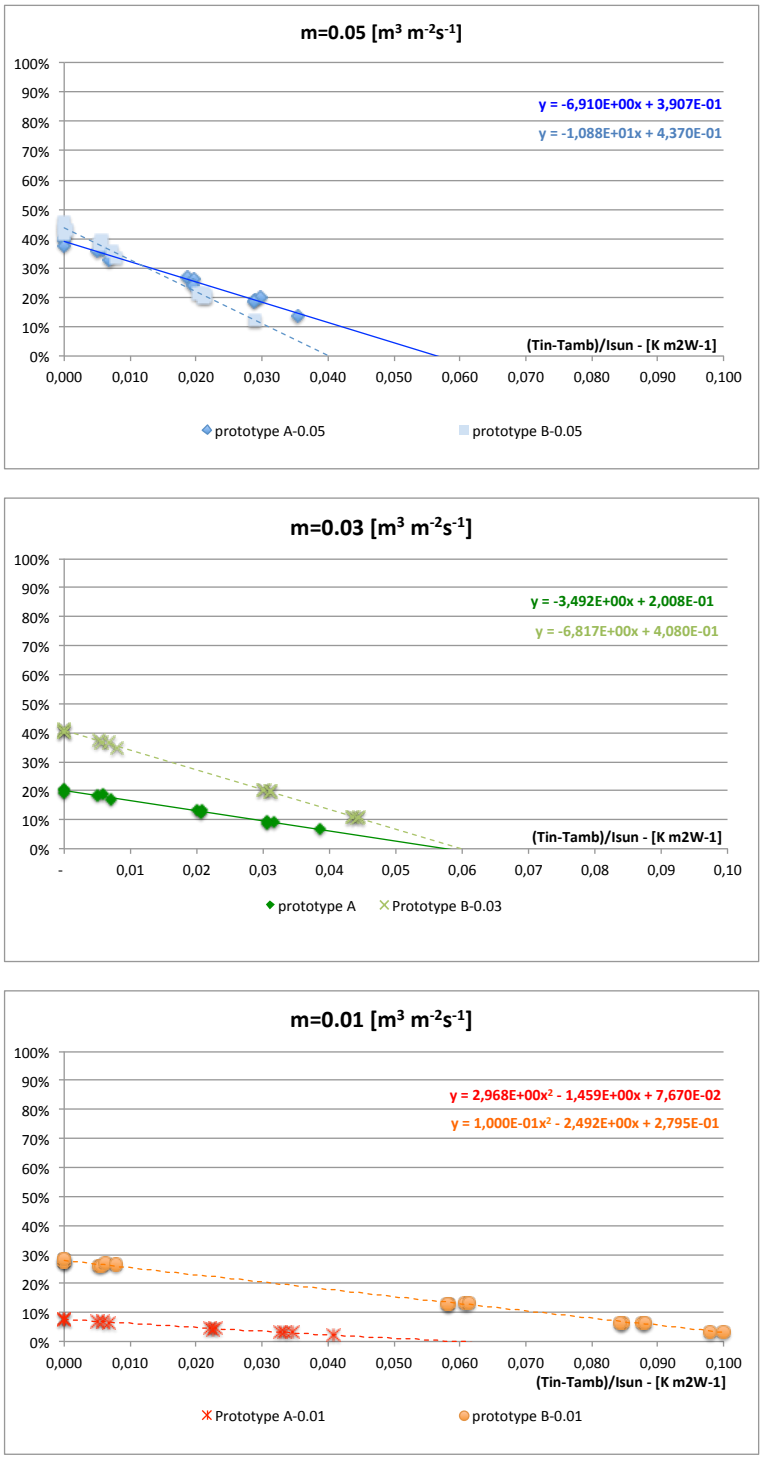

Fig. 55 Efficiency curves for prototype A and B varying the inflow velocity as a function of T_{in}

First of all, the maximum efficiency at x-axis=0 is higher for prototype B as expected, with maximum differences between Prototype A and B recorded for the lowest flow rate while for m=0.05 [m^3 $m^{-2}s^{-1}$] this difference set only at 6%. Moreover mass flow rate reduction extremely affects prototype A maximum efficiency while for prototype B a 3% of maximum efficiency reduction is recorded from m=0.05 to m=0.03 [m^3 $m^{-2}s^{-1}$] and a 12.3% from m=0.03 to m=0.01 [m^3 $m^{-2}s^{-1}$]. Actually, comparing prototypes performance at the same flow rate and remembering $(\tau\alpha)_B$ is 5% higher then $(\tau\alpha)_A$, a reduction about that percentage is obviously between the two configuration for any inflow rate case; moreover, for x=0 it follows that

$$y_{x=0} = F_R(\tau\alpha)$$

being the interception with y-axis driven also by

$$F_R = \frac{\dot{m}\, c_p}{AcU_L}\left(1 - e^{-\frac{AcU_L F\prime}{\dot{m}\, c_p}}\right)$$

and considering c_p, A_C are constant while m varies in the same way from a case to the another in both analyzed configuration and only case at the same flow rate are compared, it is deductible the U_L and F' dependence on temperature is mostly affecting prototype A. Indeed, as suggested by Copper and DunKle in **[3**] a linear dependence could be introduced for these parameters with respect to temperature assuming: $U_L F' = a + b\,(T - T_{amb})$, where a and b are coefficient depending on wind speed and cover collector structure. Actually, U_L is a function of node temperatures as well as wind speed, with increasing dependence as the number of cover decreases. It is then reasonable to suppose the change in configuration from A to B leading a reduction of such temperature dependence while Prototype A performances are deeply affecting by it.

At this regard, another notice comes if the x-axis interception at the different inflow rate is analyzed. Actually, prototype A efficiency curves intercept this axis in every cases quite at the same point, while for prototype B the interception changes from one case to the other. Being this interception the ratio between $(\tau\alpha)$ and U_L, and if it is almost constant as it is for

prototype A and ($\tau\alpha$) does not vary with the inflow rate, it means also U_L need to be constant inducing to suppose only F' in prototype A is mainly affected by temperature. At least having a look at the duct geometrical characteristics in both prototype different convective coefficient has to be affected, hence remembering the collector efficiency factor depends on geometrical features of the duct and on this coefficient (formula is reported in tab. 10) another reason for why the two groups of efficiency react in so different way while changing the inflow rate could be searched in F'.

Finally, if the x-axis interception for prototype B is considered, such a dependence U_L on temperature is predictable also in this case being the $x_{y=0}$ values extremely variable changing the inflow rate and consequently the thermal behavior and temperature results for the prototype.

5.3 STC-wall efficiency curves

Equation in function of T_{amb} and in function of T_m* are compared introducing both prototype and STC-wall efficiency curves whose representation is shown in ***Fig. 56***, ***Fig. 57*** and ***Fig. 58***. At a first sight, as predictable higher results become when the reduced temperature is introduced while no relevant notice on prototype and corresponding STC-wall behavior is actually recorded. For finding such a difference it is necessary to look at m=0.05 $m^3m^{-2}s^{-1}$ and specifically at configuration A, where an increase about 1% of maximum efficiency as well as an increase in the x-axis interception in favor of the integrated collector is outlined, ***Fig. 58***.

Indeed, both prototype for their configuration are presumable extremely dependent on the thermal top loss and edge loss coefficient more than on U_{back} as a single cover is provided in both cases while thermal bridge at the perimeter is not enough properly designed in order to reduce its effect in favor of a easy and fast assembling during building renovation work.

At the same time, some betterments in thermal performance for integrated collector could be noticed for the poorest configuration A even if this improvement is not actually significant.

$$x = \frac{(T_{in} - T_{amb})}{I_{sun}}$$

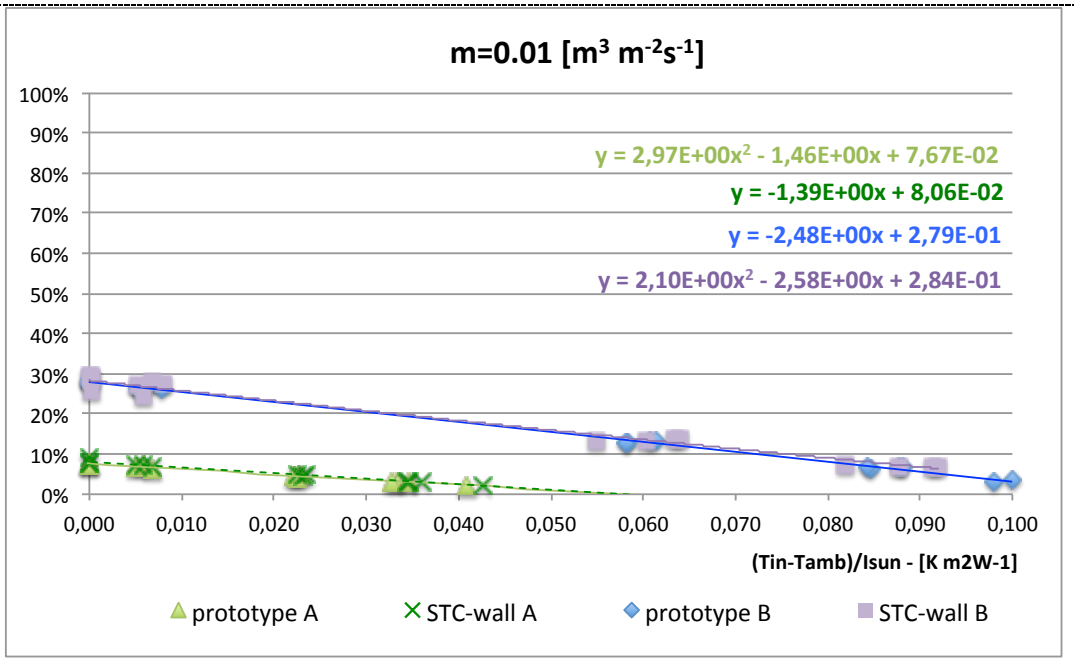

$$x = \frac{(T_m^* - T_{amb})}{I_{sun}}$$

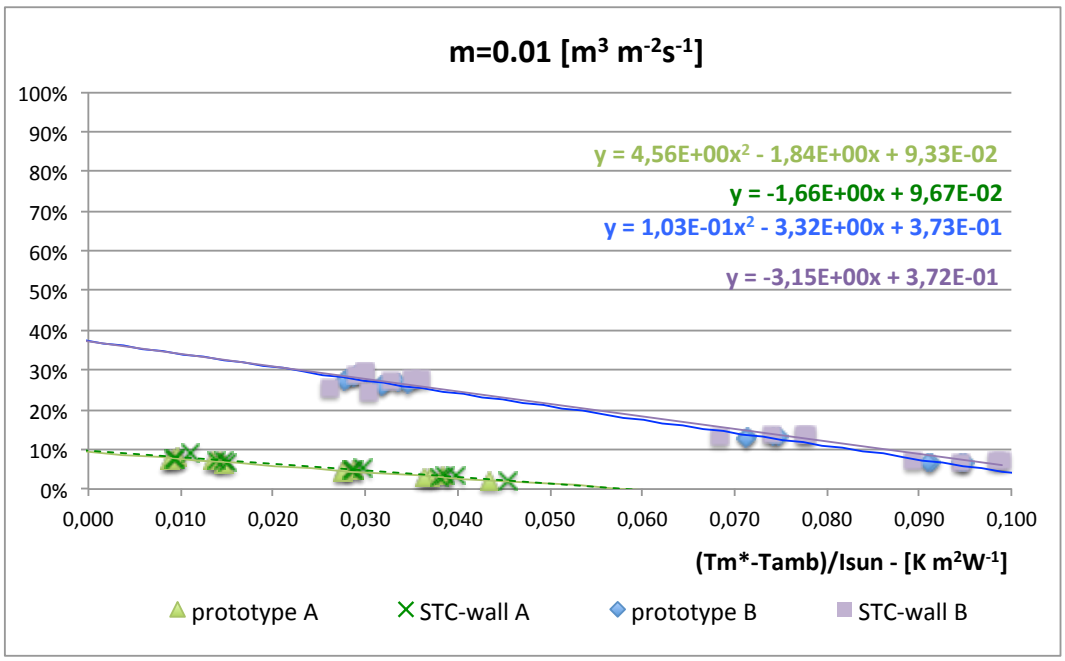

*Fig. 56 Efficiency curve comparison between prototype and STC-wall at m=0.01 $m^3m^{-2}s^{-1}$. Efficiency curve are sorted in funciton of Tin and of the reduced temperature Tm**

$$x = \frac{(T_{in} - T_{amb})}{I_{sun}}$$

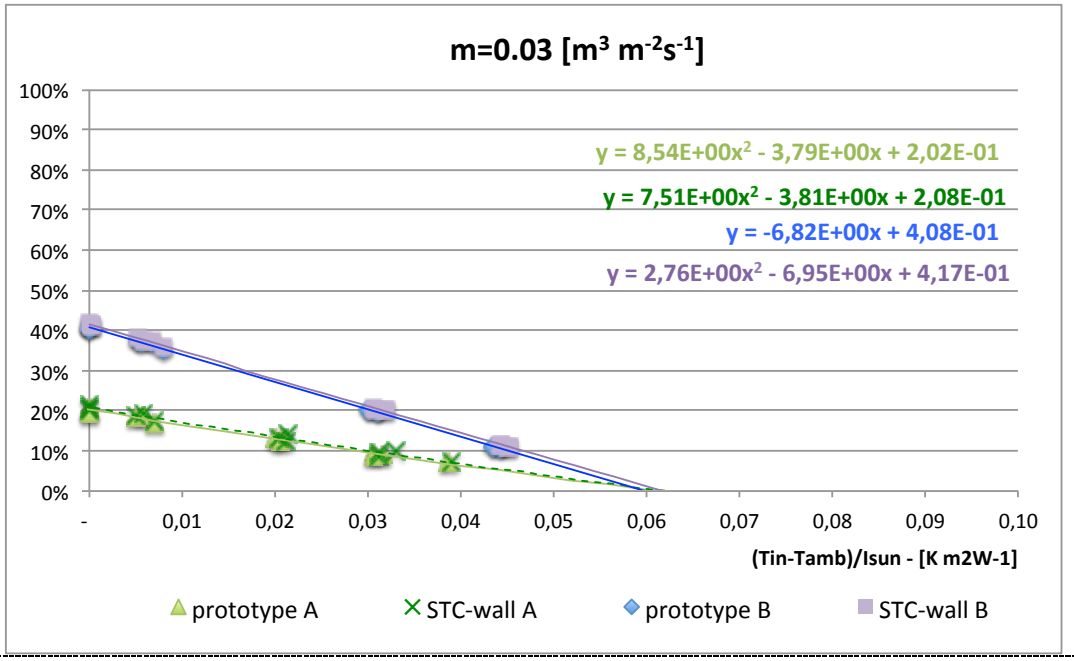

$$x = \frac{(T_m^* - T_{amb})}{I_{sun}}$$

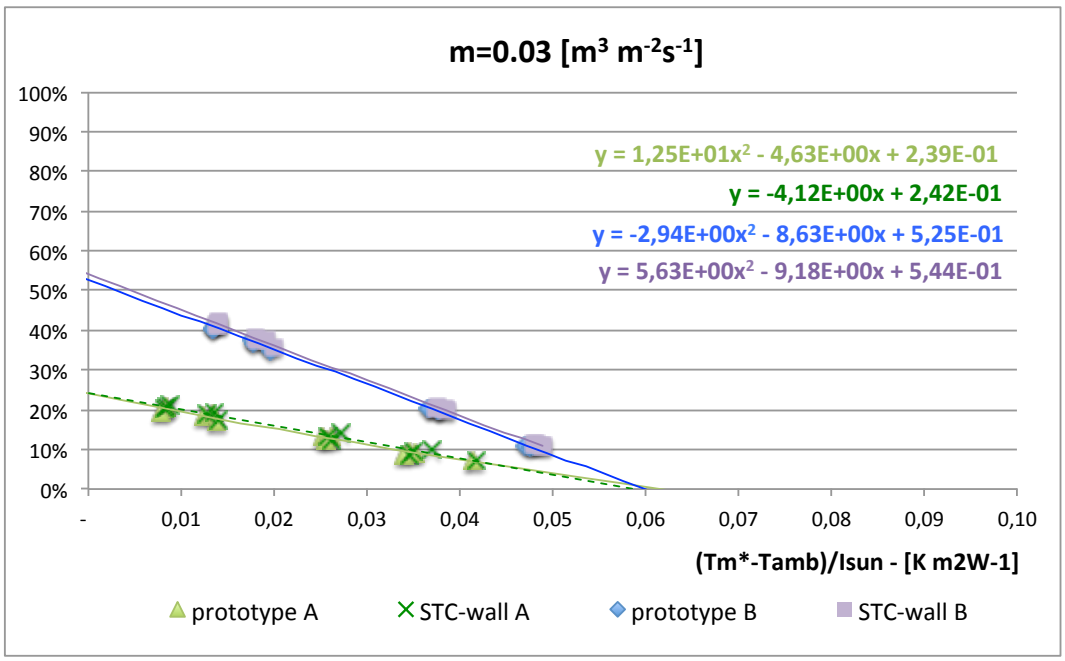

*Fig. 57 Efficiency curve comparison between prototype and STC-wall at m=0.03 $m^3m^{-2}s^{-1}$. Efficiency curve are sorted in funciton of Tin and of the reduced temperature Tm**

$$x = \frac{(T_{in} - T_{amb})}{I_{sun}}$$

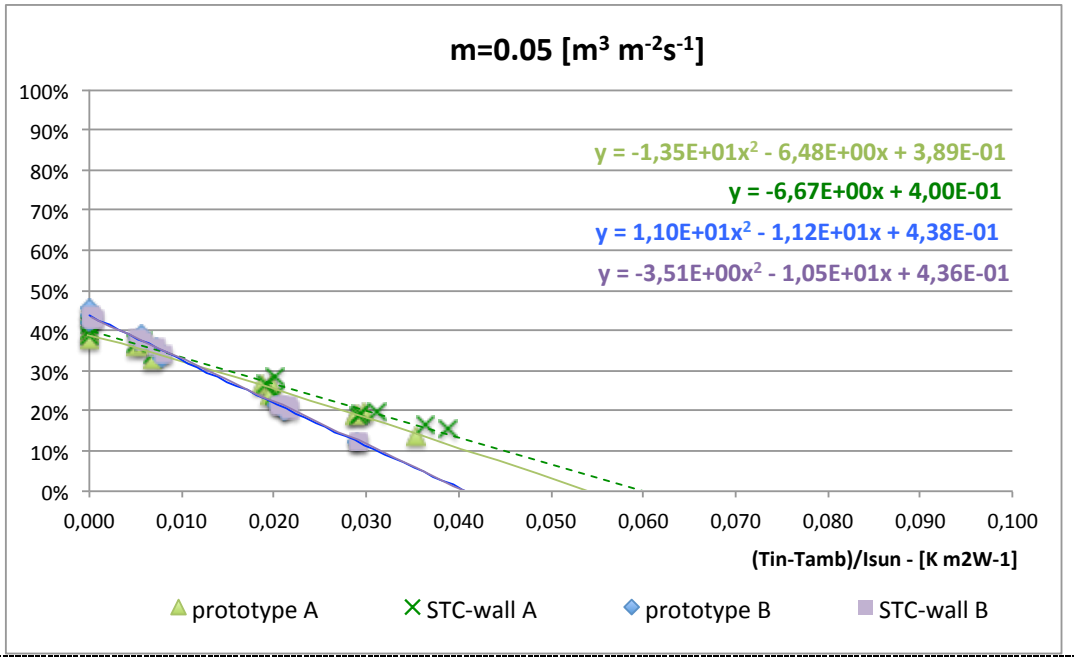

$$x = \frac{(T_m^* - T_{amb})}{I_{sun}}$$

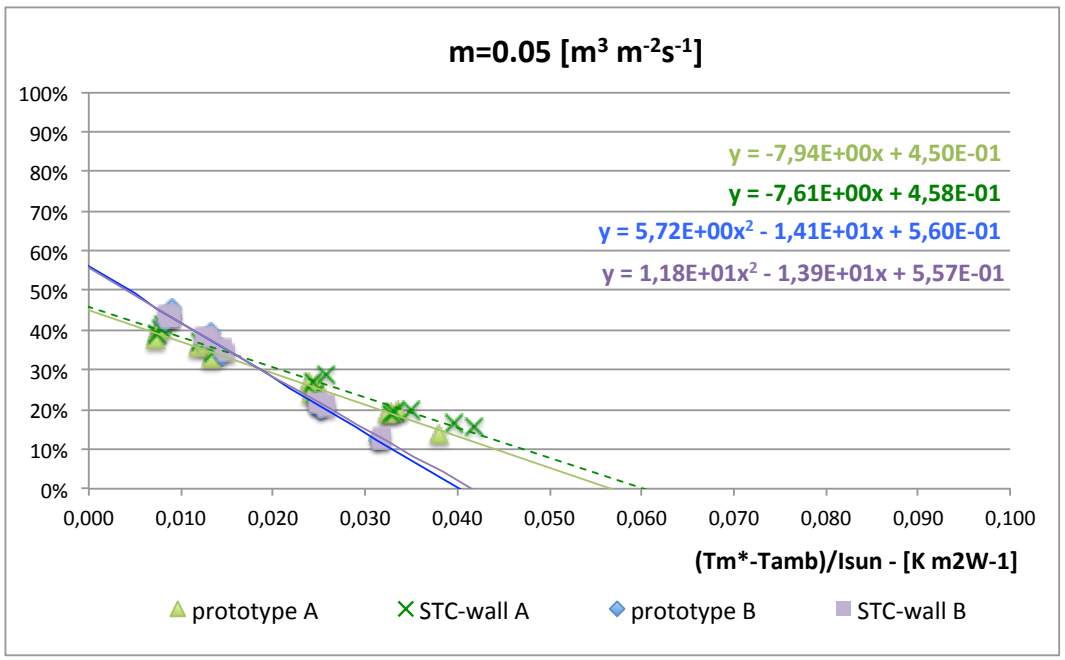

*Fig. 58 Efficiency curve comparison between prototype and STC-wall at m=0.05 $m^3m^{-2}s^{-1}$. Efficiency curve are sorted in funciton of Tin and of the reduced temperature Tm**

5.4 STC-wall transient behaviour

What it is missed right now is the effect of the change in thermal capacity when collector is integrated since right now only steady-state conditions have driven analysis.

For this purpose, a further investigation is performed by means of Trnsys using the efficiency curves as input and energy production over a typical year in a specified sites detected for both prototype and STC-wall in both configurations. Type 539 is suitable for the proposed analysis requiring the efficiency curve coefficient as well as the collector capacity as input and basing results essentially on:

$$C\frac{dT}{dt} = F'\big(I - U_L(T - T_{amb})\big) - \dot{m}c_p(T - T_{in})$$

$$I = (\tau\alpha)_n IAM\ A\ I_{sun}$$

where IAM is set as suggested in D&B at 0.126. All the required input are the obtained by introducing the efficiency curve coefficient ($A = F_R U_L$) and intercepting term ($B = F_R(\tau\alpha)$) with reference to the generic equation: $\eta = Ax + B$ while solving iteratively the following system of equation:

- $(\tau\alpha)_N = \frac{B}{F_R} = \frac{(F_R(\tau\alpha)_N)}{F_R}$
- $U_L = \frac{BA}{F_R} = \frac{(F_R U_L)}{F_R}$
- $F' = -\frac{\dot{m_{test}} Cp_{test}}{AU_L} \ln\left(1 - \frac{F_R A_{coll} U_L}{\dot{m}cp}\right)$
- $F'^{(\tau\alpha)_N} = F' \cdot (\tau\alpha)_N$
- $F'U_L = F' \cdot U_L$

Two sites with different climatic characteristics are proposed: Milan and Palermo and results sorted for m=0.05 and m=0.03 [m^3 $m^{-2}s^{-1}$]. ***Fig. 59*** shows the main climatic characteristic of the chosen sites, Rome is also introduced since it will be used for further analysis in next chapter and data belongs to UNI 10349:1994 **[22]**. Specifically sites mainly differ for degree days value as well as for the duration of the heating period and for the thermal plant design temperature (T_{design}). Moreover different daily average air temperature and global irradiation on south surface change for one city to the other during the winter months.

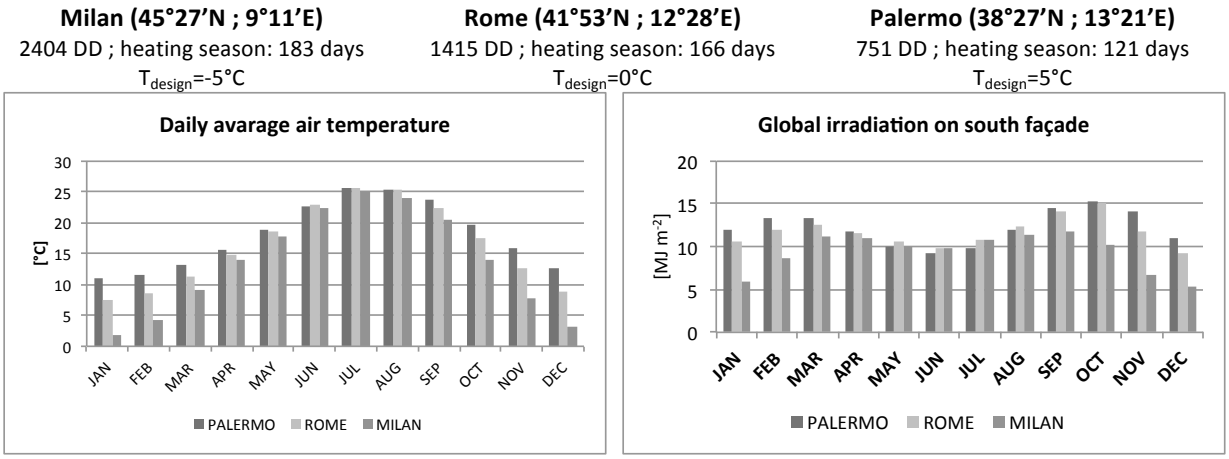

Fig. 59 climatic characteristics of chosen sites

Consequently Trnsys model accounts on a controller regarding heating and cooling season that determines whenever T_{indoor} is 26°C (cooling period) and whenever it is 20° C in order to find out the appropriate $T_{weighted}$ for losses calculation in STC-wall. Results in terms of useful energy production and temperature at outlet are then sorted and compared each other.

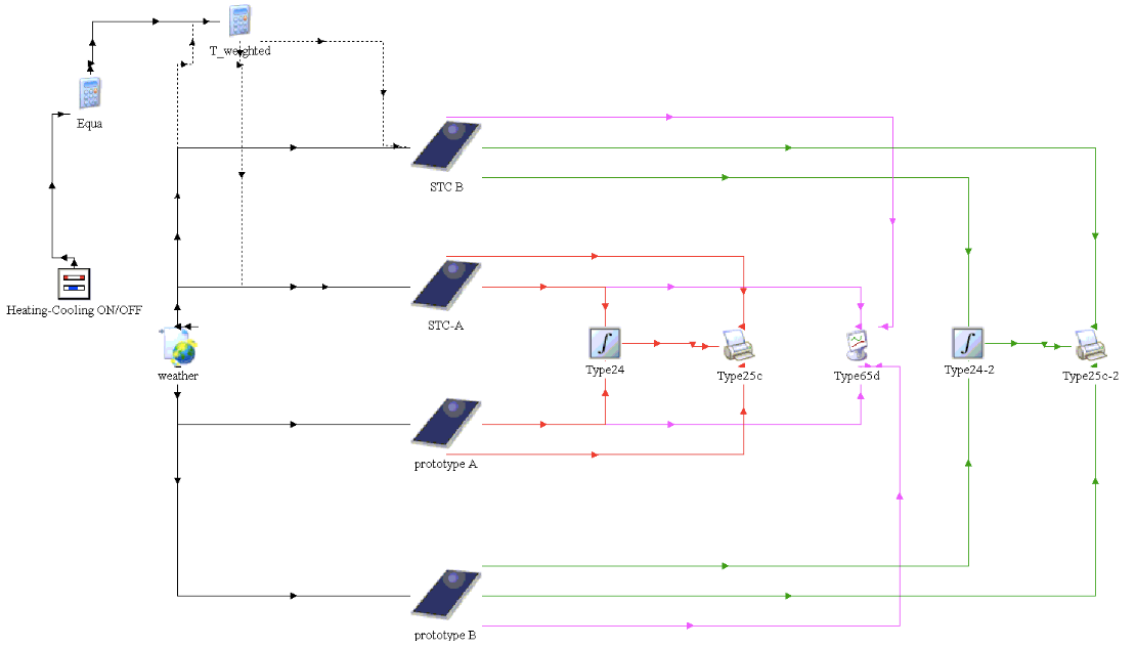

Fig. 60 Trnsys model

Considering the transient behaviour, differences between the STC-walls and the merely prototype are more evident. If outlet temperature difference between STC-wall and prototypes are considered, fluctuations between -10 and +10°C in Milan and between -5 and +5°C in Palermo are evident with positive values recorded during the day and without respect on inlet flow rate.

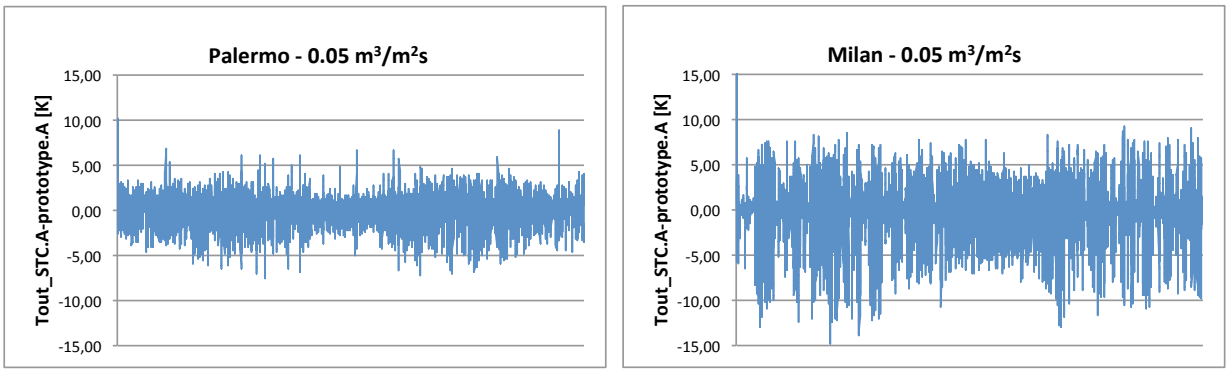

Fig. 61 Typical outlet temperature difference trand between STC-wall and prototype in working condition in Milan and Palermo. Data for maximum inflow rate are reported as reference case.

Fig. 62 shows monthly useful energy production for the city of Milan at different inflow rate, actually whenever the solar collector is integrated higher performances are recorded with major differences for configuration A at m=0.05 $m^3m^{-2}s^{-1}$. If an average yearly value for the $Qu_{STC}/Qu_{prototype}$ is used as reference point for comparison in configuration A energy

production increases about 17% when a 0.05 $m^3m^{-2}s^{-1}$ inflow rate is provided and about 33% if the inlet mass is reduced to 0.03 $m^3m^{-2}s^{-1}$. Meanwhile for configuration B, this production improvements set at 14% and it is not affected by the inflow rate, as already outlined in the comments regarding the comparison among efficiency curves.

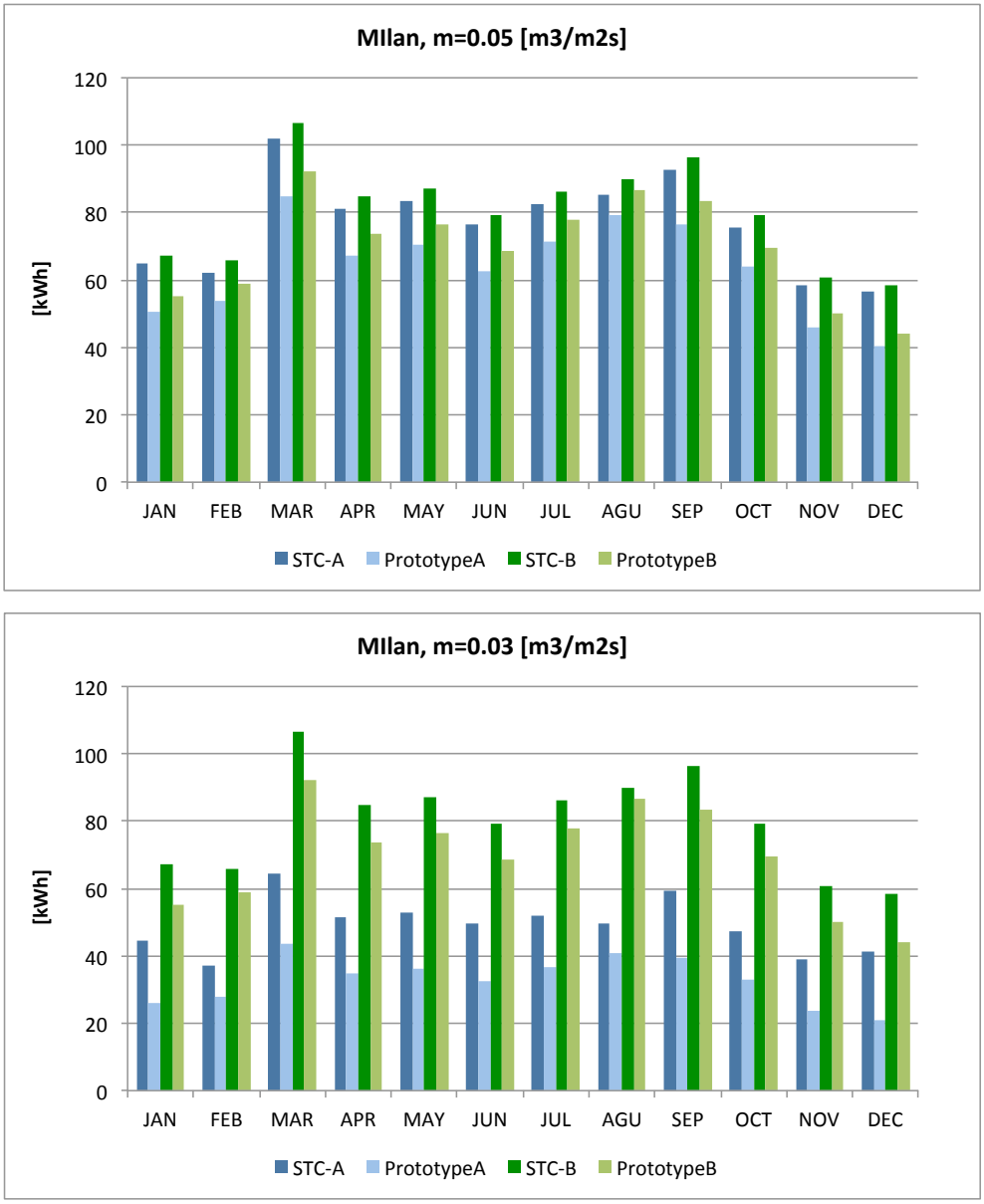

Fig. 62 Useful monthly energy gain in Milan varying the inflow rate: comparison among STC-walls and prototypes

Moreover, if weather conditions change and a warmer climate is considered as in the case of the city of Palermo, others considerations follow (***Fig. 63***). Specifically, meanwhile the yearly average improvement in energy performances between collector and STC-wall for

configuration B doesn't change and stands still at 14% without any respect to inflow velocity; configuration A shows lower value than that recorded for the city of Milan even if the trend between m=0.05 and m=0.03 $m^3m^{-2}s^{-1}$ is confirmed and 7% increment at the highest inflow rate versus 13% corresponding to the minimum inflow rate are recorded.

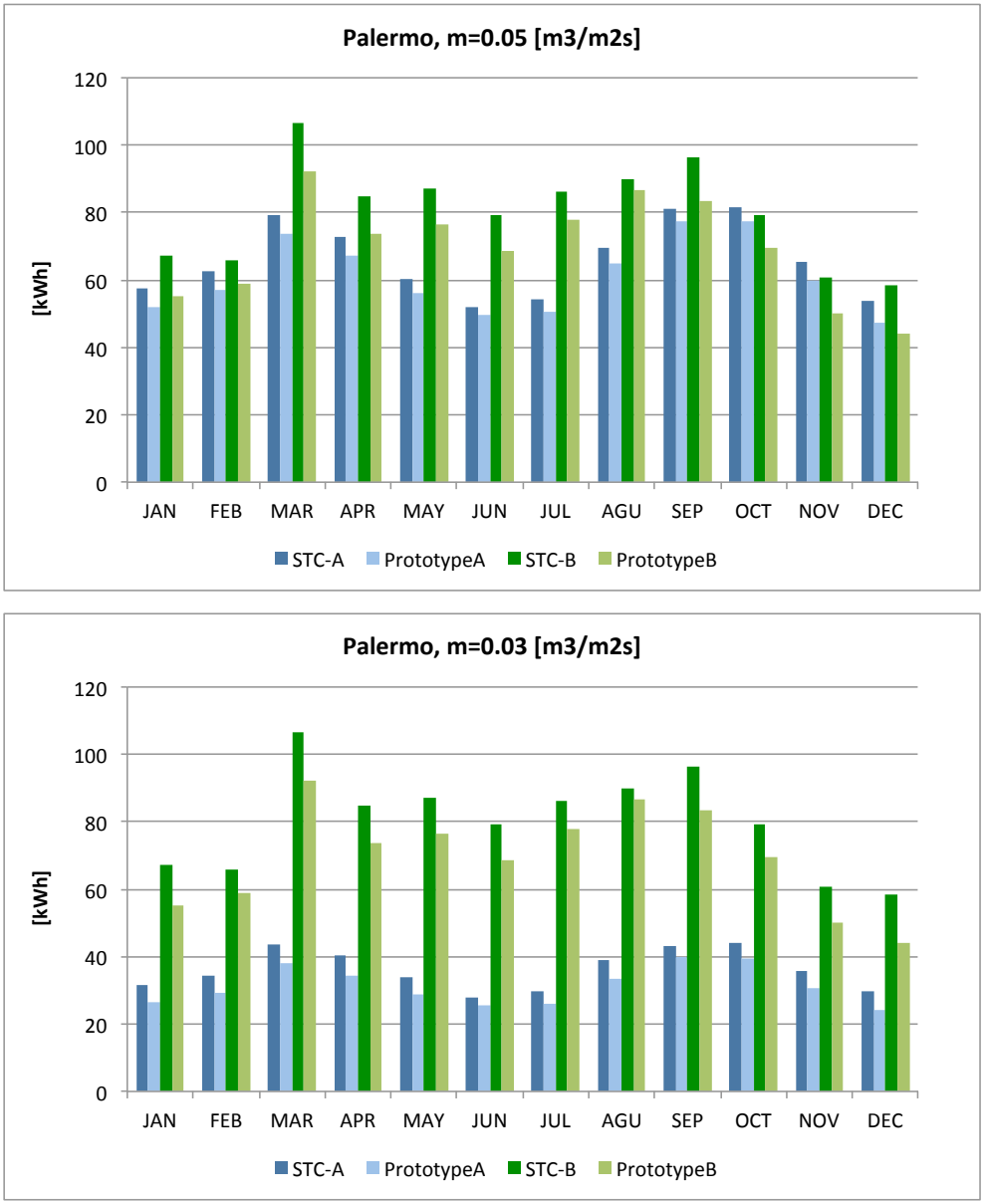

Fig. 63 Useful monthly energy gain in Palermo varying the inflow rate: comparison among STC-walls and prototypes

Summarising the integrated system is more suitable in cold climate overall if medium inflow rate are previewed as standard working conditions. Moreover, a final reasoning could be introduced concerning the opportunity of choosing a specific configuration with regards of the climatic conditions, as obviously configuration B is everywhere desirable but some remark come if the ratio between the useful energy production for STC-wall A and B are sorted in Palermo and in Milan distinguishing the inflow rate, ***Fig. 64***. If the maximum flow rate is considered, both in Milan and in Palermo the two configurations during winter time are quite comparable while if m=0.03 $m^3m^{-2}s^{-1}$ is considered configuration B becomes more suitable all over the year especially in Palermo.

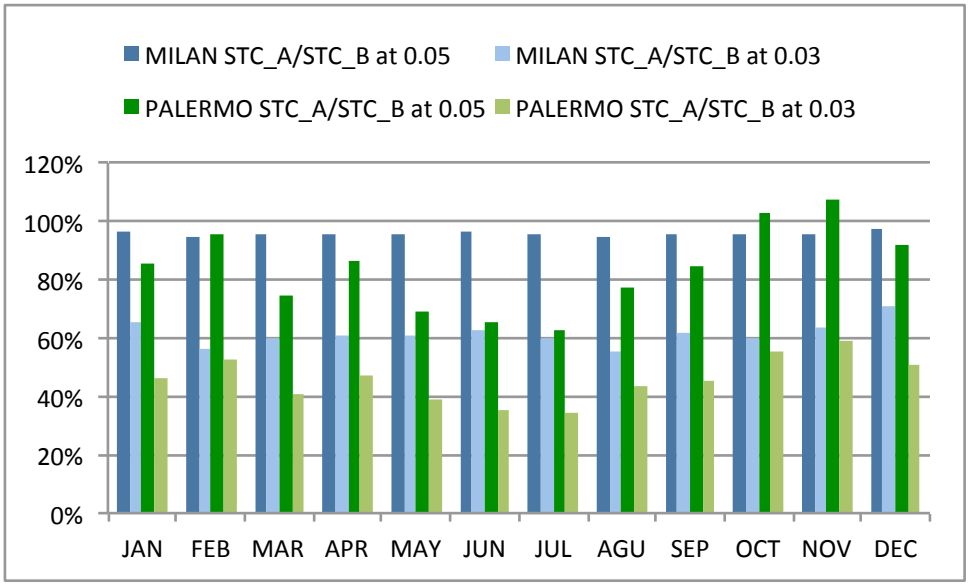

Fig. 64 Ratio between useful energy gain from STC-wall and STC-wall B for the city of Milan and Palermo.

Actually, present results confirm as obviously the predictable results from the efficiency curve analysis outlining from one part the effect of thermal inertia for STC-wall and from other part giving a practical view on the problem while considering specific sites.

6. STUDY OF THE PERFORMANCES IN BUILDING INTEGRATION

Once the efficiency curves for the STC-wall A and B were sorted, Trnsys model is suitable for determining the outlet temperature, the useful energy production and the node temperatures in working condition over a typical year in a specified reference building. It is possible then to relate energy production to the overall building energy balance and to the energy transfer through the south façade.

From this point of view, solar collectors connected in series are supposed to be integrated in the south façade according to its main architectonic features and to provide the required basic air change per hour during the heating season. At the same time, heat exchange through the south wall is supposed to occur between the indoor air temperature and the surface temperature at the interface between solar collector and the wall itself, opportunely determined. Consequently during heating period the modified heat transfer through the wall as well as the modified energy losses by ventilation are considered meanwhile during cooling period when air from the collector is supposed to be discharged only transmission through the south wall is considered.

Moreover, none Trnsys type for glazed air collector requiring as input efficiency curve coefficients, working at different ambient temperature at the back and cover surface boundaries and giving back the desired values is available. For that reason a system of equation is introduced deriving node temperatures from outlet temperature and STC-wall energy balance. ***Fig. 65*** shows the general Trnsys model where the main type are type 56 for simulating the building energy performance and type 539 for simulating the solar collector array. The latter one provides to type 56 itself the main input at building ventilation load level (the outlet temperature is used as input for ventilation energy balance) and at south façade boundary condition level (the evaluated $T_{interface}$ is the boundary condition for heat exchange through the south wall). Weather data belong to the database by the US Department of Energy and Milan is again chosen as reference site being the place to which the reference building presented in next section belong, moreover this previous research results based to the same weather database. In addition and in order to evaluate STC-wall performances, simulations run also for Palermo and Rome, ***Fig. 59***.

Since no plate temperature validation with respect to recorded data for the Comsol© model on Prototype B is available and no check for validating the system of equation in Trnsys© model could be done, only configuration A is analyzed.

Indeed, before running proper simulation, Trnsys model is run at the same steady-state condition of the FEM model for first and $T_{node,Trnsys}$ are compared to the corresponding Comsol© outputs, $T_{node,comsol}$.

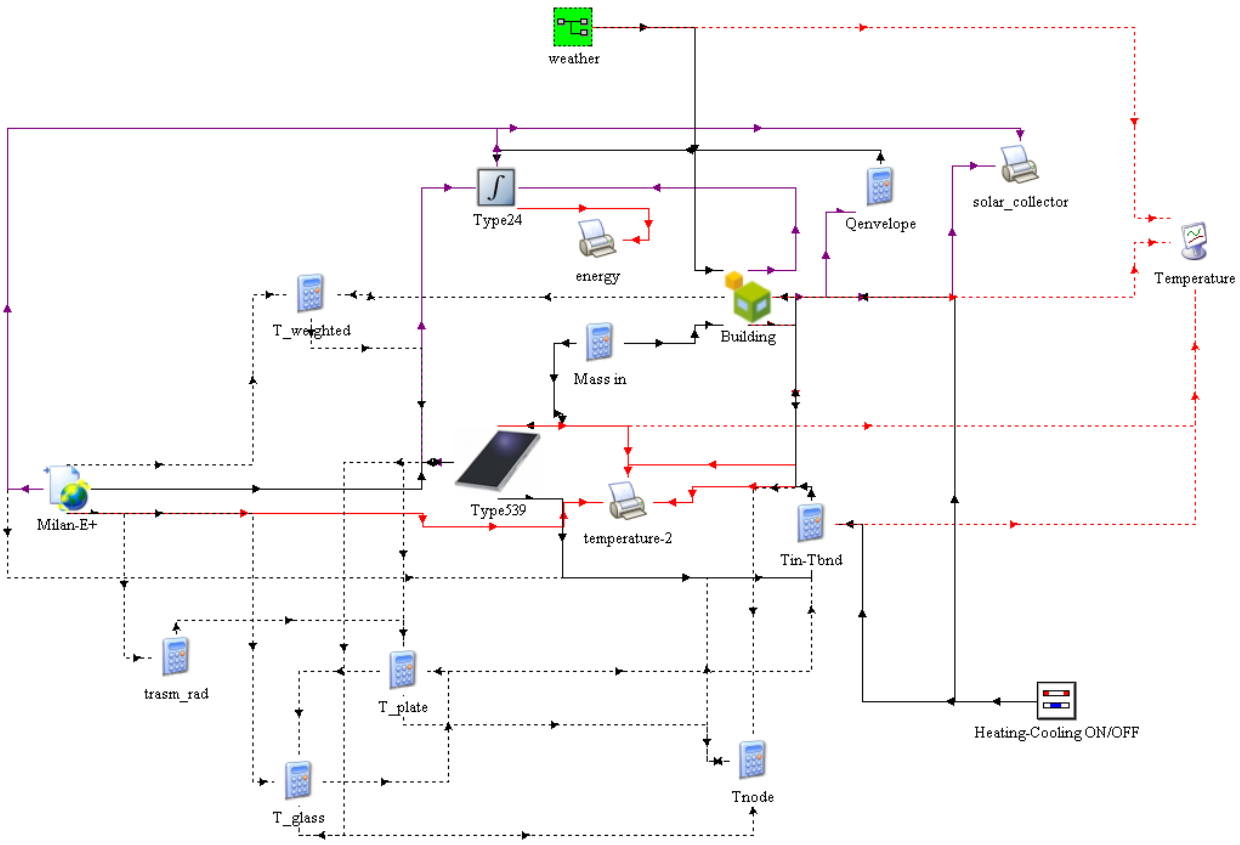

Fig. 65 Trnsys general project

6.1 Reference building

Description

Reference building characteristics are sorted from prior research carried out at the Politecnico di Milano **[16**], concerning the characterization of Milan building stock for energy refurbishment issues. Among the different building typologies introduced in this study, the present work deals to the one showing a good feasibility in integrating the solar

collector array and being at the same time the most widespread in Milan, hereby discussion and results from the previous work are then proposed only for the chosen typology, addressed as typology 2. It is a 5-storey residential building with aligned window that allows introducing up to ten solar thermal array each one composed by 5 collectors connected in series, ***Fig. 66***.

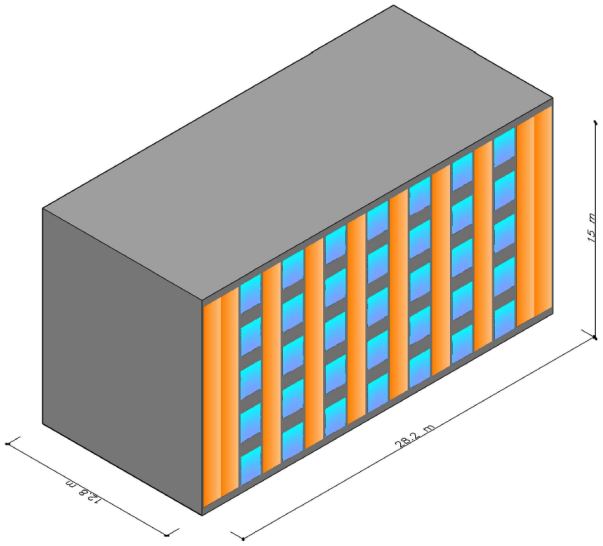

milan building stock typology

EPOCA / DESTINAZIONE D'USO		TIPOLOGIA 1		TIPOLOGIA 2		TIPOLOGIA 3		TIPOLOGIA 4	
		Residenziale	Terziario	Residenziale	Terziario	Residenziale	Terziario	Residenziale	Terziario
Prima del 1919	Epoca 1	x	x	x	x	x (*)	x (*)	x	x
1919 - 45	Epoca 2	x	x	x	x	x (*)	x (*)	x	x
1946 - 61	Epoca 3	x	x	x	x	x (*)	x (*)	x	x
1962 - 71	Epoca 4	x	x	x	x	x	x	x	x
1972 - 81	Epoca 5	x	x	x	x	x	x	x	x
1982 - 91	Epoca 6	x	x	x	x	x	x	x	x
Dopo il 1991	Epoca 7	x	x	x	x	x	x	x	x

For each typology the age of construction to which each of them belong to is outlined as well as the intended use: residential/office.

Fig. 66 on the left, reference building where 10 solar collector string are supposed to be integrated in the south wall. On the right the most common building typologies in Milan.

In this previous study, the main constructional characteristics are investigated, typology by typology with respect of the building age and to the intended use of building. Specifically only building from 1962-1981 having the same envelope characteristics are considered in present work, once again for being the most diffuse in the Milan building stock and in the Italian scenario generally. For narrowing the current field on investigation only residential intended use in building has been considered in present work. Thickness, transmittance value, surface density and specific heat are the parameter displayed for each envelope component, as well as main characteristic of windows are also outlined, ***tab. 39***.

tab. 39 Reference Building envelope characteristich with reference to the chosen age of construction				
opaque envelope	s [cm]	U [W(m²K)$^{-1}$]	Ms [kg m^{-2}]	C [kJ(m$_2$K)$^{-1}$]
wall	31.0	1.14	212.1	185.4
roof	33.0	0.96	313.0	298.9
ground floor	29.0	1.63	384.0	326.9
floor	31.0	1.56	384.0	326.8
partition	12.0	1.93	108.6	108.6
transparent	glass	frame	tot	
window	6.26	3.63	5.80	U [W(m²K)$^{-1}$]
	0.86	-	-	SHGC

Once the building envelope is defined in the previous study, some hypothesis have been done regarding heating/cooling plant differentiating stand-alone installation from the centralised system. Regarding the residential building referred to the chosen typology, it was supposed a gas boiler as heating generator and thermal radiators as emission system for heating while heat pump are used for cooling; all technical characteristics and efficiencies belong to the UNI TS 11300-2 and UNI TS 11300-3, tab. 40. At the same time an hourly profile for occupancy and for all internal gains while ventilation losses it refers to UNI EN 15251 introducing an air change rate equal to 0.762 m^3/hr.

tab. 40 Heating plant efficiency by regulation					
	η-emission	η-generation	η-distribution	η-regulation	η-global
HEATING	0.90	0.86	0.93	0.85	0.61
COOLING	0.97	2 (EER)	-	0.98	-

Once the different typologies were assessed at envelope level as well as plant and internal gain level, simulation by means of Energy+ were run for all the basic cases, for obtaining the actual energy demand for each typologies and extrapolating data at city scale considering their spread with respect to the Milan urban fabric. Moreover energy refurbishment measures were supposed and other simulations run getting results on the impact of such a measures at urban level again. Specifically, it was supposed to reducing the transmittance values for the opaque and the transparent building components according to Italian

regulation valid in 2009-2011 that introduced minimum values for that parameters according to the climatic zone: U_{wall}=0.34, U_{roof}=0.30, U_{floor}=0.33 U_{window}=2.20 $Wm^{-2}K^{-1}$. Moreover, considering cooling energy demand night ventilation was considered as well and each refurbishment measure assessed individually or coupled each other's according to tab. 41, tab. 42.

tab. 41 Heating energy demand reduction measures	
measure 1	reducing transmittance values of all opaque component of the building envelope
measure 2	reducing transmittance values of transparent component of the building envelope
measure 3	reducing transmittance values of transparent component of the building envelope while using glass with g<0.5
measure 4	measure 1 + measure 2
measure 5	measure 1 + measure 3

tab. 42 Cooling energy demand reduction measure	
measure 1	night ventilation
measure 2	reducing transmittance values of all opaque component of the building envelope
measure 3	measure 1 + measure 2
measure 4	reducing transmittance values of transparent component of the building envelope
measure 5	measure 1 + measure 4
measure 6	reducing transmittance values of transparent component of the building envelope while using glass with g<0.5
measure 7	measure 1 + measure 6
measure 8	measure 2 + measure 4
measure 9	measure 1 + measure 2 + measure 4
measure 10	measure 4 + measure 6
measure 11	measure 1 + measure 4 + measure 6

Results

According to the purpose of present study, only results at building scale are reported referring to the chosen reference building: residential building referred to typology 2 and constructed from 1962 until 1981. Results on the basic studied case are shown in ***Fig. 67*** for heating and cooling energy demand. What is of relevance is that except for typology 1

whose characteristics are totally different form the other typologies, the chosen reference case shows a comparable seasonal energy demand if compared to the other studied cases, specifically $Q_{heating}$= 67.5 kWh($m^{-2}y^{-1}$) while $Q_{cooling}$= 17.1 kWh($m^{-2}y^{-1}$).

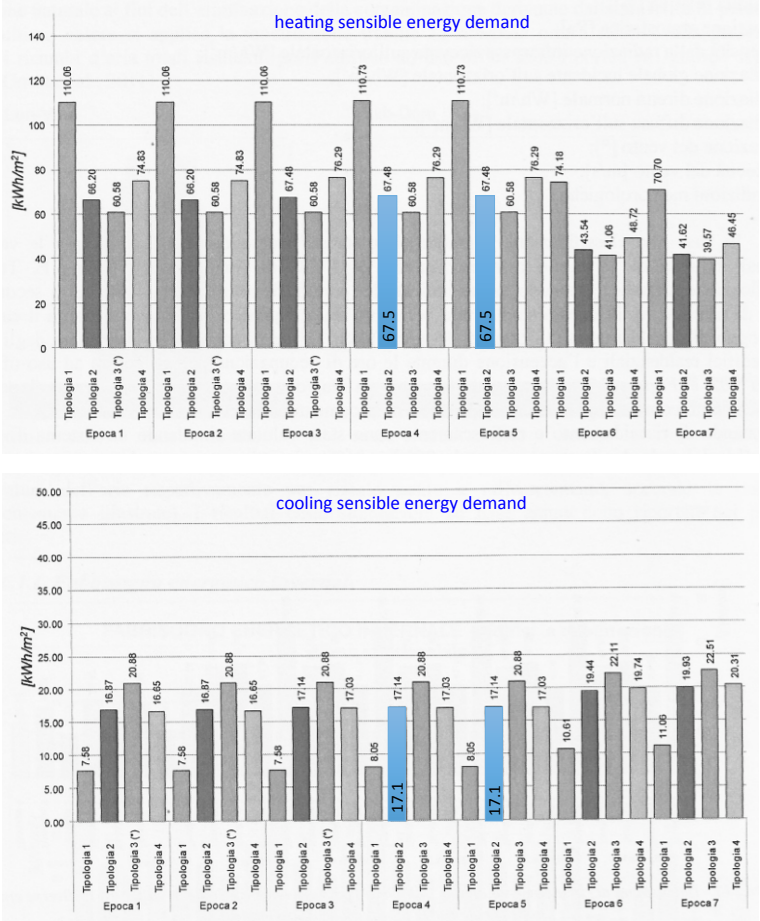

Fig. 67 Seasonal energy demand for residential building distinguished by building typology with reference to the age of construction, results for the chosen reference case is blue-outlined

When energy refurbishment measures are considered and simulation run for the chosen reference building, reduction of heating and cooling energy demand are obviously obtained but some notices have been outlined. Heating performances are mainly affected by windows and opaque envelope components transmittance reduction (***Fig.*** *68*) meanwhile when cooling performance are considered the U_{wall}, U_{roof} and U_{floor} reduction leads to an increase in the energy demand with respect to the building as it is. Decreasing g-value of glass is definitively important during summer (***Fig.*** *69*) meanwhile during winter it is necessary to put all measures together for obtaining good results.

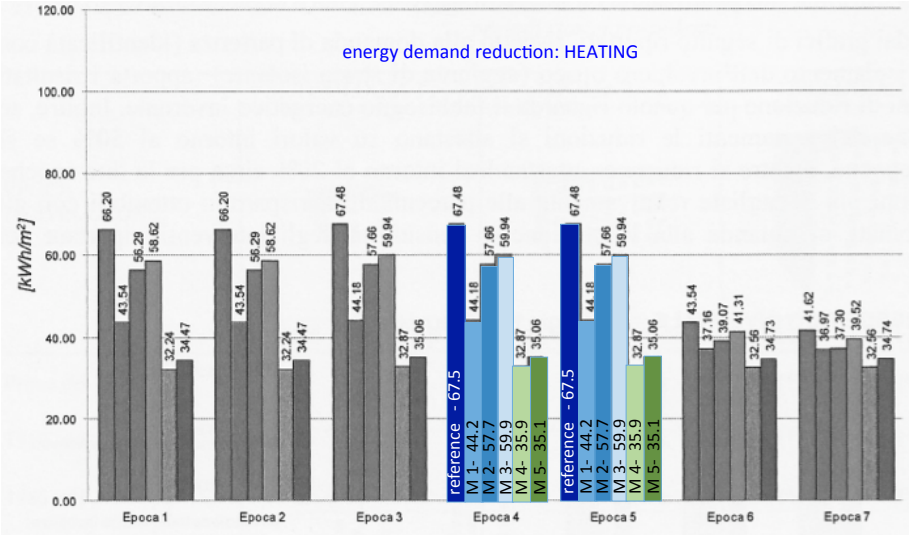

*Fig. **68** Heating energy demand reduction for the different energy refurbishement scenario as presented in* **tab. 41**. *'M' stays for measure while dark blue color refered to the basic building.*

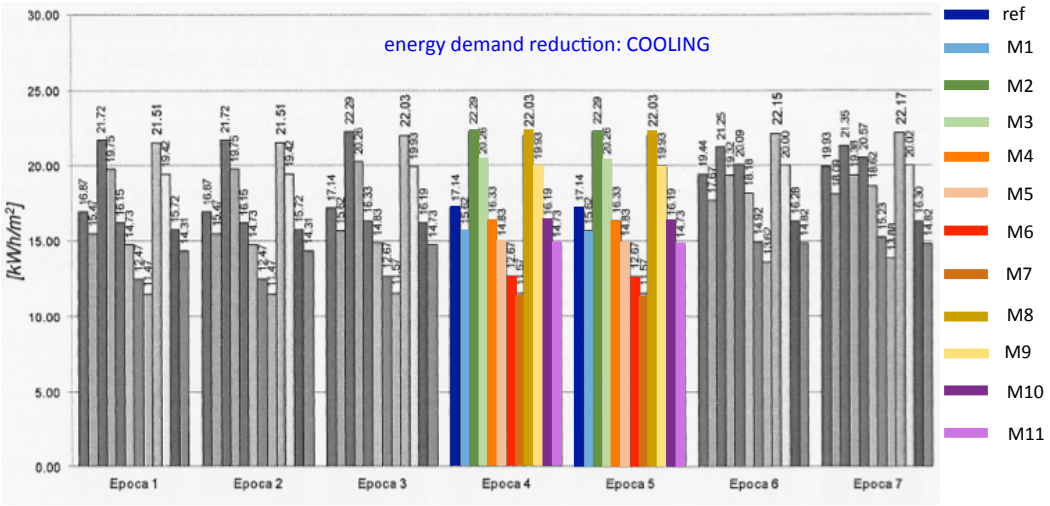

*Fig. **69** Cooling energy demand reduction for the different energy refurbishement scenario as presented in* **tab. 41**. *'M' stays for measure while dark blue color refered to the basic building.*

Presents results are extremely important for the purpose of the present study where the effect at thermal level on building envelope for an integrated solar collector will be analysed.

6.2 Interface temperature from type 539.

Type 539 already described in previous chapter is suitable for finding out the outlet temperature and the useful energy from the collector introducing the main collector characteristics:

- Efficiency curve (η)
- Collector thermal capacity (Cc)
- Incident Angle Modifier (IAM)

According to the needed ventilation rate in the building the most appropriate efficiency curve is the one at m=0.05 $m^3m^{-2}s^{-1}$ sorted as a function of $(T_{in}-T_{amb})/I_{sun}$. Moreover, only data at m=0.05 $m^3m^{-2}s^{-1}$ are actually available and are suitable in determining the $h_{channel}$ value needful in solving the required system of equation.

Finally, the coefficient of the incident angle modifier (IAM) is set at 0.136 as suggested by Duffie and Beckman **[3**] while having a look again at the basic formula:

$$C\frac{dT}{dt} = F'\left(I - U_L(T - T_{amb})\right) - \dot{m}c_p(T - T_{in})$$

$$I = (\tau\alpha)_n IAM\ A\ I_{sun}$$

where as already outlined throughout the present work, T_{amb} is approximated at $T_{amb,w}$ in order to account on the fact that the collector is integrated and consequently the real temperature at internal and external boundaries are definitively different.

The model is firstly run in steady state condition at different irradiance and ambient temperature values from tab. 30 and results are compared with those belonging to Prototype A in Comsol© model. As shown in ***Fig. 70*** Trnsys model has a good reliability for prototype A with respect to the validated FEM model, expect for the lowest irradiation value. Anyway, the absolute error is about 2°C and consequently no relevant mistakes are foreseeable in results.

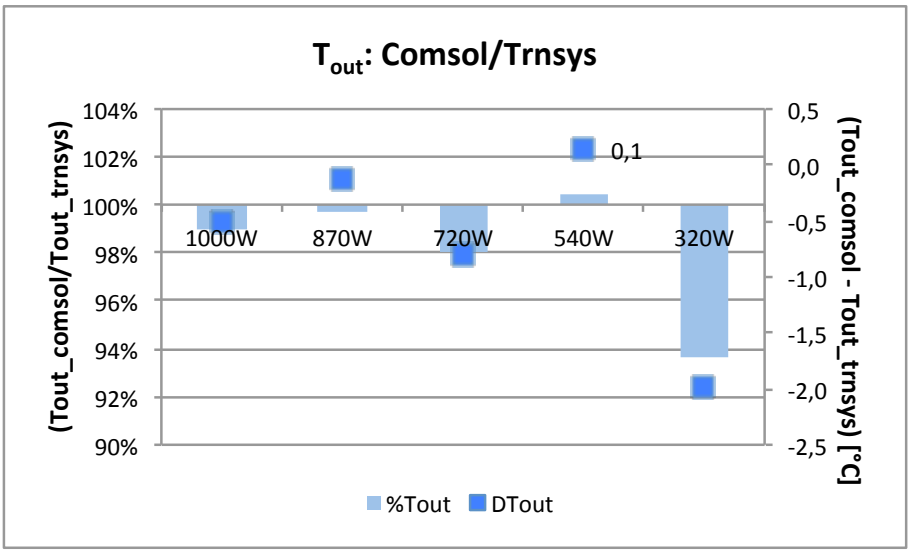

Fig. 70 Transys/comsol results comparison in standard condition.

Once the outlet temperatures are sorted with an appropriate reliability with respect to results from FEM model, a thermodynamic system is introduced in order to look for T_{node}, ***Fig. 71***. Actually, it is useful to identify two sub-systems related each other by the common boundary condition at the channel: $T_f=T_{out}$ where T_{out} is the outlet temperature from type 539 and $h_{conv}=h_{channel}$ where $h_{channel}$=45 $Wm^{-2}K^{-1}$ at the desired m_{in}=0.05 $m^3m^{-2}s^{-1}$ belongs to the validated FEM model.

The first system is the one effectively useful for sorting the searched T_{node}; the STC-wall layers whose thermal characteristics are already defined compose it. Through the upper boundary the solar radiation, filtered by the glass, enter the system while aside from the convective flux described by T_{out} and $h_{channel}$, radiative heat fluxes occurs between the plate and the glass cover surface whose temperature is at the moment unknown, as well as the h_{rad} value depending on it. Meanwhile the down boundary is essentially the indoor ambient and it is defined by the fixed cooling/heating T_{indoor} and by the convective/radiative coefficient $h_{conv\text{-}rad,back}$, as prescribed by UNI EN ISO 6946. The back heat flux through this system is then:

$$Q_{back} = (\tau_{tot}\, I_{sun})\alpha - h_{conv,top}(T_p - T_f) - h_{rad}(T_p - T_g) - h_{conv-rad,back}(T_b - T_{indoor}) - \frac{(T_p - T_b)}{R_1 + R_2}$$

It is then useful to introduce the definition of sol-air temperature ($T_{sol-air}$) considering the radiative and convective coefficients at the up boundary and making the assumption $T_{sol-air} \rightarrow T_p$:

$$T_p \cong T_{sol,air} = T_f + \frac{(\tau_{tot} I_{sun})\alpha}{h_{conv,top} + h_{rad,top}}$$

where plate absorption coefficient, as well as h_{conv}, accounts on coefficients belonging to the Comsol calibration procedure, specifically $\alpha = \varepsilon = 0.5(\varepsilon_{B1} + \varepsilon_{B2})$ and $h_{conv} = h_{channel} = 45$ $Wm^{-2}K^{-1}$ while $T_f = T_{out}$ from Type 539.

Looking at previous formula it is evident that the main unknown variable is the radiative coefficient between plate and glass. Indeed, if down-boundary phenomena could be easily approximated in System A at the up boundary, the radiative exchange whose influence is definitively important are not immediately available and for that reason System B in ***Fig. 71*** is introduced. This system is essentially composed by the glass cover and bounds at the upper surface with the external ambient defined by radiative fluxes toward the sky by means of T_{sky} and $h_{rad,sky}$ and at the same time defined by wind dominated convective flux whose describing variables are $T_{outdoor}$ and h_{wind}.

The searched unknown h_{rad} depends on both plate and glass temperature beyond the radiative properties of surfaces, tab. 11:

$$h_{rad} = \sigma \frac{\left({T_p}^2 + {T_g}^2\right)\left(T_p + T_g\right)}{\frac{1}{\varepsilon_{p,B2}} + \frac{1}{\varepsilon_{g,B2}} - 1}$$

where the emissivities of interest are the ones in the second band, considering that the analyzed radiative phenomenon happens in the IR band. Glass temperature is then evaluated by solving System B:

$$Q_{glass} = U_{glass}\left(T_f - T_{outdoor}\right)$$

$$U_{glass} = \left(\frac{1}{h_{outdoor}} + \frac{s_{glass}}{k_{glass}} + \frac{1}{h_{f,conv}}\right)^{-1} \quad ; \quad T_g = T_f - \frac{Q_{glass}}{h_{f,conv}} = T_f - T'$$

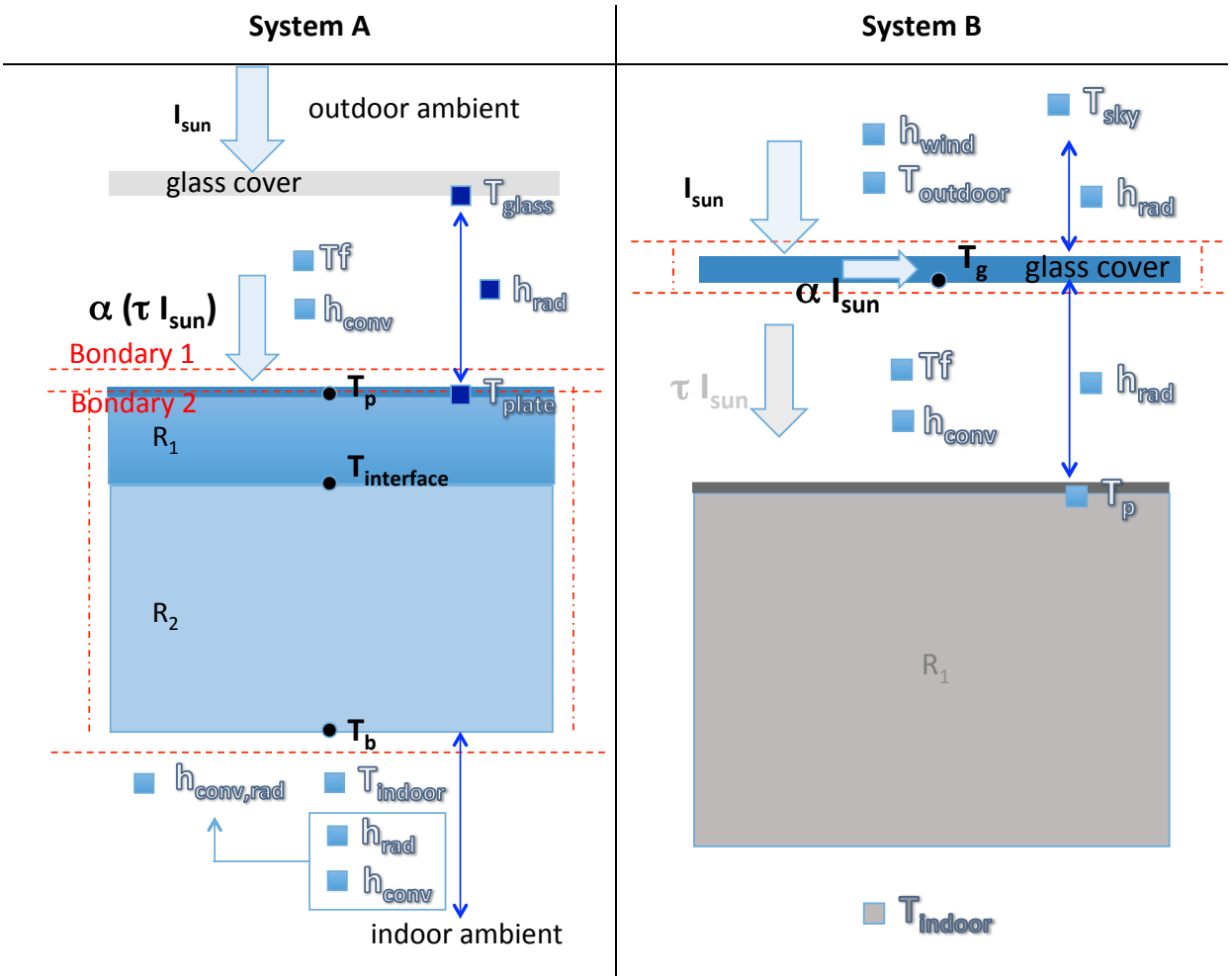

Fig. 71 STC-wall themodynamic system

Substituting this value in the h_{rad} formula, the resulting radiative coefficient is then introduced in Q_{back} balance while expressing T_g in function of T_f :

$$Q_{back} = (\tau_{tot}\, I_{sun})\alpha - (h_{conv,top} + h_{rad})(T_p - T_f) - h_{rad}(T')$$
$$-h_{conv-rad,back}(T_b - T_{indoor}) - \frac{(T_p - T_b)}{R_1 + R_2}$$

At the same time looking at $T_{sol\text{-}air}$ definition it is possible to define the incoming solar radiation as:

$$(h_{conv,top} + h_{rad,top})(T_p - T_f) = (\tau_{tot} I_{sun})\alpha$$

It follows that replacing the incoming solar radiation and introducing the assumption $T_{sol-air} \rightarrow T_p$ the back heat flux is:

$$Q_{back} = -\frac{T'}{{h_{rad}}^{-1}} - \frac{(T_b - T_{indoor})}{{h_{indoor}}^{-1}} - \frac{(T_p - T_b)}{R_1 + R_2}$$

Actually, it is equal to narrow the system A in ***Fig. 71*** from boundary 1 to boundary 2 introducing the T_p equivalent value as $T_{sol\text{-}air}$ that includes itself most of the phenomena happening at boundary 1. From that system the interface temperature is evaluated as:

$$T_{interface} = T_p - Q_{back}(R_1 + R_2)$$

Model is then run at the different ambient conditions from FEM validation procedure for an appropriate lapse of time in order to stabilize results while nullify the thermal inertia effect and results for T_g, T_p and the searched $T_{interface}$ are compared in ***Fig. 72*** and ***Fig. 73*** showing a good reliability for Trnsys model: the relative error lays in a range between +4% and -4%, meanwhile absolute error set in a range +2°C and -2°C inducing at very slow variation in the evaluation of energy transfer through the building envelope component.

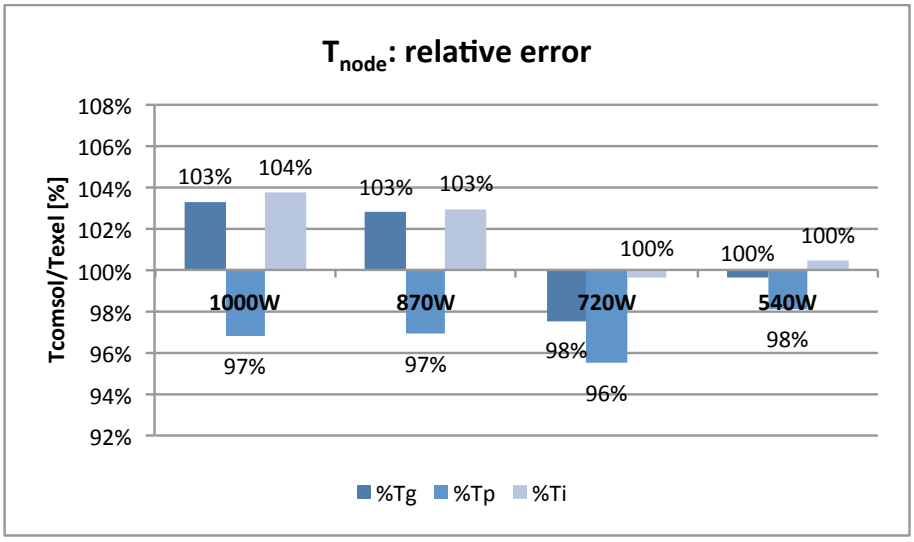

Fig. 72 Results from validation between Trnsys and Comsol models in terms of relative error.

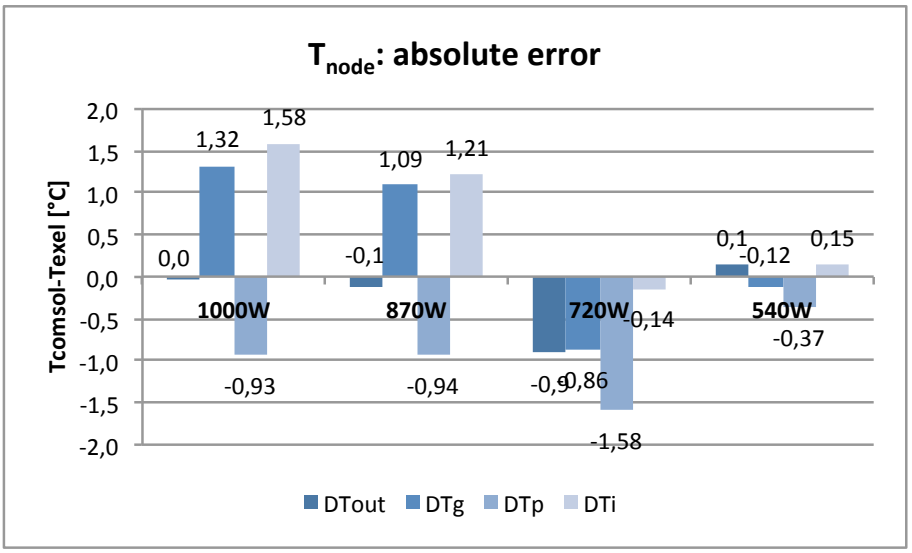

Fig. 73 Results from validation between Trnsys and Comsol models in terms of absolute error.

6.3 The building model

Once the main input for type 56 from type 539 are defined, proper simulations run once for the reference chosen building once for the detected building whose south façade respecting window partition integrates the Solar Thermal component as an energy refurbishment measure. From one side, energy transfer through the STC-wall will be selected while energy production by the solar collector is used for providing pre-heated air for prescribed air change rate according to hygiene regulation during winter.

Actually, what the present work want to demonstrate is how such a measure double affects (at ventilation load and at envelope heat transfer) the building energy balance during heating and cooling periods and consequently the following output are sorted and compared:

Q_{sens}	The sensible energy demand for heating and cooling with reference to a specified $T_{indoor,Heating}$ and $T_{indoor,cooling}$	[kWh $m^{-2}y^{-1}$]
$Q_{envelope}$ **Q_{walls}** **$Q_{STC-wall}$**	Energy transfer through the envelope, distinguishing from the overall value ($Q_{envelepe}$) the rate of south wall ($Q_{STC-wall}$) and the rate of all walls (Q_{wall}).	[kWh $m^{-2}y^{-1}$]
Q_{vent}	The sensible energy from ventilation load	[kWh $m^{-2}y^{-1}$]

For stressing attention on these parameters, a simplified one-zone building model is introduced at geometrical level as well as at building balance level (***Fig. 74***), detailing only features involved in the searched Q_{vent} value and $Q_{south\text{-}wall}$ value. Consequently, equivalent windows surface whose area matches the sum of single window for each exposure replace the window partition of the building. Indeed, if a unique thermal zone is considered, this simplification does not affect calculation. **Internal gain** values belongs to main common Italian standard regulation that prescribes 9 Wm^{-2} for kitchen-living room and 3 Wm^{-2} for bedroom and other, specifically a mean value is considered as constant all over the year:

$$Q_{gain} = 6\, Wm^{-2} \rightarrow 38988\, Jh^{-1}$$

Indoor temperature is fixed at 20°C during heating season and at 26°C during cooling season as prescribed by Italian regulation. The two periods for the city of Milan according to its Degree Day (2404 DD) are respectively from 15th October until 15th April and consequently from 16th April to 14th October. Deadlines for Palermo and Rome are considered in the same manner.

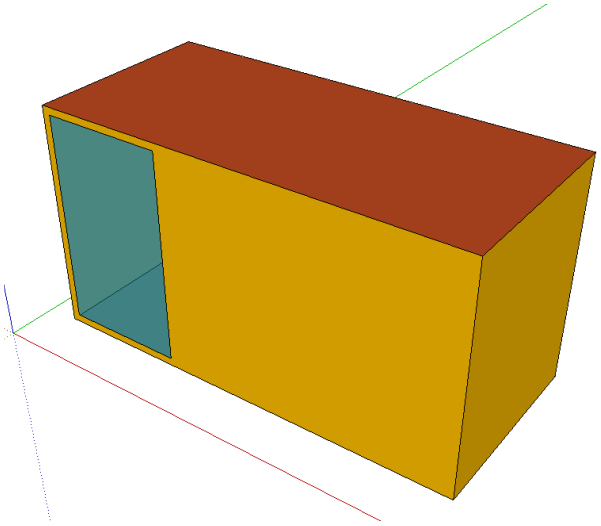

North-South orientation	A_{tot}	423.00 m^2
	A_{window}	112.80 m^2
East-West orientation	A_{tot}	192.00 m^2
	A_{window}	0.00 m^2
Ground/Roof	A_{tot}	360.96 m^2
Window	L_{window}	1.6 m
	H_{window}	2.00 m
	%glass	80%
	%frame	20%

heating period

Palermo: 1st dec – 31st mar

Rome: 1st nov – 15th apr

Milan: 15th oct – 15th apr

Fig. 74 Simplified Trnsys building model

Regarding **transmission through the building envelope**, the required inputs by the software are thermal conductivity (k – [kJ(m K hr)$^{-1}$]), mass density (ρ - [kg m^{-3}]) and specific heat [cp - kJ(kg K)$^{-1}$]) meanwhile data for the reference building **[16**] provides thickness (s –[m]), transmittance value (U – [W m^{-2}K^{-1}]), surface density (ρ_s – [kg m^{-2}]) and specific heat (cp_s – [kJ m^{-2}K^{-1}]) (***tab. 39***). Hence starting from the known values aside from the due change of units the required inputs are sorted as follows:

$$cp = {}^{cp_s}/_{\rho_s} \qquad\qquad \rho = {}^{\rho_s}/_{s}$$

Some notices has to be outlined regarding the building envelope transmittance distinguishing generic envelope component from the wall component, indeed as declared and according to the aim of present work, more detailed attention is put in defining the heat transfer through the façade for outlining the effect of introducing the STC-wall. Moreover considering that a single unique thermal zone has been introduced, only external roof and ground floor will be differentiating in calculation and in detailing from external wall.
Specifically an equivalent k-value for these two elements regardless the layer construction is evaluated by the given transmittance and thickness values, considering boundary heat coefficients as prescribed by UNI EN ISO 6946:

$$k_{eq} = \frac{\left(U^{-1} - \frac{1}{h_{outdoor}} - \frac{1}{h_{indoor}}\right)}{s}$$

It has to be noticed for the ground floor that it has been supposed to bound with a basement by means of introducing the appropriate $h_{outdoor}$ assuming the basement temperature is equal to the external one.

tab. 43 building envelope component input

Building component	s [m]	κ [W/m^{2}K]	ρ [Kg/m^3]	c_p [J/kg K]	U [m^{2}K/W]	**note**
external roof	0.33	0.36	950	960	0.956	equivalent values of thermal conductivity are introduced
ground floor	0.29	0.72	1200	740	1.625	

Regarding external façades, higher level of detail is then provided. Wall layers from the Italian Thermo-technical Commitee **[17]** are considered for building up model. If the reference building and the building with an integrated solar thermal collector of south façade are considered, the focus point and main difference between the two simulations is the south wall outdoor boundary condition. As usual in the reference model heat transfer coefficient corresponding to European regulation and including convective/radiative phenomena at the external surfaces is provided. Meanwhile in the detected building model this input is replaced by the surface temperature ($T_{interface}$) calculated by the introduced system of equations previously defined; both incoming solar radiation as well as convective/radiative exchange are turned off since they are already evaluated in Tinterface calculation, tab. 44.

tab. 44 external wall input

Layer	s [m]	k [W/m^{2}K]	r [Kg/m^3]	c_p [J/kg K]	R [m^{2}K/W]	T [°C]	**note**
outdoor BND					0.04$^{(*)}$	$T_{outdoor}$	wall
					none	$T_{interface}$	STC-wall
outdoor plaster	0.020	0.900	1800	837			
perforated brick	0.120	0.387	717	837			
air gap	0.060	0.278	1	1004	0.18$^{(*)}$		
perforated brick	0.080	0.400	775	837			
indoor plaster	0.020	0.900	1800	837			
indoor BND					0.13$^{(*)}$	$T_{intdoor}$	

$^{(*)}$ UNI EN ISO 6946 [24]

Some other considerations concerning windows characteristics follows, the reference work from Politecnico di Milano deals with window structure typical from 1960-1980. It is single glass window with wooden frame (oak) whose total thermal transmittance is U_W=5.80 Wm^{-2}K^{-1} while solar transmittance is equal to 0.9 and the Solar Heat Gain Coefficient is 0.86. Such a windows have been usually replaced during the years. Considering that point, that windows are not part of the present investigation and consequently they don't change from the reference-building model to the STC-building model, a double-glazing system with aluminum frame is introduced for having a better matching with the real Italian building stock. Main characteristics are, at thermal level, U_W= 2.83 Wm^{-2}K^{-1} and, at optical level, g-value=0.755, t_{sol}=0.693, t_{vis}=0.817 and r_{sol}=0.126 .

Finally, regarding **ventilation load** as well known it is really difficult to evaluate the rate from infiltration and actually they have been omitted in present simulation meanwhile the focus point is to evaluate how much pre-heating air by means of the integrated solar collector array could reduce energy demand during heating period. Software evaluates this contribution to the overall balance by means of:

$$Q_{vent} = V\ \rho\ cp\ (T_{vent} - T_{zone})$$

where V is the volume of the incoming air, ρ and cp respectively the density and the specific heat of air itself, T_{zone} the fixed indoor temperature according to heating and cooling conditioning plant set, meanwhile according to the declared aim T_{vent} is equal to the outlet temperature from type 539 during heating period whenever $T_{outlet}>T_{outdoor}$ and it is equal to $T_{outdoor}$ during the cooling period and whenever $T_{outlet}<T_{outdoor}$. For sake of detail the air change per hour is set at 0.3 according to Italian regulation.

What is of interest for present work is how Trnsys evaluate the heat transfer through the building envelope in which the transfer function method by Mitalas is applied according to which solutions are evaluated time step by time step (k):

$$\dot{q_{si}} = \sum_{k=0}^{n_{bs}} {b_s}^k {T_{s,o}}^k - \sum_{k=0}^{n_{cs}} {c_s}^k {T_{s,i}}^k - \sum_{k=1}^{n_{ds}} {d_s}^k {\dot{q}_{s,i}}^k$$

$$\dot{q_{so}} = \sum_{k=0}^{n_{as}} {a_s}^k {T_{s,o}}^k - \sum_{k=0}^{n_{bs}} {b_s}^k {T_{s,i}}^k - \sum_{k=1}^{n_{ds}} {d_s}^k {\dot{q}_{s,o}}^k$$

where meaning of coefficient are explicated in ***Fig. 75*** the coefficient are determined by using the z-transfer function reference routine. For external wall the inside heat flux is evaluated by a combination of boundary air temperatures:

$$\dot{q_{s,i}} = B_s T_{a,s} - C_s T_{a,s} + D_s$$

where B_s, C_s, and D_s depends in turn on convective coefficient at the outside surface, on the fraction of sky view from the outer surface, on the incoming solar radiation on the surface itself and on the corresponding transfer equation.

Whenever the outside temperature is provided, as for STC-wall is, the outdoor temperature T_{as} is substituted by the known one (in this model $T_{interface}$) meanwhile by setting the h_{back} coefficient of outer surface at almost zero it follows: $T_{a,s}=T_{b,s}=T_{s,o}$ as required by the present intent for simulation.

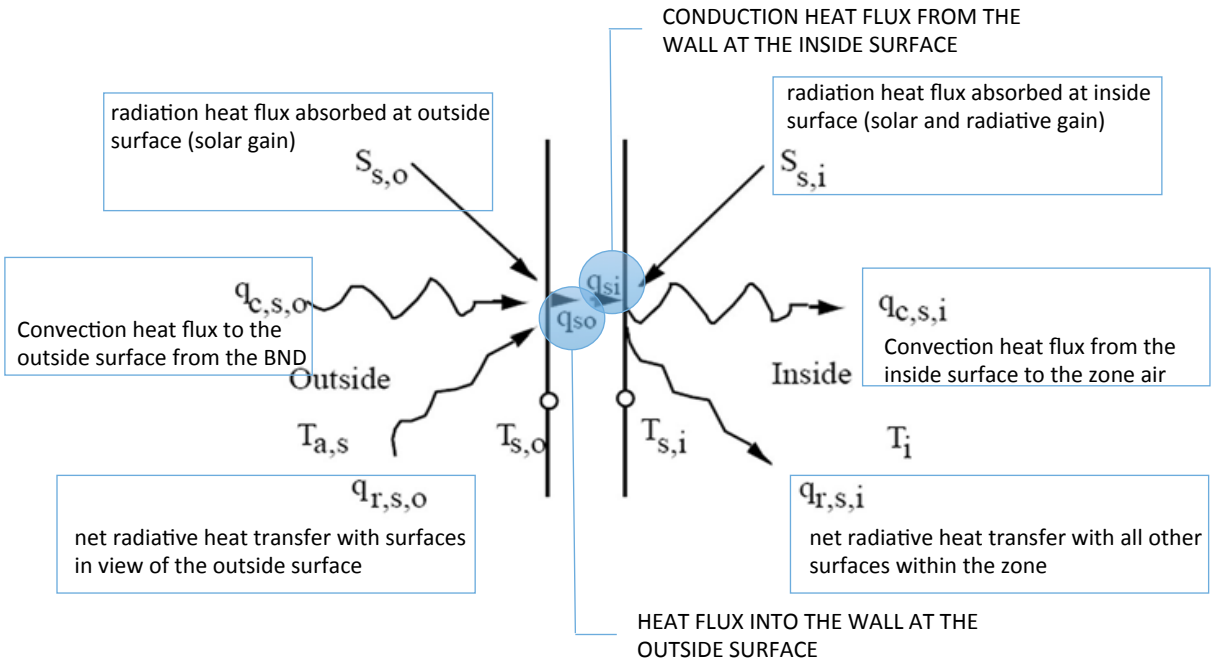

Fig. 75 Surface it fluxes and temperature

6.4 Building results and discussion

Trnsys model run for the typical year in Milan, Rome and Palermo, sorting the desired outputs once for the reference building itself once for the building where the STC-wall is south façade integrated. This latter configuration will be addressed as STC-building. Moreover, for the reason why only T_{node} at m=0.05 $m^3(m^2s)^{-1}$ are validated in previous chapter with respect of the prototype A model, only the configuration STC-wall A is considered. Actually only data from the experimental campaign on prototype A reports also the plate temperature allowing to validate at first prototype A (and consequently STC-wall A) with respect to T_p obtaining reasonable data for all other significant node temperatures.
Meanwhile model set up is assessed for outlining the effect of STC-wall at building energy balance. For that reason results for reference building are different from those in the previous study undertaken at the Politecnico di Milano, ***Fig. 76***, even if they are basically comparable.

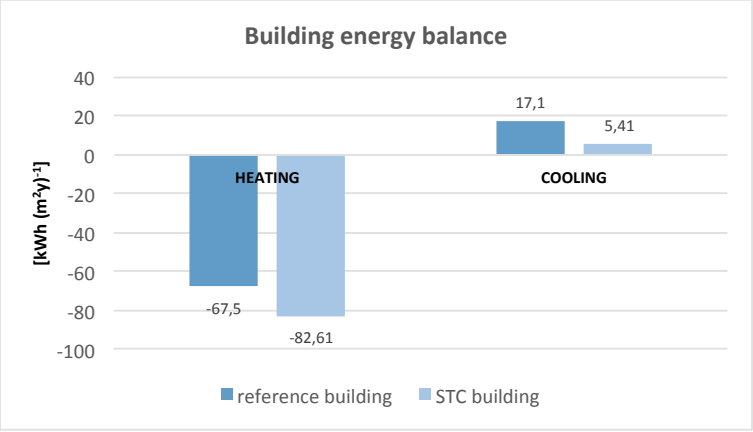

Fig. 76 Building energy balance for heating and cooling seasons: comparison between reference building as calculated by Trnsys and the results from original model belonging to previous study performed by Energy+.

Actually, different software have been used (Energy+ ; Trnsys) and overall internal gain for the previous study are really detailed with weekly and seasonal profile while present work refers to a constant value from national regulation.
Aside the necessary initial comparison between the two models, what is of interest for the present study is the comparison between the reference building and the STC-building results belonging to the same simulation setting.

An initial evaluation on reference buildings according to different sites is then necessary focusing on the double effects of STC-wall in terms of heat transfer through the south façade and in terms of ventilation load.

At a first sight, Milan heating balance is more affected by the heat losses through its envelope (wall, roof, ground floor and windows) than Rome and Palermo (respectively 80%, 70% and 50%).

At the same time and at a deeper detail level, it is interesting to make some comparison focusing on heat transfer through the opaque component in south façade, ventilation load and sensible zone load in heating and cooling periods for the reference building ***Fig. 77***.

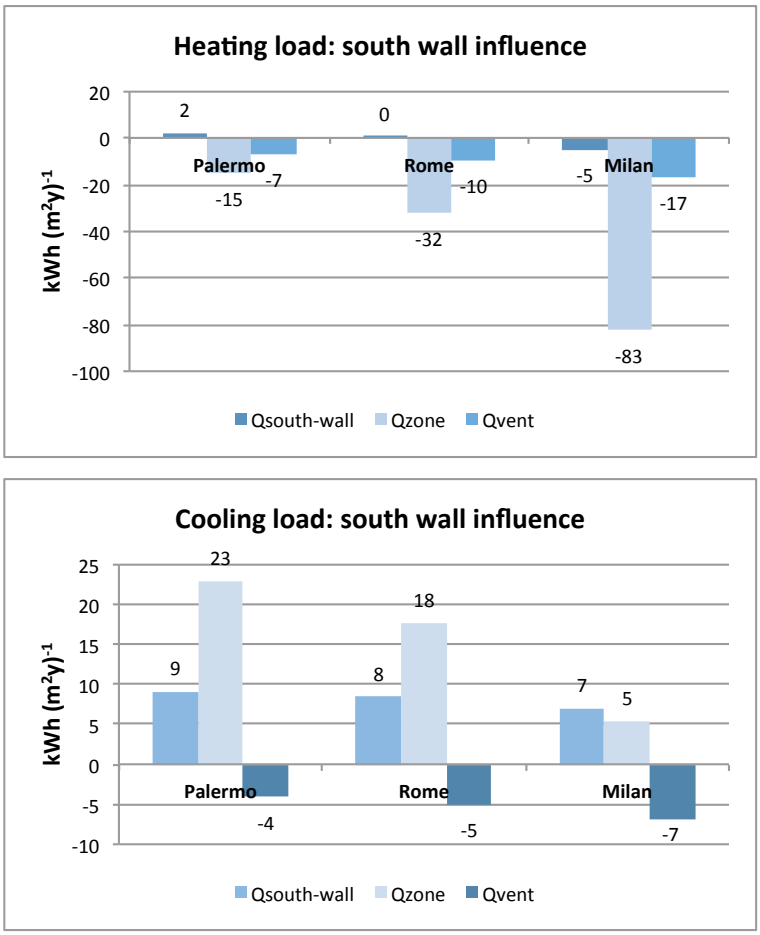

Fig. 77 South wall load influences on seasonal energy balance.

Basically a difference between cooling and heating building balance exists meanwhile the same trend is recorded in the three sites. During winter, the zone balance is mostly affected by ventilation meanwhile during summer south wall contribute to balance increasing energy demand while ventilation has an opposite sign.

Consequently, introducing the STC-building, some points need special attention:

- from one hand heating energy balance will be positively affected
- from the other hand cooling instances will be negatively influenced.

Comparing heating and cooling energy balances it is then necessary to determine whether it is suitable to integrate a solar air collector.

At a first evaluation seasonal balance are considered (***Fig. 78***) and actually some reduction are recorded for heating period meanwhile cooling season results are not really affected by the STC-wall.

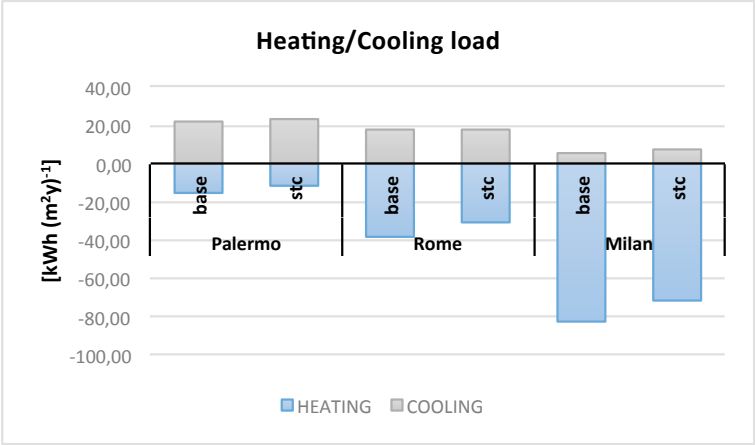

Fig. 78 Building energy balance for heating and cooling seasons: comparison between reference building and STC-building

Actually, considering relative and absolute differences between the reference building and the STC one in ***Fig. 79*** better results are recorded for the city of Palermo in heating balance even if in absolute value higher difference are noted in Milan. Finally at cooling thermal balance level, maximum increase sets at +2 $kWh(m^2y)^{-1}$ in Milan, this behaviour could be explained considering the solar geometry and the variation of irradiation input according to months and latitudes.

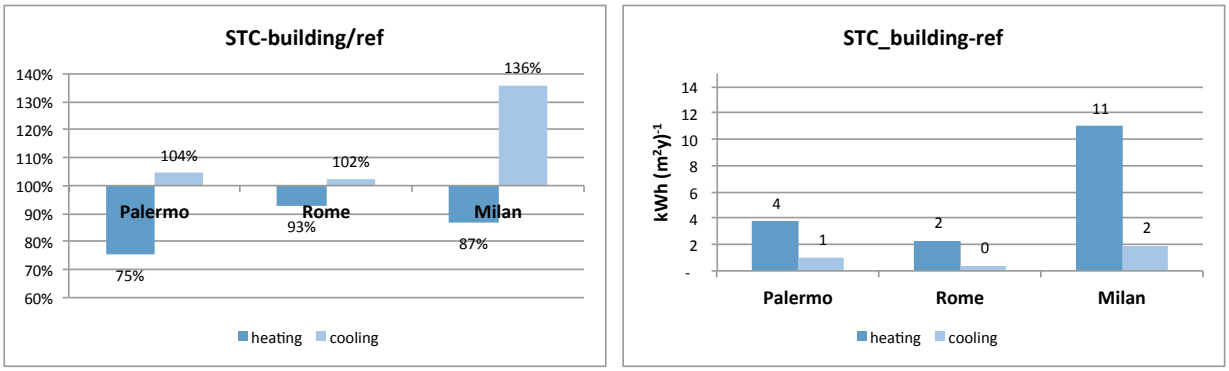

Fig. 79 Absolute and relative differences between reference building and STC-building.

Focusing then on STC-wall contribution to the overall balance results are proposed with respect to the collector surface. A monthly analysis is then proposed in ***Fig. 80***. As already outlined and as predictable, transmission through the south façade are always positive when STC-wall is addressed with higher desirable impact during winter months. Anyway effects on cooling performances could not be neglected and ratio between heating and cooling wall gains are introduced:

$$\frac{H}{C} = \frac{Q_{heating,STC} - Q_{heating,ref}}{Q_{cooling,STC} - Q_{cooling,ref}}$$

Fig. 81 shows results, STC-wall is then generally suitable being the heating gain related to STC-building higher then the undesirable increase in wall heat transfer during cooling season.

Moreover also ventilation load decreases during heating period, at this regard it is interesting to notice how during summer some difference are notice even if in both reference and STC cases the inlet temperature is the outdoor temperature. This difference is due to a secondary effect of the STC-wall, actually if the zone temperatures in STC-building and in ref-building are compared differences about 0,5 - 1 °C are recorded.

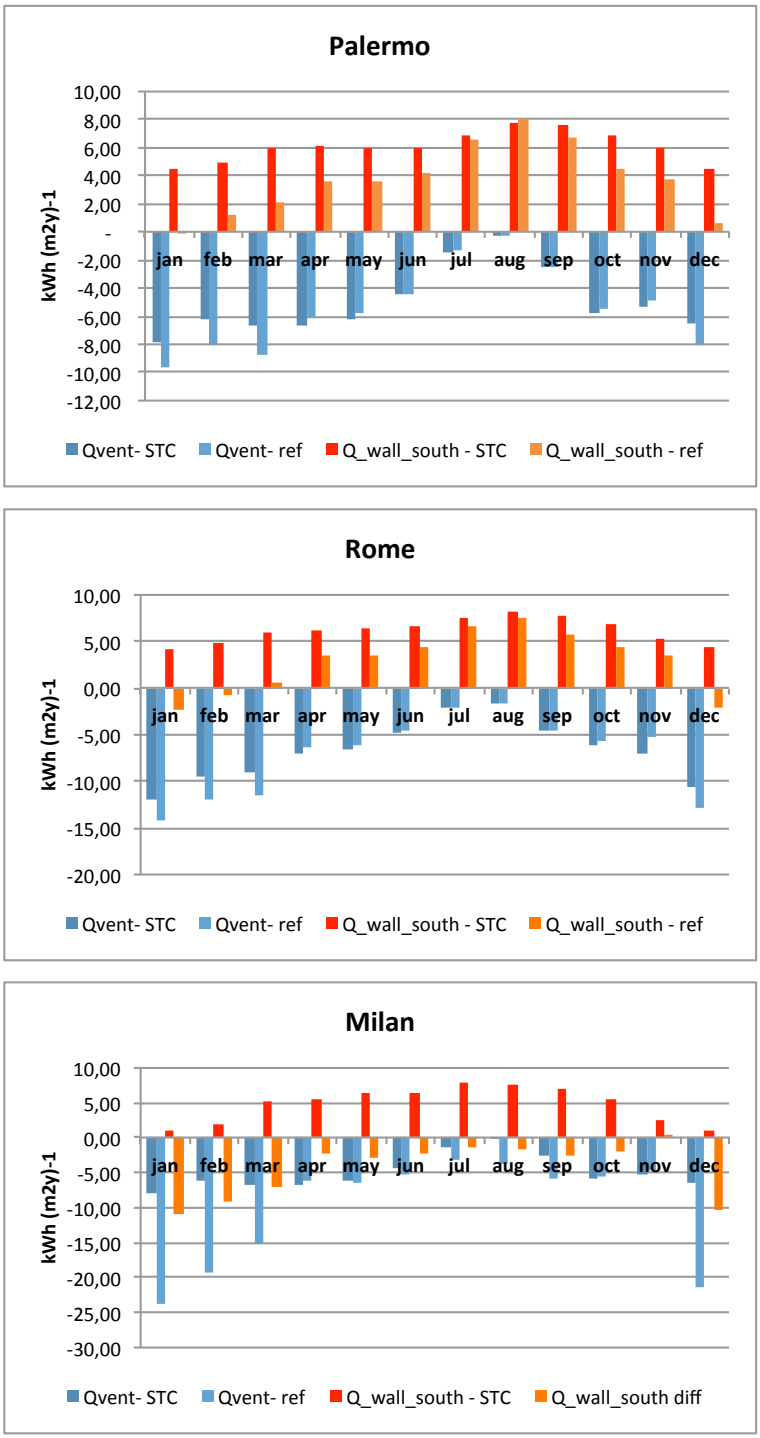

Fig. 80 STC-wall active and passive contribution to the monthly balance.

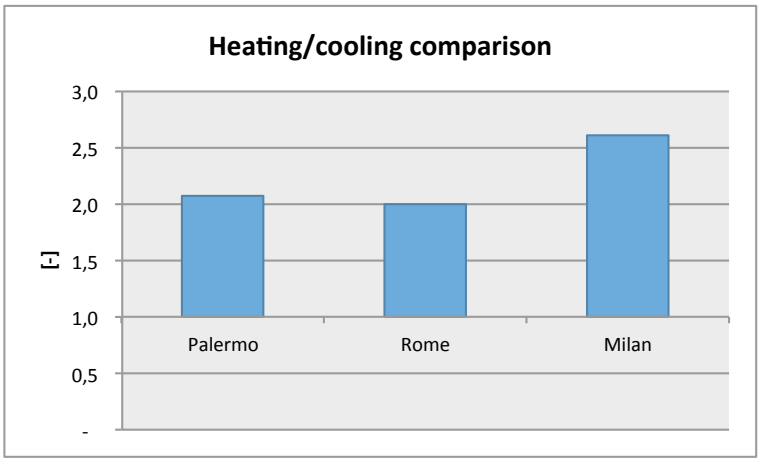

Fig. 81 STC-wall overall performance evaluation

7. CONCLUSION

Present work focused on energy performance of two low cost integrated solar thermal collectors. Analysis on the thermal balance of the component as well as building energy balance on a reference building has been carried out. Primary results show how positive interactions are generally achieved by the integrated component in both functions: as a passive building envelope component and as an active thermal plant component. It is important to notice that not a standard method for evaluating integrated collector performances is available yet. Moreover data for characterising the solar collector are usually and more easily acquired for stand-alone installation. For that reason, present work deals to a method based on FEM model assessment: available recorded data are in this case useful for validating and calibrating a stand alone component FEM model. Afterward, bottom boundary conditions are changed as well as wall layers introduced so that FEM model is used for checking temperature field for the integrated component.

Moreover standard procedures for sorting solar thermal collector efficiency curves refer again to stand-alone collector, then for accounting on the fact that the bottom boundary for the integrated component is the indoor ambient, an outdoor/indoor averaged weighted temperature is introduced in calculation, meanwhile thermal resistances towards the indoor ambient belongs to the standard rule for calculating the heat transfer through the wall itself.

Two interpretations of results could be done, distinguishing the passive and active contributions of the integrated component on the building energy balance.

Specifically, lowering the back loss coefficient leads to some improvements in the collector efficiency but other considerations have to be done considering the two prototypes are two low-cost ones. Indeed, they are both characterized by a single glass cover while thermal bridge at the perimeter is not enough properly designed in order to reduce its effect in favor of an easy and fast assembling during building renovation work. Consequently, they are presumably are extremely dependent on the thermal top loss and edge loss coefficient more than on U_{back}. Definitively, the cheapest the configuration the highest the efficiency for the integrated component with respect to the stand-alone one, even if more significant results could be achieved reducing firstly thermal bridges while increasing top resistance.

Optimization among component cost, integration feasibility features and energy production could be further addressed case by case.

Actually, the overall performance of collector is affected also by the weather conditions and by its transient response to hourly climatic parameters change. For these reasons, simulations were then run for two different sites characterised by different weather conditions (Palermo, 751 DD and Milan, 2404 DD). For any case, higher daily outlet temperatures are achieved with better performance in the case of the coldest climate. Consequently also the useful energy production increases in both cases steadily over all the year without any difference between summer and winter. Anyway, differences could be outlined between the results from the two simulations; indeed, integrated component is more suitable in Milan where the increase in energy production with respect to the stand-alone component is higher than in Palermo.

Moreover, if STC-wall A and B energy productions in the two cities at different flow rate is analysed, it follows that at m=0.05 $m^3m^{-2}s^{-1}$ there is no relevant difference in choosing configuration A or B in Milan, meanwhile if results at m=0.03 $m^3m^{-2}s^{-1}$ in Milan and results in Palermo without respect to inflow rate are considered STC-wall B is always more suitable then STC-wall A.

Finally, dealing with building energy balance the number of variables at component design level, at building/thermal-plant features level and at climatic level increase. For that reason a reference building that typically represent the Italian building stock is introduced and evaluation on the influences of the integrated component on its energy balance done for a specified site (Milan). What is of primary importance is that heat flux is all over the year from outdoors to indoors avoiding energy losses through the wall during winter when the collector is integrated. It is worth to notice that due to its exposure (the south façade has been chosen), energy flux through the wall does not affect really the summer energy balance for the building. Moreover, also ventilation load obviously decreases introducing pre-heated air from the collector array even if good results would be achieved if larger façade surface was available, meanwhile during summer the produced energy from collector is at the moment discharged.

Summarizing, present work has demonstrated that such a topic of research could be successful but many other efforts are needed and further analysis on different solar component as well as on different building samples are necessary, once for checking the best solution at energy production levels once for generalizing results based on different kind of building and sites. Moreover, the final use of the produced energy while change the typology of the component has to be investigated, too. Good compromise among energy demands from the building, useful energy production by the collector, final use of the produced energy and cost of retrofit action could be probably achieved if such a topics of research will converge in a unique line.

REFERENCES

Physics and Simulation

[1] Bejan A., Kraus A.D., *Heat transfer handbook*, John Wiley & sons. INC, 2003

[2] COMSOL Multiphysics Referece Guide, 2011

[3] Duffie J., Beckman W.A., *Solar engineering of thermal process*, 3rd ed., John Wiley & sons. INC, 2006

[4] Durst F., Fluid Mechanics. *An introduction to the theory of fluid flow*, Springer 2008.

[5] Ferziger J.H., Peric M., *Computational methods for fluid dynamics*, 3rd ed., Springer, 2002

[6] Incropera F.P., DeWitt D.P., Bergman T.L., *Fundamentals of heat and mass transfer*, John Wiley & sons. INC, 2007

[7] Lewis R.W., Nithiarasu P., Seetheramu K.N., *Fundamentals of the Finite Element Method for heat and fluid flow*, John Wiley & sons. INC, 2004.

[8] Modest M.F., *Radiative heat transfer*, 2nd ed., Academic press – Elsevier Science, 2003

[9] Peyret R., Taylor T.D., *Computational method for fluid flow*, Springer-Verlag, New York, 1983

[10] Siegel R., Howell J.R., *Thermal radiation heat transfer*, 3rd ed., Hemisphere Publishing Corporation, 1992.

[11] Trnsys Userguide – volume 5: Mathematical reference

[12] Trnsys Userguide – volume 6: Multizone building modelling with type 56 and TRNBuild

Background

[13] Alvarez A., *Experimental and numerical investigation of a flat-plate solar collector*, Solar Energy 35 (2010) 3707-3716

[14] Baudanza S. , *Analisi delle prestazioni di un collettore solare ad aria*, Università degli Studi di Palermo. A.A. 2011/2012 Degree in Engineer – Thesis, supervisor: prof. V. Lo Brano, ing. P. Finocchiaro

[15] Bellone N., *Solare termico integrabile negli edifici. Sviluppo e test di un sistema low cost*, Università degli Studi di Palermo. A.A. 2010/2011 Degree in Achitecture – Thesis, supervisor: prof. M. Beccali

[16] Costa G., *Caratterizzazione tecnologico-prestazionale del patrimonio edilizio per la valutazione dell'efficacia di strategie energetiche*, Politecnico di Milano, AA. 2009-2011. Phd Thesis, supervisor: prof. P.Caputo, prof. S. Ferrari

[17] Comitato Termotecnico Italiano – CTI, *Prestazioni energetiche degli edifici: climatizzazione invernale e preparazione acqua calda sanitaria per usi igienico-sanitari*, Roma 2003

[18] EN 12975:2006-1. Thermal solar systems and components – Solar Collectors – part 1: general requirement

[19] EN 12975:2006-2. Thermal solar systems and components – Solar Collectors – part 2: tests methods

[20] Official Journal of the European Union - Directive 2010/31/EU of the European Parliament and of the Council (Recast). 19 May 2010.

[21] UNI 8937:1987. Collettori solari piani ad aria. Determinazione del rendimento termico (*Air heating flat plate solar collectors. Determination of the thermal efficiency*)

[22] UNI 10349:1994. Riscaldamento e raffrescamento degli edifici. Dati climatici. (*Heating and cooling. Weather data*).

[23] UNI/TS 11300-1: 2008. Prestazioni energetiche degli edifici. Parte 1: Determinazione del fabbisogno di energia termica dell'edificio per la climatizzazione estiva ed invernale

[24] UNI EN ISO 6946:1999. Componenti e elementi per edilizia - Resistenza termica e trasmittanza termica -Metodo di calcolo (Building components and building elements - Thermal resistance and thermal transmittance - Calculation method.)

[25] UNI EN 12524:2001. Materiali e prodotti per edilizia - Proprietà igrometriche - Valori tabulati di progetto (Building materials and products - Hygrothermal properties - Tabulated design values).

State of the art

NZEB

[26] Athienitis A, Kalogirou SA, Candanedo L. *Modeling and simulation of passive and active solar thermal systems*. Elsevier Ltd; 2012. p. 357-417.

[27] Attia S, Hamdy M, O'Brien W, Carlucci S. *Computational optimisation for zero energy buildings design: Interviews results with twenty eight international experts*. 13th Conference of the International Building Performance Simulation Association, BS 2013. Chambery2013. p. 3698-705.

[28] Ardente F, Beccali M, Cellura M, Mistretta M. *Energy and environmental benefits in public buildings as a result of retrofit actions*. Renewable and Sustainable Energy Reviews. 2011;15:460-70.

[29] Beccali M, Cellura M, Fontana M, Longo S, Mistretta M. *Energy retrofit of a single-family house: Life cycle net energy saving and environmental benefits*. Renewable and Sustainable Energy Reviews. 2013;27:283-93.

[30] Cellura M, Campanella L, Ciulla G, Guarino F, Lo Brano V, Cesarini DN, et al. *The redesign of an Italian building to reach net zero energy performances: A case study of the SHC Task 40* - ECBCS Annex 52. PART 2 ed. Montreal, QC2011. p. 331-9.

[31] Cellura M, Campanella L, Ciulla G, Guarino F, Brano VL, Cesarini DN, et al. *A net zero energy building in italy: Design studies to reach the net zero energy target*. 12th Conference of International Building Performance Simulation Association Building Simulation 2011, BS 2011. Sydney, NSW2011. p. 649-55.

[32] Garde F. and Donn M., *Solution sets and Net Zero Energy Buildings : A review of 30 Net ZEBs case studies worldwide*, Proceeding of IEA SHC Task 40 / EBC Annex 52 Towards Net Zero Energy Solar Buildings

[33] Jenssen T, König A, Eltrop L. *Bioenergy villages in Germany: Bringing a low carbon energy supply for rural areas into practice*. Renewable Energy. 2014;61:74-80.

[34] Marszal AJ. Et al., *Net Zero Energy Buildings - Calculation Methodologies versus National Building Codes*. *P*roceeding of IEA SHC Task 40 / EBC Annex 52 Towards Net Zero Energy Solar Buildings

[35] Marszal A.J. and Heiselberg P., *Zero Energy Building definition – a literature review*, Proceeding of IEA SHC Task 40 / EBC Annex 52 Towards Net Zero Energy Solar Buildings

[36] Marszal AJ, Heiselberg P, Bourrelle JS, Musall E, Voss K, Sartori I, et al. *Zero Energy Building - A review of definitions and calculation methodologies*. Energy and Buildings. 2011;43:971-9.

[37] Salom J., Marszal AJ., Widén J., Candanedo J., Lindberg KB, *Analysis of load match and grid interaction indicators in net zero energy buildings with simulated and monitored data.* Applied Energy 136 (2014) 119–131

[38] Sartori I, Napolitano A, Voss K. *Net zero energy buildings: A consistent definition framework*. Energy and Buildings. 2012;48:220-32.

[39] Torcellini P., Pless S., Deru M., *Zero Energy Buildings: A Critical Look at the Definition*, Conference Paper NREL/CP-550-39833 June 2006

[40] Voss K., Sartori I., Lollini R., *Nearly-zero, Net zero and Plus Energy Buildings – How definitions & regulations affect the solutions*, Proceeding of IEA SHC Task 40 / EBC Annex 52 Towards Net Zero Energy Solar Buildings

[41] Voss K., et al. *Load Matching and Grid Interaction of Net Zero Energy Buildings. P*roceeding of IEA SHC Task 40 / EBC Annex 52 Towards Net Zero Energy Solar Buildings

Solar component & building integration

[42] Anderson T.N., Duke M., Carson J.K., *The effect of colour on the thermal performance of building integrated solar collectors*, Solar Energy Materials&Solar Cells 94 (2010) 350–354

[43] Anderson T.N., Duke M., Morrison G.L., Carson J.K., *Performance of a building integrated photovoltaic/thermal (BIPVT) solar collector*, Solar Energy 83 (2009) 445–455

[44] Cristina S.P.L. , Frontini F., Friesen G., Friesen T.,*Experimental testing under real conditions of different solar building skins when using multifunctional BIPV systems*, Energy Procedia 48 (2014) 1412 – 1418

[45] Davidsson H., Perers B., Karlsson B., *Performance of a multifunctional PV/T hybrid solar window,* Solar Energy 84 (2010) 365–372

[46] Jin-Hee Kim *et al.*, *Experimental performance of heating system with buildingintegrated PVT (BIPVT) collector*, Energy Procedia 48 (2014) 1374 – 1384

[47] Lobaccaro G, Wall M., Product development and dissemination activities. Proceedings of Task 41

[48] Maurer C., *Solar heating and cooling with transparent façade collectors in a demonstration building*, Energy Procedia 30 (2012) 1035 – 1041

[49] Motte F., Notton G., Cristofari C., Canaletti J.L., *Design and modelling of a new patented thermal solar collector with high building integration*, Applied Energy 102 (2013) 631–639

[50] Munari Probsta MC, Roecker C., *Criteria for architectural integration of active solar systems IEA Task 41, Subtask A*, Energy Procedia 30 (2012) 1195 – 1204

[51] Munari Probsta MC et al., *Designing solar thermal system for architectural integration. Criteria and guidelines for product and system developers*. Proceedings of Task 41

[52] Munari Probsta MC et al., *Solar energy systems in architecture. Integration criteria and guidelines*, Proceedings of Task 41

[53] Munari Probst M.C., Roecker C., *Towards an improved architectural quality of building integrated solar thermal systems (BIST)*, Solar Energy 81 (2007) 1104–1116

[54] Palmero-Marrero A.I., Oliveira A.C., *Evaluation of a solar thermal system using building louvre shading devices*, Solar Energy 80 (2006) 545–554

[55] Synnefa A, Santamouris M, Apostolakis K. *On the development, optical properties and thermal performance of cool colored coatings for the urban environment*. Solar Energy 2007; 81:488–497.

[56] Tyagi V.V., Kaushik S.C., Tyagi S.K., *Advancement in solar photovoltaic/thermal (PV/T) hybrid collector technology*, Renewable and Sustainable Energy Reviews 16 (2012) 1383– 1398

[57] Visa I., Comsit M., Duta A., *Urban acceptance of facade integrated novel solar thermal collectors*, Energy Procedia 48 (2014) 1429 – 1435

[58] Wang RZ, Zhai XQ, *Development of solar thermal technologies in China*, Energy 35 (2010) 4407–4416

[59] Wang RZ. *et al.*, *Solar integrated energy system for a green building*, Energy and Buildings 39 (2007) 985–993

[60] Xiao-Yu Sun *et al.*, *Performance and building integration of all-ceramic solar collector*, Energy and Building 75 (2014)176–180

[61] Yuguo Yang *et al.*, *A building integrated solar collector: All-ceramic solar collector*, Energy and Buildings 62 (2013) 15–17

[62] Zhai XQ. *et al.*, *Experience on integration of solar thermal technologies with green buildings*, Renewable Energy 33 (2008) 1904–1910

website

- http://leso2.epfl.ch/solar/index.php?page=home

- http://task41.iea-shc.org/casestudies/

- http://www.enob.info/en/net-zero-energy-buildings/map/